

TWO-EQUATION TURBULENCE MODELING AND PARTICLE  
IMAGE VELOCIMETRY MEASUREMENTS OF HELICOPTER  
ENGINE BAY COOLING INLET FLOW

By

PETER STEPHEN GLOCKNER

A thesis presented to the Faculty of Graduate Studies,  
University of Manitoba in fulfillment of the thesis requirement  
for the degree of Masters of Science in  
MECHANICAL ENGINEERING

Department of Mechanical and Industrial Engineering  
University of Manitoba  
Winnipeg, Manitoba, Canada

© Peter Stephen Glockner, July 2002



National Library  
of Canada

Acquisitions and  
Bibliographic Services

395 Wellington Street  
Ottawa ON K1A 0N4  
Canada

Bibliothèque nationale  
du Canada

Acquisitions et  
services bibliographiques

395, rue Wellington  
Ottawa ON K1A 0N4  
Canada

*Your file* *Votre référence*

*Our file* *Notre référence*

The author has granted a non-exclusive licence allowing the National Library of Canada to reproduce, loan, distribute or sell copies of this thesis in microform, paper or electronic formats.

The author retains ownership of the copyright in this thesis. Neither the thesis nor substantial extracts from it may be printed or otherwise reproduced without the author's permission.

L'auteur a accordé une licence non exclusive permettant à la Bibliothèque nationale du Canada de reproduire, prêter, distribuer ou vendre des copies de cette thèse sous la forme de microfiche/film, de reproduction sur papier ou sur format électronique.

L'auteur conserve la propriété du droit d'auteur qui protège cette thèse. Ni la thèse ni des extraits substantiels de celle-ci ne doivent être imprimés ou autrement reproduits sans son autorisation.

0-612-76762-0

**Canada**

**THE UNIVERSITY OF MANITOBA**

**FACULTY OF GRADUATE STUDIES**

**\*\*\*\*\***

**COPYRIGHT PERMISSION PAGE**

**TWO-EQUATION TURBULENCE MODELING AND PARTICLE IMAGE  
VELOCIMETRY MEASUREMENTS OF HELICOPTER ENGINE BAY  
COOLING INLET FLOW**

**BY**

**PETER STEPHEN GLOCKNER**

**A Thesis/Practicum submitted to the Faculty of Graduate Studies of The University**

**of Manitoba in partial fulfillment of the requirements of the degree**

**of**

**Master of Science**

**PETER STEPHEN GLOCKNER © 2002**

**Permission has been granted to the Library of The University of Manitoba to lend or sell copies of this thesis/practicum, to the National Library of Canada to microfilm this thesis and to lend or sell copies of the film, and to University Microfilm Inc. to publish an abstract of this thesis/practicum.**

**The author reserves other publication rights, and neither this thesis/practicum nor extensive extracts from it may be printed or otherwise reproduced without the author's written permission.**

## ABSTRACT

In this thesis, a  $k$ - $\varepsilon$  turbulence model is presented in the context of a previously developed solver for multiphase flows. This new formulation was developed, in part, to quickly and accurately predict icing of helicopter engine bay cooling inlets. The turbulence equations are solved using a control-volume-based finite-element method. Special shape functions that prescribe the velocity profile in the near-wall region were developed. These shape functions are based on Reichardt's universal velocity profile, which may be used throughout the entire near wall region. A positivity scheme was developed that is based on physical principles and will not require ad-hoc "clipping". Proper implementation of the turbulence model is verified by simulating flow between parallel plates and flow over a backward-facing step. Particle Image Velocimetry (PIV) experiments of flow over scaled models of engine bay cooling inlets are presented. A boat was designed that enables the laser sheet to be projected through the free surface of the water tunnel. The spreading rates of the turbulent wakes downstream of two different scaled models were determined. It is anticipated that the new CFD solver will be able to accurately predict the icing of helicopter engine bay cooling inlets.

## TABLE OF CONTENTS

ABSTRACT	iii
TABLE OF CONTENTS	iv
LIST OF FIGURES	vii
LIST OF TABLES	x
ACKNOWLEDGEMENTS	xi
Chapter 1: Introduction	1
1.1 Background	1
1.2 Review of Technical Literature	3
1.3 Overview of Thesis	12
Chapter 2: The Control-Volume-Based Finite-Element Method	15
2.1 The Conservation Equations	16
2.2 The Finite Element	17
2.3 The Linear Shape Functions	20
2.4 Approximating the Diffusion Term	26
2.5 Approximating the Unsteady and Source Terms	27
2.6 Approximating the Advection Term	30
Chapter 3: Turbulence	31
3.1 Turbulent Momentum Equations	33
3.2 Types of Turbulence Models	35
3.3 Two-Equation Turbulence Models	38
3.4 Choosing an Appropriate Two-Equation Turbulence Model	41
3.5 The Standard k- $\epsilon$ Turbulence Model	44

3.6 Boundary Conditions	48
3.7 Implementation of the k- $\epsilon$ Turbulence Model	48
Chapter 4: The Near-Wall Region	51
4.1 Wall Functions	51
4.2 The Law-of-the-Wall	54
4.3 Special Shape Functions	59
4.4 Near-Wall Boundary Conditions	65
4.5 Eddy Viscosity	68
Chapter 5: Positivity Scheme	70
5.1 Source Terms	71
5.2 Beyond the Source Terms	73
5.3 Advection Positivity Scheme	76
5.4 Hybrid and Absolute Positivity Schemes	82
Chapter 6: Numerical Results	86
6.1 Channel Flow Simulation	86
6.2 Flow Over a Backward-Facing Step	105
Chapter 7: Particle Image Velocimetry Measurements	112
7.1 Particle Image Velocimetry Background	114
7.2 Seeding	115
7.3 Illumination	116
7.4 Recording	117
7.5 Processing and Analysis	118
7.5.1 Data Windowing	118

7.5.2 Correlation Plane Evaluation	121
7.6 The Water Tunnel	122
7.7 The Bluff Bodies	123
7.8 Particle Image Velocimetry Experiments	126
Chapter 8: Closure	137
8.1 Conclusions	137
8.2 Recommendations for Future Research	140
References	142

## LIST OF FIGURES

Figure 2.1: Typical CVFEM grid	18
Figure 2.2: Typical element	19
Figure 2.3: Finite element definitions	20
Figure 2.4: Normal surface vector	25
Figure 2.5: Integration area definition	28
Figure 3.1: Refined grid at a solid boundary with ice accretion	44
Figure 4.1: Comparison of dimensionless velocity profiles	59
Figure 4.2: Velocity comparisons using the log law and the new shape functions	63
Figure 4.3: Velocity gradient comparisons of the log law and the new shape function	64
Figure 5.1: Implementation of the advection positivity scheme	79
Figure 5.2: Implementation of the positivity scheme.	84
Figure 6.1: Engine bay cooling inlet configuration	87
Figure 6.1: Dimensionless velocity profiles for channel flow	91
Figure 6.2: Channel flow configuration	94
Figure 6.3: U-Velocity profiles predicted using various turbulence models	100
Figure 6.4: Turbulence kinetic energy profiles	101
Figure 6.5: Reynolds-stress profiles	102
Figure 6.6: Turbulence kinetic energy profiles	103
Figure 6.7: Reynolds-stress profiles	104
Figure 6.8: Backward-facing step flow configuration	105
Figure 6.9: Predicted properties at the channel outlet	109

Figure 6.10: Vector map of the predicted velocity field in the recirculation zone indicating a reattachment length of approximately 5.35 step heights	110
Figure 7.1: Schematics of helicopter components	113
Figure 7.2: Pictures of ice accretion on the leading edges of helicopter engine bay cooling inlets	113
Figure 7.3: Interrogation region showing the shift in the position of a particle between time $t$ and time $t+\Delta t$	115
Figure 7.4: Schematic of the ghost interrogation regions that are generated around the region under interrogation	119
Figure 7.5: Gaussian window function with $k = 1.0$ , $M = 1016$ and $N = 1008$	120
Figure 7.6: Water Tunnel 505 by Engineering Lab Designs Inc.	123
Figure 7.7: Copper support used for mounting bluff bodies resembling EBCIs in the water tunnel	125
Figure 7.8: Top of mounting system	125
Figure 7.9: Raw vector map for the flow past the bluff body resembling engine bay cooling inlet No.2	128
Figure 7.10: Validated (moving average algorithm) vector map for the flow past the bluff body resembling engine bay cooling inlet No.2	129
Figure 7.11: Statistically averaged vector map (average of 30 validated vector maps) for the flow past the bluff body resembling engine bay cooling inlet No.2	130
Figure 7.12: Streamline plot for the flow past the bluff body resembling engine bay cooling inlet No.2	131

Figure 7.13: Vorticity plot for the flow past the bluff body resembling engine bay cooling inlet No.2	131
Figure 7.14: Streamline plot for the flow past the bluff body resembling engine bay cooling inlets No.1 and No.3	135
Figure 7.15: Vorticity plot for the flow past the bluff body resembling engine bay cooling inlets No.1 and No.3	136

## LIST OF TABLES

Table 6.1: Parameters used in channel flow simulations	96
Table 6.2: Parameters used in the channel flow simulation were used to obtain inlet boundary conditions for the backward-facing step simulation	108
Table 6.3: Parameters used in the BFS simulation	111

## ACKNOWLEDGEMENTS

I would like to give special thanks to Dr. G. Naterer for his invaluable support in generating innovative ideas, helping me resolve difficult problems, providing direction when I was lost, motivating me when I felt defeated and always being available to provided assistance.

I would like to thank Mr. O. Adeyinka for his valuable ideas that were provided during hours of discussion and brainstorming.

I would like to thank Dr. N. Popplewell, Dr. R. Derksen and Dr. M. Tache of the University of Manitoba for their innovative ideas and support.

I would like to thank Mr. G. Venn and Dr. G. Richardson of GKN Westland Helicopters Ltd. for their valuable feedback.

I would like to acknowledge the partial funding of experimental equipment used in this thesis from the Canadian Foundation for Innovation, Manitoba Hydro and the Manitoba Innovation Fund.

# Chapter 1: Introduction

## 1.1 *Background*

In-flight icing of aircraft components can occur when super cooled droplets or freezing precipitation impinge on the aircraft surface with a nucleation site(s). This potential problem is a concern of the main sponsor of the current research, namely GKN Westland Helicopters Ltd. GKN is an aerospace company based in the U.K. that produces a variety of helicopters for customers all over the world, including the EH101 helicopter for the Canadian military (EH101, 1999, EH Industries, 2002). Under certain atmospheric conditions, problems may arise with ice accretion on the engine bay cooling inlets of helicopters. Sufficient ice accretion on a helicopter engine bay cooling inlet can sufficiently alter the airflow into the engine as to cause considerable problems with the engine's performance. Moreover, ice fragments may be shed and ingested into the cooling inlet, severely damaging helicopter components. GKN wishes to develop better ways to reduce/eliminate ice accretion. A passive method of reducing ice accretion involves altering the geometry of the helicopter surface to promote shedding of runback water along the surface by the local airstream before freezing occurs. A reactive method involves designing an anti-ice system that heats helicopter components to melt or prevent

accreted ice. Alternatively, pneumatic rubber boots could be installed on the leading edge of the engine bay cooling inlets, similar to those used on aircraft leading edges. Any solution may involve significant alterations to the helicopter, requiring a large capital investment, and compromises the terms of the engine or overall system performance.

As we push the limits of technology even slight improvements in performance are often difficult achievements. Trial-and-error is usually not an effective design strategy. Testing numerous prototypes of mechanical systems has become too expensive in many instances. Computer simulations are becoming an increasingly important tool when designing fluid dynamic and thermodynamic systems. Several alternative designs can be simultaneously simulated on computers, with only the most efficient designs receiving further investigation. GKN has participated with a European consortium in using a three-dimensional (3-D) multiphase Computational Fluid Dynamics (CFD) code to solve 3-D flows involving ice accretion. Performing a full aircraft icing simulation using a 3-D finite-element CFD code can be very time consuming, particularly when re-meshing is required after each time-step if the ice layer grows. It is inefficient to perform such simulations under conditions that do not lead to ice growth. An alternative CFD code is thus desired to quickly and accurately predict ice accretion. A two-dimensional (2-D) Control-Volume-Based Finite-Element Method (CVFEM) for multiphase flows with droplets has been formulated (Naterer and Schneider, 1995, Naterer et al., 2000). It is anticipated that certain helicopter simulations may be performed with this formulation to determine whether a given set of flow conditions lead to ice accretion. Conditions leading

to ice accretion may then be further examined with GKN's 3-D CFD code to solve the three-dimensional shape of the ice growth.

The previously developed 2-D CFD solver (Naterer, Schneider, 1995) has been successfully applied to several different laminar flows. However, the high velocities associated with flight render most flows associated with flight turbulent. The turbulence of the flow must therefore be included before the existing CFD code can be used to predict in-flight ice accretion on the helicopter engine bay cooling inlets. In this thesis, a two-equation  $k-\varepsilon$  turbulence model with wall functions is formulated in the context of the existing base code using a CVFEM approach to solve the turbulence equations. In addition, experimental studies are performed in relation to the engine bay cooling inlet flows.

## **1.2 *Review of Technical Literature***

Due to its practical importance, many previous studies have investigated fluid flow and heat transfer associated with aircraft icing. Schuster et al. (1992) established a rapid inlet icing analysis procedure. Naterer et al. (1999) develop an analytical model for the prediction of glaze ice accretion on electrical power lines, including the Joule heating effect. Glaze ice refers to ice growth with some unfrozen water, whereas rime ice involves droplets solidifying immediately upon impact on the surface. Methods for the solution of the multiphase conservation equations and binary-constituent solid-liquid

phase-transition problems have been developed with a CVFEM (Naterer, Schneider, 1995, 1997). Myers and Thompson (1998) derive a three-dimensional mathematical model that describes the flow of a thin film of water driven by air shear, gravity, surface tension, and ambient pressure variation over a solid substrate. Hirata and Matsui (1990) examine the ice formation phenomenon and heat transfer around isothermally cooled cylinders that are lined up in a crossflow of cold water. Lu et al. (1998) describe freezing rain simulations performed to determine the time-dependent mass of ice accreted on a short sample of a transmission line. Naterer and Glockner (2001) present pulsed laser PIV measurements of flows resembling a helicopter engine inlet flow and their contributions to a multiphase turbulence model.

Minkowycz et al. (1988) describe different ways to formulate the discretization equations from the general differential equations. Discretization of the unsteady and diffusion term is relatively standard, while various schemes are presented for advection. Special considerations for the source terms in the turbulence equations are included because of their unique requirements of positive values. Minkowycz et al. (1988) present a complete explanation of a CVFEM formulation, including discretization of the domain, the formation of control volumes and the use of linear shape functions. Schneider and Zedan (1982) present a more detailed discussion pertaining to discretization of the diffusion terms. Naterer (1999) examines the relationship between entropy processes and numerical upwinding in the context of gas space dynamics. Karimian and Schneider (1994) present a control-volume-based finite-element method with a new formulation for

the convecting integration point velocity in the implicit solution of compressible and incompressible flows.

A two-equation turbulence model was selected for use in this research, based on conversations with GKN (Naterer, 2000). Launder and Spalding (1974) present a paper that suggests that computational economy, range of applicability and physical realism are best achieved using two-equation turbulence models. Menter (1992) compares zero-equation,  $\frac{1}{2}$ -equation, one-equation and two-equation turbulence models for the well-known Samuel-Joubert flow and two flows by Driver. It was found that all but the zero-equation model deserved some credit, although all suffered from some deficiencies.

Initially a  $k$ - $\omega$  model was being pursued in this research project, where  $\omega$  represents the ratio of  $k$  to  $\varepsilon$ . Wilcox (1998) presents the most-well known  $k$ - $\omega$  turbulence model, which he later improves by incorporating the effects of cross-correlation term into the closure coefficient and auxiliary functions (Wilcox, 1998). Menter (1992) shows that the  $k$ - $\omega$  turbulence model exhibits a strong dependence on the free stream value of  $\omega$ . Liu and Zheng (1994, 1995) and Liu and Jameson (1993) present formulations in which the  $k$ - $\omega$  equations are solved on staggered control volumes. Wilcox (1994) describes how the  $k$ - $\omega$  turbulence model with viscous modifications predicts the nonlinear growth of flow instabilities from laminar flow into the turbulent flow regime. An improved multiscale  $k$ - $\omega$  model accounts for disalignment of the Reynolds-stress-tensor and the mean-strain-rate-tensor principal axes (Wilcox, 1988a). Wilcox (1993) compares eight low Reynolds number ( $k$ - $\varepsilon$  and  $k$ - $\omega$ ) models for high Reynolds number, incompressible, turbulent

boundary layers with favorable, zero, and adverse pressure gradients. Ilegbuis and Spalding (1985) claim that their new  $k-\omega$  model, that does not require any near-wall modification of constants, can accurately predict a wide range of fluid-dynamic and heat-transfer phenomena.

Speziale et al. (1992) present a  $k-\tau$  model, where  $\tau$  is the turbulent time scale, which includes an exact viscous term that is usually neglected in the  $k-\omega$  model. It yields improved predictions for turbulent boundary layers. Menter (1994) presents two new models that utilize the  $k-\omega$  model in the boundary layer and switch to the  $k-\varepsilon$  model outside the boundary layer. Menter claims that this new model leads improvements over other eddy-viscosity models when predicting adverse pressure gradient flows. Menter (1996) presents a comparison of four two-equation turbulence models and claims that the shear-stress transport model predicts better results than the standard or RNG  $k-\varepsilon$  turbulence models for flows with strong adverse pressure gradients. Also, Menter (1997) presents a method by which any two-equation eddy-viscosity turbulence model can be transformed into a one-equation model, based on Bradshaw's assumption that the turbulent shear stress is proportional to the turbulent kinetic energy.

Almost all of the above  $k-\omega$  models solve the turbulence equations through the sublayer to the wall. This requires grid refinement near the wall to capture the steep velocity gradients that exist there. As described earlier, the turbulence model in this research will be applied to a CFD solver for multiphase flows. Impinging droplets and ice growth could fill refined wall elements in a single time step, thereby requiring re-meshing. In

order to avoid this major difficulty and computational expense, the standard  $k-\varepsilon$  model with wall functions will be employed. The  $k-\varepsilon$  model is generally recognized as reliable and relatively simple compared with multi-equation models of higher order closures (Amano, 1984). The coefficients of the standard  $k-\varepsilon$  model used in Tascflow (2000) and Wilcox (1998) were adopted in this research. Cazalbou et al. (1994) examine the flow structure predicted in the vicinity of free-stream edges by two-equation eddy-viscosity models. They conclude that the turbulence kinetic energy, dissipation rate and shear stress predicted by the  $k-\varepsilon$  turbulence model propagate into the non-turbulent region at the same velocity with no need for any special relationship between the model constants.

Rodi and Scheuerer (1986) predict adverse pressure gradient flow with one-equation and  $k-\varepsilon$  turbulence models and found that a modification of the  $\varepsilon$ -equation, emphasizing the generation rate due to deceleration, improved predictions for both moderately and strongly decelerated flows. Chai and Amano (1992) report improved predictions of the second-order temperature velocity products in turbulent shear flows (over a  $k-\varepsilon$  model) using a higher-order turbulence closure model. These results arise because the Boussinesq viscosity model assumes that turbulence is isotropic, and thus it over-predicts the transverse normal components of the Reynolds stress. Yoon and Chung (1996) propose a new  $k-\varepsilon$  model with a cross-diffusion term that can be used to analyze nonequilibrium flows. Goldberg et al. (1998) achieve improved predictions with a proposed wall-distance-free low Reynolds number  $k-\varepsilon$  turbulence closure model. It incorporates an extra source term in the  $\varepsilon$  transport equation, designed to increase the level of  $\varepsilon$  in nonequilibrium flow regions. Pajayakrit and Kind (2000) suggest that a  $k-\varepsilon$

model similar to that of Dash et al. (1983) or the Baldwin-Lomax model (1978) outperformed the  $k-\omega$  model of Wilcox (1988) and the multiscale model of Wilcox (1998) for engineering calculations involving wall-jet flows.

The renormalization group (RNG)  $k-\varepsilon$  model was considered for use in this thesis. At this time, there does not seem to be a consensus as to whether the RNG model is suitable for complex flows, such as multiphase flows with droplets. However, the  $k-\varepsilon$  model's coefficients can be updated at a later time to conform to those of an RNG model. Speziale and Thangam (1992) show that the RNG  $k-\varepsilon$  model of Yakhot and Orszag (1986) substantially underpredicts the reattachment point for backward-facing step flows. They show that the recent improvements of Yakhot et al. yield excellent results for the same flow. Speziale et al. (1991) present a correction made to the RNG-based calculation of the model constant  $C_{\varepsilon 1}$  that improves the poor performance of earlier RNG models in homogeneous turbulent shear flows. Combining the claimed universality of the RNG-based  $k-\varepsilon$  model constants with the anisotropies of the nonlinear  $k-\varepsilon$  model cannot enhance predictions of both recirculating and shear flows (Papageorgakis, Assanis, 1999). Smith and Reynolds (1991) provide an independent, comprehensive, critical review of the RNG theory of turbulence developed by Yakhot and Orszag. Lam (1992) attempts to simplify the RNG theory of Yakhot and Orszag (1986) using more conventional terms and a distinctly different viewpoint.

In this thesis, wall functions will be implemented in the low Reynolds number near-wall region, where the high-Reynolds number  $k-\varepsilon$  should not be applied. Amano (1984)

performs a numerical study of separated and reattached flows created by a sudden pipe expansion. Attention is given primarily to the development of turbulence near-wall models based on the wall function. Chen and Patel (1988) investigate the performance of different near-wall treatments in a single turbulence model. They found that a two-layer model seems promising for the boundary layer and wake associated with two axisymmetric bodies. Launder (1984) suggests that wall functions may be effectively replaced by a fine-grid, near-wall treatment that extends the numerical computations through the buffer zone to the wall. Patel et al. (1985) perform a systematic evaluation of existing two-equation, low Reynolds number turbulence models. Peng and Davidson (2000) present a two-equation turbulence model in which the turbulent eddy viscosity is not constructed from scale-determining quantities, but rather it is calculated from a transport equation. This model allows integration over the near-wall region, requiring neither wall functions nor wall distance parameters in the model coefficients.

In this thesis, special shape functions are developed in the near-wall region, based on the universal velocity profile of Reichardt (Fluent, 2000b). A new specification for  $\varepsilon$  at the first interior node was derived to be consistent with Reichardt's velocity profile. A Dirichlet boundary condition for  $k$  at the first interior node was adapted (NWV, 2001). A near-wall specification for the eddy viscosity, presented by Schetz (1984), and developed by Reichardt, is used in the near-wall region to provide almost identical results to those of van Driest's mixing length model (Fluent, 2000b). Methods of calculating production of  $k$  in the near-wall region were adapted from Tascflow (2000) and Fluent (2000b) software packages.

Negative solution values of  $k$  or  $\varepsilon$  can have drastic effects on the  $k$ - $\varepsilon$  turbulence model. A positivity scheme was implemented in this regard based on physical principles. Schneider and Raw (1986) propose a skew-upwinding procedure for applications to control-volume-based finite-element computations of convective-diffusive transport problems. It precludes the possibility of developing non-physical spatial oscillations within the solution domain. Minkowycz et al. (1988) present a positive coefficient advection operator that prevents spatial oscillations in the streamwise direction. It balances mass flow rates across sub-surfaces, rather than using upwinding to determine the influence coefficients.

In this thesis, a channel flow was simulated to verify the correct formulation and implementation of the  $k$ - $\varepsilon$  turbulence model. The simulation parameters of Mansour et al. (1988), Kim et al. (1987), Kim and Moin (1989) and Teitel and Antonia (1993) were used to verify a formulation for the friction velocity presented by White (1974). All of the authors used direct numerical simulations (DNS) to obtain their results. Velocity profiles of Eckelmann (1974) were used to aid in validating the predicted velocity fields. Eddy viscosity profiles presented by Hinze (1959) provided the trend of the eddy viscosity across the channel. Moin and Kim (1982) simulate a channel flow at a Reynolds number of 13,800 using an eddy-viscosity model. Kim and Chen (1988) solved a fully developed channel flow using a finite-element computational procedure for turbulent boundary layer flows and an algebraic stress turbulence model. Johnson and King (1985) suggest that a new eddy-viscosity turbulence closure model, containing features of a Reynolds stress

model and designed specifically to treat two-dimensional turbulent boundary layers with strong adverse pressure gradients, is superior to the Cebeci-Smith model for predicting channel flows.

Also, flow over a backward-facing step was simulated to further determine whether the  $k$ - $\varepsilon$  model had been properly formulated and implemented. The key flow feature that was examined was the reattachment length. Eaton and Johnson (1980) performed a detailed experimental investigation of flow past a backward-facing step. Kim et al. (1980) investigated flow over a backward-facing step with an expansion ratio of 3 at a Reynolds number of 132,000. A reattachment length of 7.1 step heights was determined. Also, Hackman et al. (1984) and Thangam and Hur (1991) present simulations of flow over a backward-facing step using a  $k$ - $\varepsilon$  turbulence model. They state that insufficient grid refinement can lead to underprediction of the reattachment length.

Particle Image Velocimetry (PIV) is a non-intrusive, full-field flow measurement technique. It is used in this research to measure the velocity field of flows past bluff bodies resembling the helicopter engine bay cooling inlets. Buchhave (1992) discusses particle image velocimetry as a fluid mechanics tool by comparison to other flow image processing methods and standard laser anemometry. Myers et al. (1997) examine the flow field in a vessel agitated by an axial-flow impeller in turbulent operation using digital particle image velocimetry. It will be show that PIV provides a useful way to gain better physical understanding of fluid dynamics as it relates to the current helicopter application.

### 1.3 *Overview of Thesis*

Following this chapter, Chapter 2 presents the discretization of the governing equations of the  $k$ - $\varepsilon$  turbulence model in a control-volume-based finite-element method (CVFEM). Discretizing the domain using finite-elements and the formation of control volumes are described as well as the use of linear shape functions to convert between local and global coordinate systems.

Chapter 3 presents a turbulence formulation in the context of a previously developed CFD solver for multiphase flow. The need for a turbulence model and an evaluation of available models are covered. The two-equation family of turbulence models was selected for this research based on its favorable performance for a variety of complex engineering flows.

Wall functions were used to prescribe the velocity profile in the low Reynolds number near-wall region, where steep velocity gradients exist and the  $k$ - $\varepsilon$  model is not applicable. Chapter 4 presents the near-wall formulation that was used. Special shape functions were developed based on the universal velocity profile of Reichardt. A new specification for  $\varepsilon$  at the first interior node, that is consistent with Reichardt's velocity profile, is presented. A formulation for specifying the eddy-viscosity in the near-wall region is outlined. It provides results similar to those obtained using van Driest's mixing length model.

The solutions of the  $k$  and  $\varepsilon$  conservation equations must be restricted to positive values. If the values of  $k$  or  $\varepsilon$  become negative, the polarity of key processes, such as advection, diffusion and dissipation, will be reversed. Some software packages have incorporated “clipping” in which all negative values in the solution field are replaced with a positive value, usually taken to be a fraction of the largest value within the domain (Fluent 2000b). Chapter 5 discusses a positivity scheme that maintains the physics of the solution, rather than merely an exercise in mathematics. This requires implementation on a local, element-by-element basis and it controls the effects of individual physical processes, such as advection or diffusion.

Flow between parallel plates (channel flow) was simulated to verify proper implementation of the turbulence model (Chapter 6). This flow was selected because it resembles the ductwork inside of a helicopter and because it may be used to generate inlet boundary conditions for a backward-facing step simulation. The Reynolds number, based on the bulk velocity and channel half-width for the simulations, was chosen to be  $Re_m = 6,875$ . This Reynolds number corresponds to that used by Mansour et al. (1988) and Wilcox (1998) to permit a comparison of results. A formulation presented by White (1974) provides the wall shear stress from  $Re_m$ . The simulated velocity profile, obtained using the  $k$ - $\varepsilon$  turbulence model differed from that of Mansour et al. (1988). An over-prediction of velocity leads to an over-prediction of production of  $k$ , and thus incorrect predictions of other turbulence quantities. In order to assess the performance of the present  $k$ - $\varepsilon$  turbulence model, various velocity profiles were determined for  $k$ - $\omega$ , Stress- $\omega$ , Baldwin-Barth, Spalart-Allmaras, Cebeci-Smith, Baldwin Lomax and Johnson-King

turbulence models using channel flow software from DCW Inc. (Wilcox, 1998). Grid refinement improved the prediction of the turbulence quantities. Overall, the trends of  $k$  and  $\varepsilon$  appear to be correct when tested against a proper mean velocity profile. Also, Chapter 6 presents a backward-facing step simulation that was performed to further ensure that the present  $k$ - $\varepsilon$  turbulence model has been correctly formulated and properly implemented into the CFD code. The simulations predicted reasonable trends of the turbulence quantities. They produced a recirculation zone beyond the step and a reattachment length of 5.35 step heights (an approximate 25% underprediction, comparable to other  $k$ - $\varepsilon$  model under-predictions).

Chapter 7 presents particle image velocimetry (PIV) experiments that measured the flow past two bluff bodies resembling helicopter engine bay cooling inlets (EBCIs). These experiments provide the velocity field past the bluff bodies from which streamline and vorticity plots were generated. The spreading rates of the turbulent wakes were determined from the streamline plots. The spreading rates represent important problem parameters that may be used to validate numerical simulations past similarly shaped bodies.

Finally, conclusions and recommendations for future research are presented in Chapter 8.

# Chapter 2: The Control-Volume-Based Finite-Element Method

A control-volume-based finite-element method (CVFEM) has been chosen to solve the conservation equations for the fluid motion and turbulence quantities. The discretized algebraic equations represent a balance of transient storage, advection, diffusion and generation of some scalar quantity,  $\phi$ . In the finite-element approach, the domain is subdivided into four-noded quadrilateral finite elements with nodes located at the corners of the elements. A control-volume is formed around each node and it includes sub-element contributions from all surrounding elements. The governing equations are solved by a conservation approach, where the flux of  $\phi$  (i.e. momentum, kinetic energy or mass) is tracked across the borders of a control volume. An assembly procedure groups control-volume contributions from different elements.

A feature of the CVFEM that makes it particularly attractive is that it is strictly conservative. This means that there is no artificial creation or destruction of a conserved quantity due to the discretization, although errors due to the algebraic approximations of the differential governing equations can still persist. The flow of a conserved variable out

of one control volume flows into the adjacent control volume(s). The discrete equation is developed term by term from physical principals. In other words, each of the terms in the algebraic equation represents a physical process, such as diffusion, convection or production. This proves useful when analyzing the results of a simulation in that one can better understand the effects of each of the physical processes on the solution. This chapter presents how the CVFEM approach is used to solve the conservation equations for a scalar variable.

## 2.1 *The Conservation Equations*

The CVFEM is presented for a generic scalar quantity, denoted by  $\phi$ . The two-dimensional, incompressible conservation equation for  $\phi$  may be written as

$$\frac{\partial}{\partial t}(\rho\phi) + \frac{\partial}{\partial x_j}(\rho u_j \phi) = \frac{\partial}{\partial x_j} \left( \Gamma \frac{\partial \phi}{\partial x_j} \right) + s_\phi \quad (2.1)$$

The terms represent, from left to right, the transient term, the convection of  $\phi$ , the diffusion of  $\phi$  and a source term. The time derivative term renders the system of equations parabolic rather than elliptic. The variable  $\Gamma$  represents a diffusion coefficient. In the above equations the Einstein summation convention has been used (note:  $j = 1, 2$  for two-dimensional flows).

Integrating equation (2.1) over a discrete volume (or two-dimensional area,  $A$ , encompassed by its surface,  $S$ ), and using the Gauss Theorem results in the following discretized conservation equation:

$$\int_A \frac{\partial}{\partial t} (\rho\phi) dA + \int_S (\rho u_j \phi) \cdot dn_j - \int_S \left( \Gamma \frac{\partial \phi}{\partial x_j} \right) \cdot dn_j = \int_A s_\phi dA \quad (2.2)$$

where the integration is performed either over the area (volume) of the control volume or along the surface around the control volume. The term  $dn_j$  represents the outward-facing unit normal vector at the surface.

Equation (2.2) is the general form of the conservation equation that may be used for any scalar property. The CVFEM approach for solving the conservation equations is well suited to coding, as all geometric information is available at a local elemental level.

## 2.2 *The Finite Element*

In this research, the spatial domain is subdivided into 4-noded finite-elements. The nodes are situated at the corners of the elements and they represent the points where the conserved variables are solved are stored. The inter-element boundaries need not be orthogonal, thereby retaining the full geometric flexibility of a control-volume method. A sample grid, representative of those used in this thesis, is presented in Figure 2.1. The local conservations equations are generated on an element-by-element basis. The local

contributions to the conservation equations for each of the four sub-control volumes within an element are grouped together with an assembly procedure.

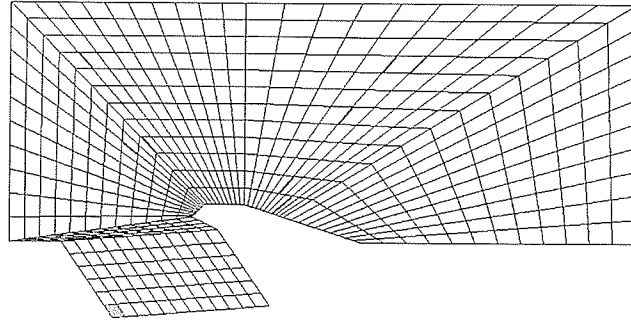


**Figure 2.1: Typical CVFEM grid**

Each element is assigned a non-orthogonal coordinate system with coordinates designated by  $s$  and  $t$  ranging from  $-1$  to  $+1$ . The local coordinate system allows each element to be treated in exactly the same manner. The nodes of an element are assigned a local numbering scheme from 1 to 4, increasing counterclockwise around an element as shown in Figure 2.2.

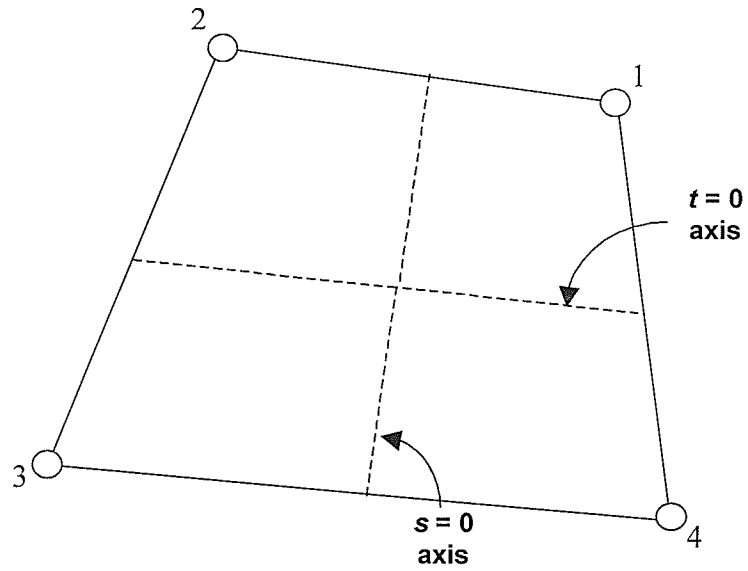


**Figure 2.2: Typical element**

The edges of the control volumes are defined by the lines  $s = 0$  and  $t = 0$  of surrounding elements as seen in Figure 2.3. The control volume is formed as an assembly of contributions from each of the four elements having a node in common. The choice of the lines  $s = 0$  and  $t = 0$  is not the only possibility. In fact, any lines of constant  $s$  and  $t$  values would suffice. The choice of the lines  $s = 0$  and  $t = 0$  ensures that the edges of adjacent control volumes coincide.

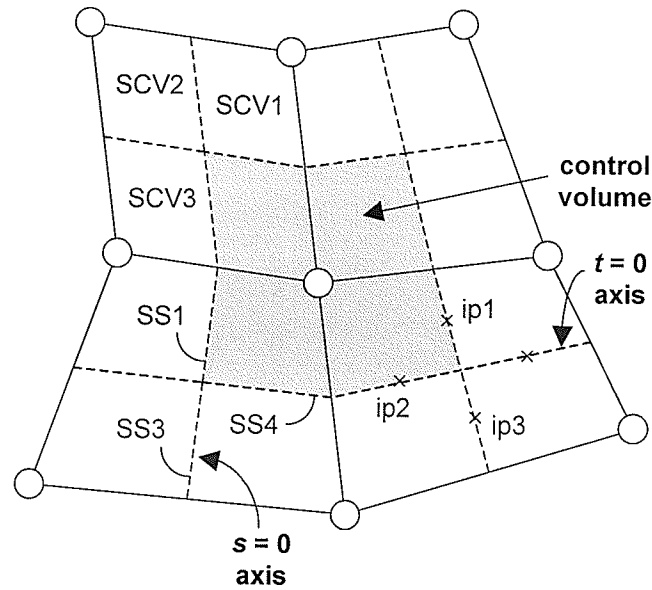


**Figure 2.3: Finite element definitions**

The lines  $s = 0$  and  $t = 0$  divide an element into four approximately equal portions, which will henceforth be referred to as sub-control-volumes (SCV) as shown in Figure 2.3. Each SCV is assigned the same number as the local node that is exclusive to that SCV. Each edge of a SCV internal to the element is referred to as a sub-surface (SS) and it is assigned the same number as the SCV located immediately clockwise of the surface, as shown in Figure 2.3. The fluxes are evaluated at the midpoints of each SS, referred to as integration-points (**ip**), whose number is the same as that of the SS on which the **ip** is centered, as shown in Figure 2.3. The advective and diffusive fluxes are evaluated at the **ips**.

### **2.3 The Linear Shape Functions**

The conservation equations are generated on an elemental level using the local coordinate system. All information about the mesh, however, is available on a global level. Thus, we

require a transformation procedure to convert between local and global coordinate systems. Bilinear shape functions (transformation functions) have been employed to perform this task. If the global  $x$  and  $y$  coordinates of local node  $i$  are designated as  $x_i$  and  $y_i$ , then the following equations may be used to calculate the global coordinates anywhere within the elements:

$$x(s, t) = \sum_{i=1}^4 N_i(s, t)x_i \quad (2.3a)$$

$$y(s, t) = \sum_{i=1}^4 N_i(s, t)y_i \quad (2.3b)$$

where the bilinear shape functions are:

$$N_1(s, t) = \frac{1}{4}(1+s)(1+t) \quad (2.4a)$$

$$N_2(s, t) = \frac{1}{4}(1-s)(1+t) \quad (2.4b)$$

$$N_3(s, t) = \frac{1}{4}(1-s)(1-t) \quad (2.4c)$$

$$N_4(s, t) = \frac{1}{4}(1+s)(1-t) \quad (2.4d)$$

Equation (2.3) may be adopted for any scalar variable  $\phi$  that is assumed to vary linearly within an element. Thus, we may write

$$\phi(s, t) = \sum_{i=1}^4 N_i(s, t) \phi_i \quad (2.5)$$

Equation (2.2) requires both the differentiation (diffusion) and integration (unsteady and source terms) of  $\phi$  at various locations within the element. We first consider the differentiation of a scalar quantity,  $\phi$ , with respect to the global coordinates,  $x$  and  $y$ . The shape functions are continuous and may thus be differentiated as

$$\left. \frac{\partial \phi}{\partial x} \right|_{s,t} = \sum_{i=1}^4 \left. \frac{\partial N_i}{\partial x} \right|_{s,t} \phi_i \quad (2.6a)$$

$$\left. \frac{\partial \phi}{\partial y} \right|_{s,t} = \sum_{i=1}^4 \left. \frac{\partial N_i}{\partial y} \right|_{s,t} \phi_i \quad (2.6b)$$

Equation (2.6) requires the  $x$  and  $y$  derivatives of the shape functions. The chain rule for partial derivatives is employed as follows:

$$\frac{\partial N_i}{\partial s} = \frac{\partial N_i}{\partial x} \frac{\partial x}{\partial s} + \frac{\partial N_i}{\partial y} \frac{\partial y}{\partial s} \quad (2.7a)$$

$$\frac{\partial N_i}{\partial t} = \frac{\partial N_i}{\partial x} \frac{\partial x}{\partial t} + \frac{\partial N_i}{\partial y} \frac{\partial y}{\partial t} \quad (2.7b)$$

The partial derivatives with respect to  $s$  of  $N_i$ ,  $x$  and  $y$  are known. A similar argument holds for the partial derivatives with respect to  $t$  of  $N_i$ ,  $x$  and  $y$ . Equation (2.7) may be rewritten in matrix form as

$$\begin{bmatrix} \frac{\partial N_i}{\partial s} \\ \frac{\partial N_i}{\partial t} \end{bmatrix} = \begin{bmatrix} \frac{\partial x}{\partial s} & \frac{\partial y}{\partial s} \\ \frac{\partial x}{\partial t} & \frac{\partial y}{\partial t} \end{bmatrix} \begin{bmatrix} \frac{\partial N_i}{\partial x} \\ \frac{\partial N_i}{\partial y} \end{bmatrix} \quad (2.8)$$

The spatial derivatives of  $N_i$  may be determined by solving the above equation to yield

$$\begin{bmatrix} \frac{\partial N_i}{\partial x} \\ \frac{\partial N_i}{\partial y} \end{bmatrix} = \frac{1}{J} \begin{bmatrix} \frac{\partial y}{\partial t} & -\frac{\partial y}{\partial s} \\ -\frac{\partial x}{\partial t} & \frac{\partial x}{\partial s} \end{bmatrix} \begin{bmatrix} \frac{\partial N_i}{\partial s} \\ \frac{\partial N_i}{\partial t} \end{bmatrix} \quad (2.9)$$

where

$$J = \frac{\partial x}{\partial s} \frac{\partial y}{\partial t} - \frac{\partial y}{\partial s} \frac{\partial x}{\partial t} \quad (2.10)$$

All of the terms in equation (2.9) and in the definition of  $J$  are known by differentiating equation (2.3) with respect to either  $s$  or  $t$ . Thus,

$$\frac{\partial x}{\partial s} = \sum_{i=1}^4 \frac{\partial N_i}{\partial s} x_i \quad \frac{\partial x}{\partial t} = \sum_{i=1}^4 \frac{\partial N_i}{\partial t} x_i \quad (2.11a, b)$$

$$\frac{\partial y}{\partial s} = \sum_{i=1}^4 \frac{\partial N_i}{\partial s} y_i \quad \frac{\partial y}{\partial t} = \sum_{i=1}^4 \frac{\partial N_i}{\partial t} y_i \quad (2.11c, d)$$

Equation (2.11) requires the local derivatives of the shape functions, which may be calculated to be

$$\frac{\partial N_1}{\partial s} = \frac{1}{4}(1+t) \qquad \frac{\partial N_1}{\partial t} = \frac{1}{4}(1+s) \qquad (2.12a)$$

$$\frac{\partial N_2}{\partial s} = -\frac{1}{4}(1+t) \qquad \frac{\partial N_2}{\partial t} = \frac{1}{4}(1-s) \qquad (2.12b)$$

$$\frac{\partial N_3}{\partial s} = -\frac{1}{4}(1-t) \qquad \frac{\partial N_3}{\partial t} = -\frac{1}{4}(1-s) \qquad (2.12c)$$

$$\frac{\partial N_4}{\partial s} = \frac{1}{4}(1-t) \qquad \frac{\partial N_4}{\partial t} = -\frac{1}{4}(1+s) \qquad (2.12d)$$

Equations (2.6) through (2.12) allow the global  $x$  and  $y$  derivatives of any scalar variable to be calculated, provided the local  $(s, t)$  coordinate and the values of  $\phi_i$  at the nodal points are known. These derivatives are required for calculating the diffusion terms and they are calculated at the integration points (shown in Figure 2.3). This procedure is coded and implemented in the CFD code.

We now possess the tools required to calculate the diffusive flux across the surfaces of a control-volume, but we have not yet defined these surfaces.

Consider the surface in Figure 2.4 that forms one of the edges of a control volume.

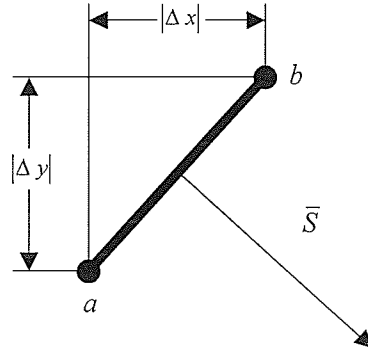


**Figure 2.4: Normal surface vector**

If one considers a counterclockwise traversal around the control volume along the line segment joining points  $a$  and  $b$ , then the vector  $\vec{S}$  is representative of the outward facing normal for the surface. If we define the distances  $\Delta x$  and  $\Delta y$  as

$$\Delta x = x_b - x_a \quad (2.13a)$$

$$\Delta y = y_b - y_a \quad (2.13b)$$

then it follows that  $\vec{S}$  may be expressed as

$$\vec{S} = \Delta y \hat{i} - \Delta x \hat{j} \quad (2.13)$$

We again use the chain rule and write

$$dx = \frac{\partial x}{\partial s} ds + \frac{\partial x}{\partial t} dt \quad (2.14a)$$

$$dy = \frac{\partial y}{\partial s} ds + \frac{\partial y}{\partial t} dt \quad (2.14b)$$

If we consider the fact that the partial derivatives of  $x$  and  $y$  with respect to  $s$  and  $t$  are constants, we may integrate equation (2.14) from  $a$  to  $b$  and write

$$\Delta x = \left. \frac{\partial x}{\partial s} \right|_{ip} \Delta s + \left. \frac{\partial x}{\partial t} \right|_{ip} \Delta t \quad (2.15a)$$

$$\Delta y = \left. \frac{\partial y}{\partial s} \right|_{ip} \Delta s + \left. \frac{\partial y}{\partial t} \right|_{ip} \Delta t \quad (2.15b)$$

where the subscript  $ip$  indicates that the derivatives are evaluated at the integration points.

In Eq. (2.15), the variables  $\Delta s$  and  $\Delta t$  are defined as

$$\Delta s = s_b - s_a \quad \text{and} \quad \Delta t = t_b - t_a \quad (2.16)$$

## 2.4 *Approximating the Diffusion Term*

We now have a formulation for approximating the differentiation of  $\phi$  at the surface of a control volume. Let us now examine exactly how this formulation may be used to approximate the diffusion terms of the conservation equations.

The diffusion terms are evaluated for all surfaces internal to the element. The discrete form of the diffusion terms in Eq. (2.2) may be written as

$$\int_{SS} \Gamma \frac{\partial \phi}{\partial x_j} \cdot dn_j \approx \Gamma \left. \frac{\partial \phi}{\partial x} \right|_{ip} \Delta y_{ip} - \Gamma \left. \frac{\partial \phi}{\partial y} \right|_{ip} \Delta x_{ip} \quad (2.17)$$

Using Eq. (2.6), we may write Eq. (2.17) in terms of nodal values, through the use of shape functions, as

$$\int_{SS} \Gamma \frac{\partial \phi}{\partial x_j} \cdot dn_j \approx \Gamma \left( \sum_{j=1}^4 \frac{\partial N_j}{\partial x} \Phi_j \right) \Delta y_{ip} - \Gamma \left( \sum_{j=1}^4 \frac{\partial N_j}{\partial y} \Phi_j \right) \Delta x_{ip} \quad (2.18)$$

where all derivatives are evaluated at the integration points. Using an uppercase  $\Phi$  indicates that a nodal value is considered, as opposed to a lowercase  $\phi$ , which indicates an integration point value. We now have a way of evaluating the diffusion terms of the conservation equations. Let us now consider the unsteady and source terms, for which we require a formulation for integrating  $\phi$  over a sub-control volume.

## 2.5 *Approximating the Unsteady and Source Terms*

The unsteady terms and the source terms in Eq. (2.2) require a procedure that allows  $\phi$  to be integrated over an area bounded by a given  $s$  and  $t$  range. Define a vector,  $\vec{r}$ , as

$$\vec{r} = x\hat{i} + y\hat{j} \quad (2.19)$$

at any point within an element, as shown in Figure 2.5.

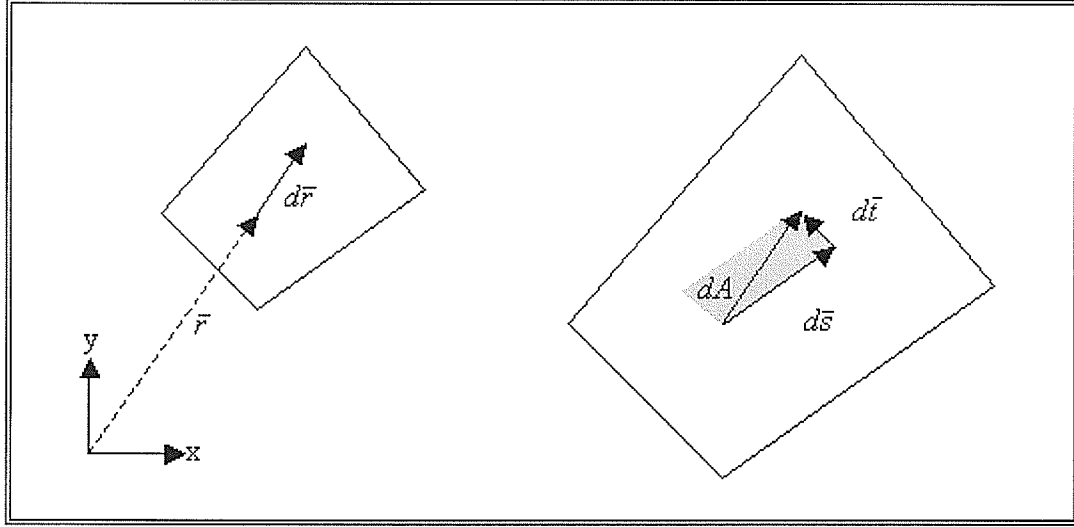


**Figure 2.5: Integration area definition**

A change in the vector  $\vec{r}$  may be written as

$$d\vec{r} = \frac{\partial \vec{r}}{\partial s} ds + \frac{\partial \vec{r}}{\partial t} dt \quad (2.20)$$

If we rewrite  $d\vec{r}$  in terms of changes in the local coordinates traversed by  $d\vec{r}$ , i.e.

$$d\vec{r} = d\vec{s} + d\vec{t} \quad (2.21)$$

Then the area defined by the vectors  $d\vec{s}$  and  $d\vec{t}$  is given by their vector product as

$$dA = |d\vec{s} \times d\vec{t}| = \left| \frac{\partial \vec{r}}{\partial s} \times \frac{\partial \vec{r}}{\partial t} \right| ds dt = \left| \left( \frac{\partial x}{\partial s} \hat{i} + \frac{\partial y}{\partial s} \hat{j} \right) \times \left( \frac{\partial x}{\partial t} \hat{i} + \frac{\partial y}{\partial t} \hat{j} \right) \right| ds dt \quad (2.22)$$

Examination of Eq. (2.10) reveals the relation

$$dA = |J| ds dt \quad (2.23)$$

The transient storage term in Eq. (2.2) is solved using a lumped approach, wherein we assume that the value of the scalar is constant across the area of integration. The value of the scalar is calculated at the center of each sub-control volume. For example, the value of the scalar would be determined at  $(s, t) = (1/2, 1/2)$  for SCV1. The lumped approach leads to the following discrete form of the transient term,

$$\int_{SCV} \frac{\partial}{\partial t} (\rho\phi) dA \approx \rho J \left( \frac{\Phi^{n+1} - \Phi^n}{\Delta t} \right) \quad (2.24)$$

where the superscripts  $n+1$  and  $n$  indicate that  $\Phi$  is evaluated at the new and previous time steps, respectively.

A lumped approach is also used for source terms, in which case we may write

$$\int_{SCV} S_\phi dA \approx S_\phi J \quad (2.24)$$

where  $S_\phi$  is evaluated at the center of the sub-control volume under consideration.

## 2.6 Approximating the Advection Term

The advection term in Eq. (2.2) is evaluated for all surfaces internal to the element. For SCV1, the advection term is evaluated at SS4 and SS1 (see Figure 2.3). The discrete form of the advection term may be written as

$$\int_{SS} (\rho u_j \phi) \cdot dn_j \approx \rho u_{ip} \phi_{ip} \Delta y - \rho v_{ip} \phi_{ip} \Delta x \quad (2.25)$$

where the subscript  $ip$  indicates that the variable is evaluated at an integration point. The terms  $\Delta x$  and  $\Delta y$  indicate the change in the values of  $x$  and  $y$  for a counter-clockwise traversal of the sub-surface. It may be observed that the integration point velocities must be written in terms of nodal quantities since the final algebraic equations involve nodal  $\Phi$  only. The relative influences of neighboring nodes are contained within influence coefficients. In this thesis, the influence coefficients are determined by a Physical Influence Scheme (PINS) (Naterer, 2002). In this method, the dependence of the central node on neighboring nodes is obtained by a local approximation of the governing transport equations at the central node.

All of the conservation equations in the CFD model are solved with the CVFEM approach presented in this chapter.

## Chapter 3: Turbulence

Flows with either very small characteristic lengths or low velocities are typically laminar. Laminar flows are characterized by the diffusion of momentum by molecular viscosity alone. They typically reach a steady-state solution, given fixed conditions at all inlets and outlets and sufficient elapsed time. In these cases, the instantaneous flow properties eventually match the steady-state values. The levels of inertia in the flow are not large enough to overcome the diffusive action of molecular viscosity. Unfortunately, there are few flows of engineering and industrial interest that may be classified as entirely laminar.

If the velocity of a laminar flow is gradually increased, there generally exists a point at which the inertia of the fluid will begin to overcome the diffusive effects of viscosity (Wilcox, 1998). At this point, known as the transition point, the flow will destabilize and become intermittently turbulent. If the velocity is further increased, the flow usually becomes fully turbulent. Thus, it may be said that turbulent flows develop from instability of laminar flows. Almost all flows of practical engineering interest may be classified as turbulent flows. Steep velocity gradients and pressure gradients are typical of turbulent flows. The unsteady nature of turbulent flows requires the time history of the flow in order to determine current instantaneous properties of the flow. We usually do not

require a complete transient solution of a flow, so we are thus satisfied with calculating the time-averaged solution. While the instantaneous solution of a turbulent flow is highly dependent on initial conditions, the statistically averaged properties are typically not.

It would prove useful to briefly explain some of the characteristics of turbulence. When discussing the length scales of turbulence, we often refer to eddies, which are local swirling regions in the fluid that are responsible for enhanced mixing and effective turbulent stresses. The diameters of these eddies are representative of the length scales of the turbulence. Turbulence may be considered to be a continuum phenomenon because the smallest scale of the turbulence (the size of the smallest eddies) is several orders of magnitude larger than the size of the fluid's molecules. Thus, we need not track individual molecules. In actuality, there is a continuous range of length scales, encompassing the larger energy-bearing eddies through to the smallest eddies. In order to exactly solve the 3-D time-dependent motion of the fluid, one would need to solve the equations of motion for several different length scales. This type of solution is not practical, given the limits of current computer technology. Fortunately, we can make use of the fact that turbulence is a cascading process, whereby energy is cascaded down from the largest eddies to the smallest eddies. The smallest eddies dissipate energy into heat through the action of molecular diffusion. It is the larger energy-bearing eddies, however, that determine the rate at which the energy is cascaded down to the smaller eddies, thus determining the dissipation rate of the turbulence. Thus, solving the equations of motion for the larger scale eddies is usually sufficient.

High velocities generally render all flows pertaining to aircraft flight to be turbulent. Any models that are used in predicting ice accretion during flight should account for the turbulent nature of the flow. The turbulent fluctuations in the flow lead to enhanced diffusion (momentum and energy) and effective turbulent stresses, which are often several orders of magnitude larger than viscous stresses found in laminar flows. Many methods of accounting for the effects of turbulence in a flow involve an eddy (or turbulent) viscosity. A turbulence model must be incorporated into any CFD code before it may be used in solving the flight-related fluid flows.

### 3.1 *Turbulent Momentum Equations*

Let us examine the turbulent momentum equations to better understand how turbulence changes the laminar momentum equations. The laminar momentum equation for incompressible flow is

$$\rho \frac{\partial U_i}{\partial t} + \rho u_j \frac{\partial U_i}{\partial x_j} = -\frac{\partial P}{\partial x_i} + \mu \frac{\partial}{\partial x_i} \left( \frac{\partial U_i}{\partial x_j} + \frac{\partial U_j}{\partial x_i} \right) \quad (3.1)$$

The variables  $u$ ,  $p$  and  $\mu$  represent velocity, pressure and dynamic viscosity, respectively. We derive the turbulent momentum equations by rewriting the velocity and pressure terms as the sum of mean and fluctuating components, viz. (Wilcox, 1998)

$$u_i(x_j, t) = U_i(x_j) + u_i'(x_j, t) \quad (3.2a)$$

$$p(x_j, t) = P(x_j) + p'(x_j, t) \quad (3.2b)$$

where uppercase variables represent time-averaged (mean) components and primed variables represent fluctuating (turbulent) components of the instantaneous variable. The time-average,  $F_T(x)$ , of the instantaneous flow variable,  $f(x, t)$ , may be defined as

$$F_T(x) = \lim_{T \rightarrow \infty} \frac{1}{T} \int_t^{t+T} f(x, t) dt \quad (3.3)$$

In the above equation, the characteristic time interval,  $T$ , cannot realistically reach infinity and so it is chosen to be very long relative to the maximum period of the fluctuations. After inserting the instantaneous variables of Eq. (3.2) into Eq. (3.1) and time averaging the results, we arrive at the turbulent momentum equations, viz.

$$\rho \frac{\partial U_i}{\partial t} + \rho U_i \frac{\partial U_i}{\partial x_i} + \rho \frac{\partial}{\partial x_j} (\overline{u_j' u_i'}) = -\frac{\partial P}{\partial x_i} + \mu \frac{\partial}{\partial x_i} \left( \frac{\partial U_i}{\partial x_j} + \frac{\partial U_j}{\partial x_i} \right) \quad (3.4)$$

Details of the time averaging process may be found in Wilcox (1998). A comparison of the laminar and turbulent forms of the momentum equations reveals that all fluctuating components are removed by the time-averaging procedure except for the correlation involving  $\overline{u_j' u_i'}$ , which is the time-averaged rate of momentum transfer due to turbulent fluctuations. This correlation is responsible for the enhanced diffusion of scalar

properties, such as velocity and energy. Equation (3.4) may be written in its most familiar form as

$$\rho \frac{\partial U_i}{\partial t} + \rho U_i \frac{\partial U_i}{\partial x_i} = -\frac{\partial P}{\partial x_i} + \frac{\partial}{\partial x_i} \left( \mu \frac{\partial U_i}{\partial x_j} + \mu \frac{\partial U_j}{\partial x_i} - \rho \overline{u_j' u_i'} \right) \quad (3.5)$$

This equation is usually referred to as the Reynolds-averaged Navier-Stokes equation. The term  $-\overline{u_j' u_i'}$  is the specific Reynolds stress tensor and it is denoted as  $\tau_{ij}$ . The purpose of a turbulence model is to provide an approximation for the apparent stress (the Reynolds stress tensor) in terms of known flow properties, such that a sufficient number of equations exist to permit a closed solution.

### 3.2 *Types of Turbulence Models*

Several different approaches have been developed to account for the effects of the apparent turbulent stresses. Some of these turbulence models include algebraic (or zero-equation) models, one-equation models, two-equation models and stress-transport models. Each class of turbulence model has advantages and disadvantages that will be discussed below. The nature of the flow and the desired parameters dictate which type of model is most appropriate for a particular application.

**Algebraic models** are the simplest turbulence models. They utilize the Boussinesq eddy-viscosity approximation to allow computations of the Reynolds stress tensor as a product of an eddy viscosity and the mean strain rate tensor. An algebraic relation between the

eddy viscosity and length scales of the mean flow usually specifies the mixing length. An algebraic model is termed incomplete because the mixing length and eddy viscosity need to be specified in advance. Although simpler than the two-equation models or stress-transport models, algebraic models have proven useful in many engineering fields. Some researchers are still making advances in the effective use of algebraic models, most notably the Cebeci-Smith and Baldwin-Lomax models, which divide the flow into inner and outer regions. Both the Cebeci-Smith and Baldwin-Lomax models accurately reproduce the skin friction and velocity profiles for incompressible turbulent boundary layers in flows with weak pressure gradients (Wilcox, 1998).

**One-Equation models** are slightly more complex than algebraic models in that they involve one more equation to be solved, namely an equation that allows the specification of the eddy viscosity. For example, Prandtl (Wilcox, 1998) expressed the eddy viscosity as

$$v_T = k^{1/2}l = C_D \frac{k^2}{\varepsilon} \quad (3.6)$$

In order to determine the eddy viscosity, only one equation needs to be solved, namely the equation for the turbulence kinetic energy, viz.

$$\frac{\partial k}{\partial t} + U_j \frac{\partial k}{\partial x_j} = P_k - C_D \frac{k^{3/2}}{l} + \frac{\partial}{\partial x_j} \left[ \left( \nu + \frac{v_T}{\sigma_k} \right) \frac{\partial k}{\partial x_j} \right] \quad (3.7)$$

where  $l$  is a mixing length,  $\sigma_k$  is a dimensionless constant and  $P_k$  is the production of turbulence kinetic energy, which may be expressed as

$$P_k = \tau_{ij} \frac{\partial U_i}{\partial x_j} \quad (3.8)$$

Prandtl's one-equation model is not complete, as the mixing length still requires specification in advance. Other more elaborate one-equation models have more recently been devised that contain far more closure coefficients and empirical damping coefficients. Some of these models are complete, meaning that no other information, such as a mixing length, needs be specified in advance. However, this does not have any implications pertaining to the accuracy of their results.

Stress-transport models are often referred to as second-order closure or second moment closure models. These models naturally incorporate the effects of streamline curvature, sudden changes in strain rate and secondary motions. The disadvantage of such improvements is a larger number of equations, the introduction of more closure coefficients and a dramatic increase in model complexity and computer resources. This has led stress-transport models to be applied to relatively few applications.

The two-equation family of turbulence models has been selected for use in this research and it is detailed further in the following sections.

### 3.3 Two-Equation Turbulence Models

A two-equation turbulence model has been chosen for solving the problem of ice accretion on helicopter engine bay cooling inlets for many reasons. Most of the research conducted on turbulence models in the past couple of decades has focused on two-equation turbulence models. These models have enjoyed success in simulating a variety of complex flows for which algebraic models would be inappropriate. The geometry of the engine bay cooling inlet (see sample representation in Fig. 2.1) is likely too complex for an algebraic model, as there would be difficulties in prescribing an appropriate length scale. Two-equation models provide a prescription for the computation of  $k$ , as well as providing the length scale. This makes two-equation models complete, in that they do not require any prior knowledge of the turbulence structure. A two-equation model appears to be capable of providing reasonable estimates of the turbulence length scales in an eddy viscosity approach. Thus, it appears to provide a good basis from which droplet effects may be included in future work.

Most two-equation turbulence models make use of the Boussinesq eddy-viscosity approximation. This approximation assumes that the Reynolds stress tensor is proportional to the mean velocity gradients. The constant of proportionality is the eddy viscosity. Thus, the Boussinesq eddy-viscosity approximation may be written as

$$\tau_{ij} = \overline{-u_i' u_j'} = \nu_T \left( \frac{\partial U_i}{\partial x_j} + \frac{\partial U_j}{\partial x_i} \right) \quad (3.9)$$

In order to model a turbulent flow field, we need to calculate the spatial distribution of  $\nu_T$ , rather than attempting to predict the unknown correlation  $\overline{u_j' u_i'}$ .

Almost every two-equation turbulence model makes use of the conservation equation for the turbulence kinetic energy,  $k$ , which may be written as (Wilcox, 1998)

$$\frac{\partial k}{\partial t} + U_j \frac{\partial k}{\partial x_j} = \tau_{ij} \frac{\partial k}{\partial x_j} - \varepsilon + \frac{\partial}{\partial x_j} \left[ \left( \nu + \frac{\nu_T}{\sigma_k} \right) \frac{\partial k}{\partial x_j} \right] \quad (3.10)$$

There are several variations of two-equation turbulence models and it is the second transport equation that dictates into which family the turbulence model is classified. There is also a wide range of closure coefficients and damping functions within each family.

**The  $k$ - $\tau$  family of turbulence models** uses a turbulence dissipation time,  $\tau$ , as the second variable. Dimensional analysis provides us with a means of calculating the eddy viscosity, turbulence length scale and dissipation rate viz.

$$\nu_T \propto k\tau, \quad l \propto k^{1/2}\tau, \quad \varepsilon \propto \frac{k}{\tau} \quad (3.11)$$

**The  $k$ - $\omega$  family of turbulence models** uses the ratio of  $k$  to  $\varepsilon$ , denoted  $\omega$ , as the second variable. This leads to a formulation for the eddy viscosity, dissipation rate and length scale, viz.

$$v_T \propto \frac{k}{\omega}, \quad l \propto \frac{k^{1/2}}{\omega}, \quad \varepsilon \propto \omega k \quad (3.12)$$

Some authors choose to express the second transport equation in terms of  $\omega^2$ .

**The  $k$ - $\varepsilon$  family of turbulence models** uses the specific dissipation rate,  $\varepsilon$ , as the second scalar variable. This leads to a formulation for the eddy-viscosity and turbulence length scale viz.

$$v_T \propto \frac{k^2}{\varepsilon}, \quad l \propto \frac{k^{3/2}}{\varepsilon} \quad (3.13)$$

Each of the families contains several models, each with a unique method of writing the second transport equation, most notably in the specification of the closure coefficients and damping functions. Each of the families has merits and drawbacks. It is up to the researcher to decide which of the models is most appropriate to their work. For reasons discussed earlier, the  $k$ - $\varepsilon$  family of turbulence models has been selected for this research, and it will be further discussed in the following section.

### 3.4 *Choosing an Appropriate Two-Equation Turbulence Model*

A literature review was conducted in order to determine which two-equation turbulence models were available, together with their advantages and disadvantages. Among the many two-equation turbulence models, it is the standard  $k-\varepsilon$  and  $k-\omega$  models that are receiving the most widespread attention. The most notable work on the  $k-\omega$  model has been performed by Wilcox et al. have performed the most notable work on the  $k-\omega$  model (Wilcox, 1988a, 1993, 1994, 1998) whereas several researchers are pursuing the  $k-\varepsilon$  model. Some authors (Wilcox, Menter, Speziale and Peng; documented by Wilcox, 1998) have combined the two models, benefiting from the advantages, while eliminating some of the shortcomings of each individual model.

The choice of which two-equation turbulence model should be used in this research depended largely on the method in which the models handle the near-wall region of wall-bounded flows. Large velocity gradients exist in this region, thereby requiring an excessive number of nodal points to accurately capture the details of the flow. Numerical difficulties arise when using the standard  $k-\varepsilon$  model in the near-wall region. This is largely due to the fact that the standard  $k-\varepsilon$  model is strictly a high-Reynolds number model. As a result, it is not applicable in the near-wall region. Additionally, the equations of the standard  $k-\varepsilon$  model are stiff in the near-wall region, leading to computational difficulties (Wilcox, 1998).

Many difficulties associated with the standard  $k$ - $\varepsilon$  model are not present in the standard  $k$ - $\omega$  model. The standard  $k$ - $\omega$  model is a low-Reynolds number model and it may be applied in both the near-wall and fully turbulent regions. The solution of  $\omega$  in the near-wall regions is highly dependent on the value of  $\omega$  in the free-stream (Wilcox, 1998, Menter, 1991, Kok, 1999). This may lead to inaccurate solutions of the near-wall region if inappropriate boundary conditions are applied to the free-stream flow. A hybrid model that combines the  $k$ - $\varepsilon$  and  $k$ - $\omega$  models alleviates this free-stream dependence by including a cross diffusion term viz.

$$+ 2 \frac{(\nu + \sigma \nu_T)}{k} \frac{\partial k}{\partial x_j} \frac{\partial \omega}{\partial x_j} \quad (3.14)$$

on the right-hand side of the transport equation for the turbulence kinetic energy, i.e. Eq. (3.10). This cross diffusion term arises when the formal change of variables  $\varepsilon = c_\mu k \omega$  is made in the standard transport equation for  $k$ . While the inclusion of the cross diffusion term improves the predictive capabilities of the  $k$ - $\omega$  model, the differential equations are far more difficult to solve. Wilcox has derived a  $k$ - $\omega$  model that incorporates the influence of the cross-diffusion term into the model's closure coefficients with the addition of some auxiliary relations (Wilcox, 1998).

The most notable difficulty associated with both the  $k$ - $\omega$  and hybrid turbulence models arises specifically when they are implemented into a multiphase CFD code. As mentioned earlier, in order to resolve the steep velocity gradients in the near-wall region,

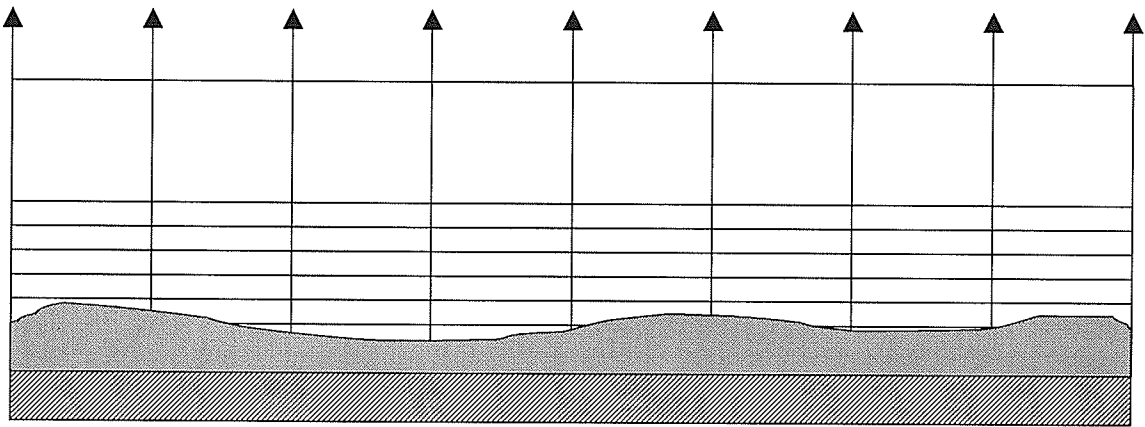
the grid immediately adjacent to solid walls needs to be refined. Besides significantly increasing computation times due to the increased number of nodal points, considerable difficulties arise when applying boundary conditions at the onset and growth of ice on the surface.

Figure 3.1 depicts a typical surface on which ice accretion has occurred. The boundary condition for  $\omega$  is applied to the first interior node of the solution domain. An accurate resolution of the near-wall region demands that this point is very close to the surface. For smooth surfaces, the boundary condition on  $\omega$  is (Wilcox, 1988a)

$$\omega \rightarrow \frac{6\nu_w}{\beta y^2}; \quad y \rightarrow 0 \quad (3.15)$$

where  $\beta$  is an empirical constant having a value of 3/40. Equation (3.15) is no longer applicable at the first interior nodal point after it has become completely submerged in ice, or the unfrozen water layer containing incoming droplets. The degree of grid refinement required when integrating the conservation equations directly to the wall could lead to submersion of the first interior node in a single time step. Thus, re-meshing is required after the solution of each time step (an/or inter-equation iteration) after the onset of ice accretion. This is excessively inconvenient for most applications, thereby appearing to render the use of the  $k-\omega$  and hybrid models inappropriate for these types of multiphase simulations.

In light of the above arguments, it was decided that the  $k-\varepsilon$  turbulence model with wall functions would be used. Wall functions prescribe a universal velocity profile within the near-wall region. The solution domain for the high-Reynolds number  $k-\varepsilon$  model extends only to the tops of the wall elements, which may be sufficiently removed from the wall as to reduce the difficulties associated with ice and/or water/droplets filling these wall elements.



**Figure 3.1: Refined grid at a solid boundary with ice accretion**

### 3.5 *The Standard $k-\varepsilon$ Turbulence Model*

The  $k-\varepsilon$  model is generally recognized as reliable and it is relatively simple compared with multi-equation models of higher order closures (Amano, 1984). The  $k-\varepsilon$  turbulence model of Jones and Launder (1972) is the most well known two-equation turbulence model developed to date. In fact, it is so well known that it is commonly referred to as the standard  $k-\varepsilon$  model. The revised closure coefficients of Launder and Sharma (1974) are used by most researchers today (Wilcox, 1998).

The standard  $k$ - $\varepsilon$  model, henceforth referred to as the  $k$ - $\varepsilon$  model, makes use of the Reynolds stress tensor of Eq. (3.9) and the transport equation for  $k$ , Eq. (3.10). The second transport equation attempts to model the specific dissipation rate of the turbulence kinetic energy,  $\varepsilon$ . The quantity  $\varepsilon$  is defined as

$$\varepsilon = \nu \frac{\overline{\partial u_i'} \partial u_i'}}{\partial x_k \partial x_k} \quad (3.16)$$

The exact transport equation for  $\varepsilon$  may be written as (Wilcox, 1998)

$$\begin{aligned} \frac{\partial \varepsilon}{\partial t} + U_j \frac{\partial \varepsilon}{\partial x_j} = & -2\nu \left( \frac{\overline{\partial u_i'} \partial u_j'}}{\partial x_k \partial x_k} + \frac{\overline{\partial u_k'} \partial u_j'}}{\partial x_i \partial x_j} \right) \frac{\partial U_i}{\partial x_j} - 2\nu \left( \frac{\overline{\partial u_i'}}{\partial x_j} \right) \frac{\partial^2 U_i}{\partial x_k \partial x_j} \\ & - 2\nu \frac{\overline{\partial u_i'} \partial u_i' \partial u_k'}}{\partial x_k \partial x_l \partial x_l} - 2\nu^2 \frac{\overline{\partial^2 u_i'}}{\partial x_k \partial x_l} \frac{\partial^2 u_i'}{\partial x_k \partial x_l} \\ & + \frac{\partial}{\partial x_j} \left( \nu \frac{\partial \varepsilon}{\partial x_j} - \overline{\nu u_j' \partial u_i' \partial u_i'} - \frac{2\nu}{\rho} \frac{\overline{\partial p' \partial u_j'}}{\partial x_l \partial x_l} \right) \end{aligned} \quad (3.17)$$

The first line of the right hand side of Eq. (3.17) represents the production of  $\varepsilon$ . The second line represents the dissipation of  $\varepsilon$ . The last line represents the sum of the molecular diffusion of  $\varepsilon$  and the turbulent transport of  $\varepsilon$ . The exact transport equation for  $\varepsilon$  is extremely complex and would require impractical amounts of computer resources to solve. The  $\varepsilon$  transport equation of the standard  $k$ - $\varepsilon$  turbulence model approximates Eq. (3.17) using empirical relations for production, dissipation and diffusion of  $\varepsilon$ . The  $k$ - $\varepsilon$  model used in this research is shown as follows,

**Eddy Viscosity:**

$$\nu_T = c_\mu \frac{k^2}{\varepsilon} \quad (3.18)$$

**Turbulence Kinetic Energy:**

$$\frac{\partial(\rho k)}{\partial t} + U_j \frac{\partial(\rho k)}{\partial x_j} = \frac{\partial}{\partial x_j} \left[ \left( \mu + \frac{\mu_T}{\sigma_k} \right) \frac{\partial k}{\partial x_j} \right] + P_k - \rho \varepsilon \quad (3.19)$$

**Dissipation Rate:**

$$\frac{\partial(\rho \varepsilon)}{\partial t} + U_j \frac{\partial(\rho \varepsilon)}{\partial x_j} = \frac{\partial}{\partial x_j} \left[ \left( \mu + \frac{\mu_T}{\sigma_\varepsilon} \right) \frac{\partial \varepsilon}{\partial x_j} \right] + C_{\varepsilon 1} \frac{\varepsilon}{k} P_k - C_{\varepsilon 2} \rho \frac{\varepsilon^2}{k} \quad (3.20)$$

where the production of turbulence kinetic energy,  $P_k$ , for 2-D incompressible flow is

$$P_k = \tau_{ij} \frac{\partial U_i}{\partial x_j} = \mu_T \left( \frac{\partial U_i}{\partial x_j} + \frac{\partial U_j}{\partial x_i} \right) \frac{\partial U_i}{\partial x_j} = \mu_T \left[ 2 \left( \frac{\partial U}{\partial x} \right)^2 + 2 \left( \frac{\partial V}{\partial y} \right)^2 + \left( \frac{\partial V}{\partial x} + \frac{\partial U}{\partial y} \right)^2 \right] \quad (3.21)$$

In the above equations,  $U$  and  $V$  refer to the mean velocity components in the  $x$  and  $y$  directions, respectively. The closure coefficients of equations (3.20) and (3.21) are (Tascflow, 2000):

$$\sigma_k = 1.0, \quad \sigma_\varepsilon = 1.3, \quad C_{\varepsilon 1} = 1.44, \quad C_{\varepsilon 2} = 1.92, \quad c_\mu = 0.09 \quad (3.22)$$

In the  $k$  equation, the terms represent (from left to right) the convective (substantive) derivative of  $k$ , flux of  $k$  by diffusion, production of  $k$  and dissipation of  $k$ , respectively. The production term,  $P_k$ , represents the rate at which kinetic energy is transferred to the turbulence from the mean flow.

The term  $\mu \partial k / \partial x_j$  is molecular diffusion and it represents the diffusion of turbulent energy by the fluid's molecular transport process. The other term,  $(\mu_T / \sigma_k) \partial k / \partial x_j$ , includes two parts: (i) the rate at which turbulent kinetic energy is transported through the fluid by the turbulent fluctuations, and (ii) pressure diffusion (interactions between pressure and velocity fluctuations).

The total viscosity is the sum of the laminar and the eddy viscosity viz.

$$\nu = \nu_0 + \nu_T \quad (3.23)$$

$$\mu = \mu_0 + \mu_T \quad (3.24)$$

Incorporating Eq. (3.24) into Eq. (3.5) yields Eq. (3.1), where  $\mu$  now represents the total viscosity.

The  $k$ - $\varepsilon$  turbulence model provides us with a means of calculating the spatial distribution of  $\nu_T$  and thus the distribution of the total viscosity of Eq. (3.24). The total viscosity is passed from the turbulence model to the momentum equations by means of the Prandtl number, Pr. The value of Pr is calculated at each integration point as

$$\text{Pr} = \frac{c_p \rho (v + v_T)}{k} \quad (3.25)$$

where  $c_p$  is the specific heat and  $k$  is the thermal conductivity of the fluid.

### **3.6 *Boundary Conditions***

The boundary conditions at inlets and outlets are handled the same for  $k$  and  $\varepsilon$  as they are for the non-turbulent variables. Dirichlet or Neumann boundary conditions are applied on  $k$  and  $\varepsilon$  at the inlets and outlets. Special boundary conditions are applied along solid boundaries using wall functions. The wall boundary conditions will be detailed in Chapter 4.

### **3.7 *Implementation of the $k$ - $\varepsilon$ Turbulence Model***

The  $k$ - $\varepsilon$  turbulence model has been added to an existing CFD code that originally contained no turbulence model, henceforth referred to as the base code. The first step in incorporating the turbulence model was to become familiar with the structure of the base code and determine the best implementation strategy. Other students are adding subroutines to the base code as well, so it is desirable to change the base code as little as possible.

The mainline of the base code calls a subroutine that reads the mesh file, as well as the laminar initial and boundary condition files. The format of these initial and boundary

condition files would ideally have been modified to include entries for  $k$  and  $\varepsilon$ . This may have prevented the base code from operating properly for laminar simulations and may not have been compatible with the works of other students. It was thus decided to read the initial and boundary condition information for  $k$  and  $\varepsilon$  from separate turbulent initial and boundary condition files.

The initial values of  $k$  and  $\varepsilon$  should have no impact on their final (steady state) values. They have, however, been used to calculate the initial value of the total viscosity, through Eqs. (3.18) and (3.23). This initial value of the total viscosity dictates whether a realistic velocity field will be obtained from the first solution of the momentum equations. It has been found that if the initial total viscosity is too low, the first solution of the momentum equations will not converge yielding a velocity field that is very inaccurate, with nodal outliers that are several orders of magnitude too large. This creates drastic problems with the solution of  $k$  and  $\varepsilon$  for the first time step because of the unrealistic distribution of production. It has been found that choosing  $k$  and  $\varepsilon$  such that a Reynolds number based on the eddy viscosity, rather than the kinematic viscosity, corresponds to laminar flow, which results in a well behaved initial solution of the velocity field. Then, a reasonable first solution of the eddy viscosity distribution may be calculated.

A segregated solution is used for the  $k$  and  $\varepsilon$  equations rather than a simultaneous solution. The  $k$  transport equation is solved first, using the most recently updated values of  $k$ ,  $\varepsilon$ , and  $\nu_T$ . The  $\varepsilon$  transport equation is then solved, using the most recent values of both  $\varepsilon$  and  $\nu_T$ , along with the value of  $k$  from the previous iteration (not the most recent

solution). The solutions of  $k$  and  $\varepsilon$  are iterated until either of the following two conditions is met: (i) the solution of the eddy viscosity converges to within a user-defined tolerance, or (ii) the solution has iterated a user-defined maximum number of times. The newest solution of the eddy viscosity is used to update  $Pr$ , through Eq. (3.25), which is then used by the next iteration of the momentum equations.

The  $k$ - $\varepsilon$  turbulence model discussed in this chapter has been implemented into the CFD base code. All of the flows studied in this thesis are wall-bounded flows. It still remains, however, to describe the wall functions that are required in the near-wall region. Chapter 4 discusses the treatment of the near-wall region, including why the wall functions are required and how they are implemented.

# Chapter 4: The Near-Wall Region

The near-wall region of a wall-bounded flow requires special attention when applying boundary conditions for  $k$  and  $\varepsilon$ . Dramatic grid refinement would be required close to solid walls to accurately capture the steep velocity gradients that exist there. For reasons discussed earlier (i.e. near-wall ice growth and reducing computational costs) we choose to impose a velocity profile in the near-wall region based on universal velocity profiles, rather than solving the velocity profile using conservation equations. This chapter presents the universal velocity profiles along with their range of applicability and describes their implementation into the CFD code.

## 4.1 *Wall Functions*

A difficulty arises when modeling turbulent flows using the  $k$ - $\varepsilon$  model in the viscosity-affected near-wall region. This is the region adjacent to solid boundaries that contains the viscous sublayer and buffer region. The near-wall region is bounded by the fully turbulent core flow and a solid boundary. The velocity increases from zero at the wall to an order of magnitude of the mean flow through the near-wall region. The thickness of the near-wall region is typically several orders of magnitude smaller than the

characteristic length of the flow. The near-wall region thus contains very large velocity gradients.

One technique that has been used to resolve the velocity profile in the near-wall region is to refine the grid near solid boundaries. This permits the conservation equations for the turbulence and flow fields to be directly integrated through the sublayer to the physical wall. However, the stiffness of the  $k-\varepsilon$  model near solid boundaries often leads to numerical difficulties. Additionally, the  $k-\varepsilon$  model is a high-Reynolds number model, and thus it will not produce accurate results if implemented in the low-Reynolds number near-wall region.

One alternative method for solving the near-wall region involves blending a low-Reynolds number model in the near-wall region with the  $k-\varepsilon$  model outside the sublayer where the flow is fully turbulent. One such low-Reynolds number model is van Driest's mixing length model (Fluent, 2000b).

Other researchers have attempted to adapt the  $k-\varepsilon$  model to the near-wall region by imposing damping coefficients near solid boundaries with varying degrees of success (Patel et al., 1984). However, many of these models fail to reproduce even the simple test case of the flat-plate boundary layer.

One of the most successful alternatives to the popular  $k-\varepsilon$  model is the  $k-\omega$  model, such as that of Wilcox (1988a, 1998). The  $k-\omega$  model can be applied to both the fully turbulent

and near-wall regions, but suffers from computational difficulties in the free-stream. This arises from difficulties in modeling the cross-diffusion term (which includes gradients of both  $k$  and  $\omega$ ) that is necessary to achieve convergent results in this region (Wilcox, 1998).

All of the previous methods require mesh refinement in the near-wall region in order to accurately resolve the steep velocity gradients near solid walls. This leads to increased solution times due to the dramatic increase in the number of nodal points in the near-wall region. This increase in solution time may be justifiable in some circumstances, but there is another difficulty that arises with grid refinement near solid boundaries. In this research, the turbulence model will be incorporated into a multiphase CFD code that will be used to simulate flows where droplets are impinging and ice is accreting on a solid surface. Even small ice growth may fill several of these small elements in a single time step as discussed in Chapter 3. This creates problems when applying boundary conditions, and re-meshing would be required to conform to the new solid surface.

A cost effective method of specifying the velocity in the near-wall region is required, so that it does not suffer from the aforementioned difficulties associated with grid refinement. One such method of dealing with the near-wall region is to apply wall functions that utilize the law-of-the-wall.

## 4.2 *The Law-of-the-Wall*

In light of the drawbacks associated with other near-wall methodologies, it has been decided that wall functions will be implemented in the near-wall region. Wall functions make use of universal velocity profiles commonly referred to as laws-of-the-wall. The law-of-the-wall approach imposes a universal velocity profile in the near-wall region, rather than calculating it with the momentum equations. The velocity profile is usually specified as a function of the dimensionless distance from the wall (or ice surface).

The law-of-the-wall approach makes several assumptions about the flow (Fluent, 2000b), i.e.

- the flow is assumed to be predominantly parallel to the wall and in local equilibrium,
- there is no injection or suction of fluid at the wall, and
- the effects of body forces are small.

These assumptions lead to the requirement that the flow remains attached to the wall. These conditions are met over most of the near-wall regions examined in this thesis. Exceptions include areas of strong adverse pressure gradients, separation, reattachment and stagnation. Despite these theoretical limitations, wall functions have been shown to provide reasonable predications over most of the physical domain.

If the above conditions are met, then it is not unreasonable to assume that the shear stress,  $\tau$ , is nearly constant through the viscous sublayer and equal to the value of the wall shear stress,  $\tau_w$ . The velocity in the near-wall region is related to  $\tau_w$  and it is specified by a dimensionless universal velocity profile. This logarithmic profile is a function of the dimensionless distance from the wall,  $y^+$ . The most general statement of the law-of-the-wall may be written as

$$U^+ = \frac{U}{u_\tau} = f(y^+) \quad (4.1)$$

where  $U$  represents the velocity tangent to the wall. The dimensionless distance from the wall,  $y^+$ , depends on the friction velocity,  $u_\tau$ , the distance from the wall,  $\Delta$ , and the kinematic viscosity,  $\nu$ , as follows,

$$y^+ = \frac{u_\tau \Delta}{\nu} \quad (4.2)$$

The friction velocity may be calculated from the wall shear stress as follows:

$$u_\tau = \sqrt{\frac{\tau_w}{\rho}} \quad (4.3)$$

The aforementioned formulation may become singular at stagnation points and points of separation if the velocity predicted by the momentum equations at the first interior node,

$U_M$  approaches zero. This problem is overcome by making the following additional assumptions:

- Couette flow,
- Constant stress layer.

This allows us to make the following relation between the wall shear stress and the turbulence kinetic energy:

$$\frac{\tau_w}{\rho} = c_\mu^{1/2} k \quad (4.4)$$

The value of  $k$  will be non-zero at points of stagnation and separation, even if  $U_M$  approaches zero. Eq. (4.4) leads to the following alternative expression for the friction velocity,

$$u_\tau = \left( c_\mu^{1/2} k \right)^{1/2} \quad (4.5)$$

It remains to specify the function  $f(y^+)$  in Eq. (4.1). Many functional forms have been presented for the universal velocity profile. The following solutions have been developed for  $f(y^+)$  in the viscous sublayer and the fully turbulent region, typically bounded by  $y^+ < 5$  and  $y^+ > 30$ , respectively, as follows,

**Viscous sublayer:**

$$U^+ = y^+; \quad y^+ < 5 \quad (4.4)$$

**Fully turbulent region:**

$$U^+ = \frac{1}{\kappa} \ln(9y^+); \quad y^+ > 30 \quad (4.5)$$

where  $\kappa$  is the von Karman constant having a value of 0.41. The region between the viscous sublayer and the fully turbulent region is commonly referred to as the buffer layer. Unfortunately, it is not possible to analytically derive an expression for the velocity profile in the buffer layer. An algebraic expression, based on experimental data, has been established for the buffer layer and may be expressed as

**Buffer layer:**

$$U^+ = 6.4264 \times 10^{-4} y^{+3} - 5.211310^{-2} y^{+2} + 1.4729 y^+ - 1.1422; \quad 5 \leq y^+ \leq 30 \quad (4.6)$$

Equations (4.4) through (4.6) specify the velocity (tangent to the wall) between the wall and the outer edge of the log layer. Unfortunately, it is necessary to determine in which of the three regions the velocity should be calculated before these equations may be applied in our CFD code. Thus, we desire a continuous universal velocity profile that is applicable at any point within the near-wall region. One such function is the so-called Reichardt's law, viz.

$$U^+ = \frac{1}{\kappa} \ln(1 + \kappa y^+) + 7.8 \left[ 1 - \exp\left(\frac{-y^+}{11}\right) - \frac{y^+}{11} \exp(-0.33y^+) \right] \quad (4.7)$$

Figure 4.2 shows a comparison between the velocity profiles obtained with Eqs. (4.4) through (4.6) to that obtained from Reichardt's law. The graph shows that Reichardt's law matches the law-of-the-wall very closely in the viscous sublayer and fully turbulent region.

Reichardt's law provides us with the velocity profile in the near-wall region. This velocity profile may be differentiated, as required when calculating production of  $k$  in the near-wall elements. Special shape functions were developed that provide us with the velocity gradient in the near-wall region.

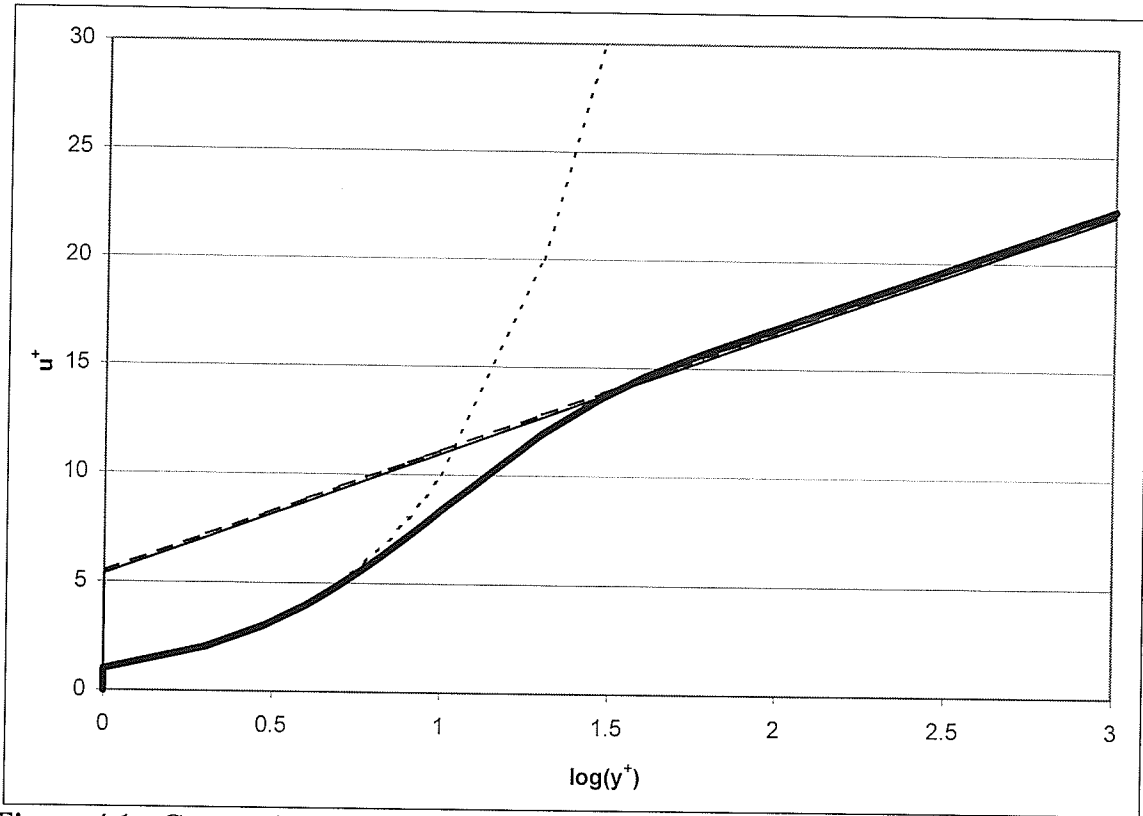


Figure 4.1: Comparison of dimensionless velocity profiles: - - -  $U^+ = y^+$ , —  $U^+ = (1/\kappa)\ln(9y^+)$ , — —  $U^+ = 2.44\ln(y^+) + 5.5$ , — — Reichardt's Law.

### 4.3 Special Shape Functions

Special logarithmic shape functions, based on Reichardt's law, are applied to all wall elements. The shape functions are derived using a linear basis function parallel to the wall and a logarithmic basis function perpendicular to the wall (Fluent, 2000b). These special shape functions depend on the characteristic turbulence Reynolds number,

$$\Delta^+ = \frac{(c_\mu^{1/2} k)^{1/2} \Delta}{\nu} \quad (4.8)$$

The turbulence Reynolds number is a function of  $k$  at the “top” of the wall elements. This functional dependence of the shape functions on  $k$  allows the velocity profile within the special wall elements to adapt to the level of turbulence kinetic energy from previous iterations.

When applying the special wall functions, it is important to ensure that the wall elements are fully contained within the fully turbulent region. This condition may be expressed mathematically as

$$\Delta^+ > 30 \tag{4.10}$$

If the value of  $\Delta^+$  is less than 30 over a significant length of the wall, then the flow should be re-simulated with a sparser grid along the solid boundary. Applying the shape function at a node for which  $\Delta^+$  is significantly lower than 30 effectively forces the turbulence into the non-turbulent near-wall region and it will yield erroneous results.

As a starting point while developing the shape functions, the dimensionless distance  $y^+$  of Eq. (4.7) is replaced with the characteristic Reynolds number in Eq. (4.8). The new shape functions are formed by combining a linear basis function (in a direction tangent to the wall) and a new logarithmic basis function, based on Reichardt’s law (in a direction normal to the wall).

The logarithmic basis function may be written as

$$A(n) = A_1(n) / A_2 \quad (4.11)$$

where

$$A_1(n) = \frac{1}{\kappa} \ln \left[ 1 + \kappa \Delta^+ \frac{(1+n)}{2} \right] + 7.8 \left\{ 1 - \exp \left[ \frac{-\Delta^+(1+n)}{22} \right] - \frac{\Delta^+(1+n)}{22} \exp[-0.165\Delta^+(1+n)] \right\} \quad (4.12)$$

$$A_2 = A_1(n=1) \quad (4.13)$$

Unlike the linear shape functions used in the CVFEM method, the shape functions used to specify the velocities differ depending on which two local nodes define the solid wall of the element. Thus, four shape functions are developed as follows.

**Local nodes 1 and 2 define the solid surface:**

$$\begin{aligned} N_1 &= \frac{1}{2}(1-t)(1-A) \\ N_2 &= \frac{1}{2}(1+t)(1-A) \\ N_3 &= \frac{1}{2}(1+t)A \\ N_4 &= \frac{1}{2}(1-t)A \end{aligned} \quad (4.14a)$$

**Local nodes 2 and 3 define the solid surface:**

$$\begin{aligned} N_1 &= \frac{1}{2}(1-t)A \\ N_2 &= \frac{1}{2}(1-t)(1-A) \\ N_3 &= \frac{1}{2}(1+t)(1-A) \\ N_4 &= \frac{1}{2}(1+t)A \end{aligned} \quad (4.14b)$$

*Local nodes 3 and 4 define the solid surface:*

$$\begin{aligned} N_1 &= \frac{1}{2}(1+t)A \\ N_2 &= \frac{1}{2}(1-t)A \\ N_3 &= \frac{1}{2}(1-t)(1-A) \\ N_4 &= \frac{1}{2}(1+t)(1-A) \end{aligned} \quad (4.14c)$$

*Local nodes 4 and 1 define the solid surface:*

$$\begin{aligned} N_1 &= \frac{1}{2}(1+t)(1-A) \\ N_2 &= \frac{1}{2}(1+t)A \\ N_3 &= \frac{1}{2}(1-t)A \\ N_4 &= \frac{1}{2}(1-t)(1-A) \end{aligned} \quad (4.14d)$$

In the above shape functions,  $A$  represents  $A(n)$  as defined in Eq. (4.11).

An advantage of these newly developed shape functions is that the velocity profile is valid and continuous from the wall to the fully turbulent region. A comparison between the velocity profiles in the near-wall region for the law-of-the-wall and the new shape functions was performed. Two velocity profiles are shown in Figure 4.3 for different values of the turbulence kinetic energy at the top of the wall element. The velocity is 1 m/s at the first interior node, which would usually be provided from the solution of the momentum equations. The normal height of the element is 0.005 m.

It is evident that the two velocity profiles are very similar, especially in the fully turbulent region. This indicates that Reichardt's law accurately specifies the velocity in the near-wall region.

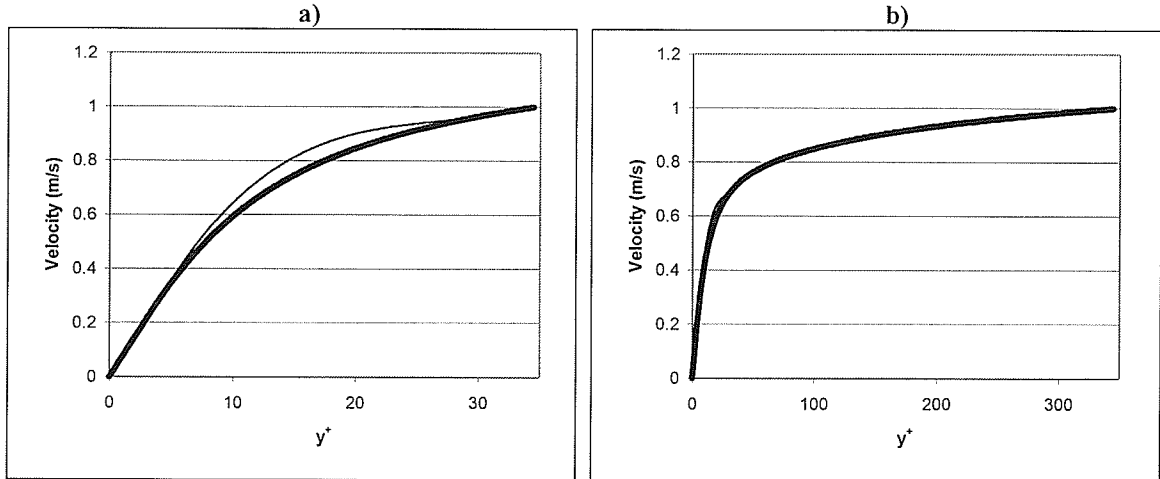


**Figure 4.2: Velocity comparisons using the log law and the new shape functions for a)  $k=0.01 \text{ m}^2/\text{s}^2$  and b)  $k=1.0 \text{ m}^2/\text{s}^2$ . The thick line represents the shape function velocity whereas the thin line represents the log law velocity.**

As has already been mentioned, the wall functions provide the velocity profile within the near-wall region. However, we are not only interested in obtaining the velocity profile. Knowing the velocity profile provides a means of calculating the velocity gradient within the near-wall region. This gradient is required when determining the amount of production of turbulence kinetic energy in the wall elements and thus it contributes to the stiffness matrix for  $k$  and  $\varepsilon$  at the first interior nodes.

Production in the wall elements may be expressed as follows:

$$P_k = \tau_w \frac{\partial U}{\partial n} \quad (4.15)$$

where  $n$  represents the outward-facing normal direction from the wall.

The velocity gradient in Eq. (4.15) is calculated using the newly developed shape functions. Two sample velocity gradient profiles are shown in Figure 4.4 for different values of the turbulence kinetic energy at the top of the wall element. In these examples , the velocity is 1 m/s at the first interior node, which is again located 0.005 m from the wall.

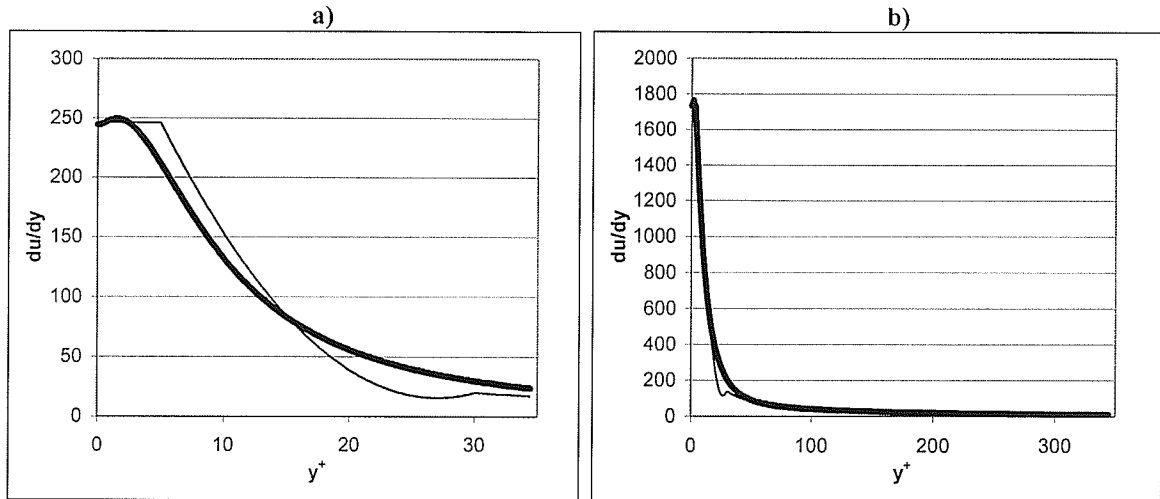


**Figure 4.3: Velocity gradient comparisons using the log law and the new shape functions for a)  $k=0.01 \text{ m}^2/\text{s}^2$  and b)  $k=1.0 \text{ m}^2/\text{s}^2$ . The thick line represents the shape function velocity gradient while the thin line represents the log law velocity gradient.**

The plots show that the magnitudes of the velocity gradient are in agreement. One of the benefits of using a universal velocity profile that spans the entire near-wall region is that there are no discontinuities in the shape function velocity profile, which accounts for the continuity of the corresponding velocity gradient profile. Additionally, the new shape functions do not require special consideration pertaining to which region (i.e. sublayer, buffer/overlap region or fully turbulent region) the flow belongs to.

The production of  $k$  in the near-wall elements contributes to the  $k$  conservation equation of the first interior nodes. A zero-flux boundary condition is placed on the  $k$ -equation at solid walls. This allows the level of turbulence kinetic energy at the “top” of a wall element, which determines the amount of skewing in the above shape functions, to vary in response to turbulence processes in the flow. This zero-flux boundary condition is consistent with the equilibrium turbulence conditions in the near-wall regions where  $k$  is a constant.

#### 4.4 *Near-Wall Boundary Conditions*

The value of  $\varepsilon$  at the first interior node is typically specified as

$$\varepsilon = \frac{P_k}{\rho} = \frac{u_\tau^3}{\kappa n} = \frac{(c_\mu^{1/2} k)^{3/2}}{\kappa n} \quad (4.16)$$

This expression was derived assuming that production of  $k$  balances dissipation of  $k$  in the near-wall region, and assuming a velocity profile resembling

$$U_{nw}^+ = \frac{1}{\kappa} \ln(y^+) + C; \quad y^+ > 10 \quad (4.17)$$

where the subscript  $nw$  indicates a velocity calculated based on the near-wall formulation. The value of  $C$  is approximately 5.5. The implication that production balances dissipation

in the near-wall region may be justified by considering the  $k$  equation in the near-wall region, viz.

$$\text{unsteady term} + \text{advection term} = P_k - \rho\varepsilon + \text{diffusion term} \quad (4.18)$$

Turbulent fluctuations are small in the near-wall region, thereby reducing Eq. (4.18) to

$$\varepsilon = \frac{P_k}{\rho} \quad (4.19)$$

We calculated the velocity differential of Eq. (4.15) by applying the chain rule to Eq. (4.17), yielding

$$\frac{\partial U_{nw}}{\partial n} = \frac{\partial U_{mw}}{\partial y^+} \frac{\partial y^+}{\partial n} = \frac{u_\tau}{\kappa} \left( \frac{1}{y^+} \right) \left( \frac{u_\tau}{v} \right) = \frac{u_\tau}{\kappa} \left( \frac{v}{nu_\tau} \right) \left( \frac{u_\tau}{v} \right) = \frac{u_\tau}{\kappa n} \quad (4.20)$$

Substituting Eqs. (4.3), (4.15) and (4.20) into Eq. (4.19) yields the desired formulation for  $\varepsilon$  at the first interior node, Eq. (4.16). Our near-wall velocities are calculated based on Reichardt's law and they are prescribed using Eq. (4.7). A different expression needs to be developed to specify  $\varepsilon$  at the tops of the near-wall elements. The new expression is derived in exactly the same manner as that described above. The resulting expression for  $\varepsilon$  that is consistent with Reichardt's law is

$$\varepsilon = \frac{u_\tau^4}{\nu} \left[ \frac{1}{1 + \kappa(y^+)} + \frac{7.8}{11} \exp\left(\frac{-y^+}{11}\right) + \frac{2.574}{11} y^+ \exp(-0.33y^+) - \frac{7.8}{11} \exp(-0.33y^+) \right] \quad (4.22)$$

The value of  $\varepsilon$  from Eq. (4.22) is applied as a boundary condition on  $\varepsilon$  at the first interior node. A zero-flux boundary condition is placed on  $\varepsilon$  at the corresponding wall nodes.

Originally a zero-flux boundary condition was placed on  $k$  at the wall. Production of  $k$  in the near-wall elements was calculated using Eq. (4.15) with the value of the velocity gradient determined by differentiating the special wall functions. The value of  $\Delta^+$  in Eq. (4.8) depended on the value of  $k$  at the top of the wall elements, allowing production in the near-wall elements to “float” in response to turbulent processes (Fluent, 2000b). The boundary condition on  $k$  was changed in an attempt to determine the cause of certain errors to be discussed in Chapter 6. This revealed an inconsistency with the prediction of velocity in the near-wall region that can lead to erroneous predictions of production of  $k$  in the near-wall region. A Dirichlet boundary condition is now applied to  $k$  at the first interior node as follows:

$$k = \frac{\tau_w}{\rho c_\mu^{1/2}} = \frac{u_\tau^2}{c_\mu^{1/2}} \quad (4.23)$$

A zero-flux boundary condition is applied at the corresponding wall node. The boundary conditions of Eq. (4.22) and Eq. (4.23) are consistent with the equilibrium turbulence conditions within the near-wall region in which the turbulence length scale, defined as

$$l_T = \frac{k^{3/2}}{\varepsilon} \quad (4.24)$$

varies linearly with distance from the wall (Fluent, 2000b).

#### 4.5 Eddy Viscosity

The  $k$ - $\varepsilon$  equations belong to the high-Reynolds number turbulence model, so they are not solved in the near-wall region. The domain over which the  $k$  and  $\varepsilon$  equations are solved thus extends only to the tops of the wall elements. This requires an alternate means of calculating the eddy viscosity in the near-wall region. In this research, we choose to use the following expression, developed by Reichardt (Schetz, 1984), to prescribe the eddy viscosity in the near-wall region:

$$\nu_T = \kappa \nu \left[ \left( \frac{y u_\tau}{\nu} \right) - 9.7 \tanh \left( \frac{y u_\tau}{9.7 \nu} \right) \right] \quad (4.25)$$

where  $\kappa$  is Von Karman's constant, having a value of 0.41. This eddy viscosity profile has been compared to that obtained using van Driest's mixing length model, viz.

$$\mu_T = \rho l_m^2 \left[ \left( \frac{\partial u_i}{\partial x_j} + \frac{\partial u_j}{\partial x_i} \right) \frac{\partial u_i}{\partial x_j} \right]^{1/2} \quad (4.26)$$

The mixing length,  $l_m$ , is specified using van Driest's equation, viz.

$$l_m = \kappa \delta [1 - \exp(-y^+ / A)] \quad (4.27)$$

where  $\delta$  is the normal distance from the wall. Also,  $A$  is an empirical constant assuming a value of approximately 26 for hydraulically smooth walls in equilibrium near-wall layers. These two formulations produced nearly indistinguishable results. Eq. (4.25) is preferred because it does not require calculation of the velocity gradient, and is it thus simpler to code. This completes our formulation for the specification on the eddy viscosity in the near-wall region.

A  $k$ - $\varepsilon$  turbulence model with wall functions has now been presented. As mentioned in Chapter 3, small initial values of the total viscosity can yield very inaccurate velocity predictions, which may lead to negative values of  $k$  or  $\varepsilon$ . This can have disastrous effects on the turbulence model. A novel positivity scheme is presented in Chapter 5 that is based on physical principles, and it should never require "clipping" to maintain positive values of  $k$  and  $\varepsilon$ .

# Chapter 5: Positivity Scheme

The solution of the momentum equations and energy equation encompasses both positive and negative values. For example, one would not be surprised to find values of  $u = -2.76$  m/s or  $T = -5.3$  °C. The solutions of the  $k$  and  $\varepsilon$  equations, however, are restricted to positive values. If the values of  $k$  or  $\varepsilon$  become negative, the polarity of key processes, such as advection, diffusion and dissipation, will be reversed. This implies, for example, that the dissipation term in the  $k$ -equation would be transferring energy from the mean flow to the turbulence, which could have disastrous effects on the solution. Some software packages have incorporated “clipping”, in which all negative values in the solution field are replaced with a positive value, usually taken to be a fraction of the largest value within the domain (Fluent 7, 2000a). Clipping is an entirely unphysical procedure that simply prevents the CFD code from terminating due to negative values of  $k$  and/or  $\varepsilon$  destabilizing the solution field.

This chapter discusses a positivity new scheme that maintains the physics of the solution, rather than simply an exercise in mathematics. This requires implementation on a local, element-by-element basis. It would be more efficient to apply the positivity scheme to the global stiffness matrices. This procedure, however, would not enable one to control the

effects of individual physical processes, such as advection or diffusion. Although implementing the positivity scheme on an element-by-element basis requires regenerating the global stiffness matrices, it is felt that retaining the physics of each process is critical to obtaining a physically realistic solution.

## 5.1 Source Terms

We first consider the values of  $k$  or  $\varepsilon$  becoming negative due to contributions from the source terms. There is only one correct sign for each of the source terms based on the physical meanings of the terms. For example, the dissipation term in the  $k$ -equation must be negative because the term represents the transfer of energy from the turbulence to the mean flow. Raithby proposes that holding the ratio of  $k/\varepsilon$  constant throughout an iteration (at their previous iteration values) speeds up the convergence process and eliminates the possibility of negative solution values resulting from source terms (Minkowycz et al., 1988). Thus, in the  $k$ -equation, we replace the conventional dissipation term, viz.

$$-\rho\varepsilon \tag{5.1}$$

with the positivity source term, viz.

$$-\rho\left(\frac{\varepsilon^m}{k^m}\right)k^{n+1} \tag{5.2}$$

where the superscripts  $n+1$  and  $m$  indicate a value of  $k$  or  $\varepsilon$  at the new time step or from the previous iteration, respectively. Similarly for the  $\varepsilon$ -equation we replace

$$+C_{\varepsilon 1} \frac{\varepsilon^{n+1}}{k^{n+1}} P_k \quad \text{and} \quad -C_{\varepsilon 2} \rho \frac{(\varepsilon^{n+1})^2}{k^{n+1}} \quad (5.3)$$

with

$$+C_{\varepsilon 1} \left( \frac{\varepsilon^m}{k^m} \right) P_k \quad \text{and} \quad -C_{\varepsilon 2} \rho \left( \frac{\varepsilon^m}{k^m} \right) \varepsilon^{n+1} \quad (5.4)$$

Let us consider the equations for  $k$  and  $\varepsilon$  with only the transient and source terms to better understand how these modifications prevent negative solutions due to source terms. We may write

$$\rho \frac{\partial k^{n+1}}{\partial t} = P_k - \rho \left( \frac{\varepsilon}{k} \right)^m k^{n+1} \quad (5.5)$$

$$\rho \frac{\partial \varepsilon^{n+1}}{\partial t} = +C_{\varepsilon 1} \left( \frac{\varepsilon}{k} \right)^m P_k - C_{\varepsilon 2} \rho \left( \frac{\varepsilon}{k} \right)^m \varepsilon^{n+1} \quad (5.6)$$

When these equations are discretized and rearranged, expressions may be written for  $k$  and  $\varepsilon$  at the new time step,  $n+1$ , viz.

$$k^{n+1} = \frac{\frac{\rho}{\Delta t} k^n + P_k}{\frac{\rho}{\Delta t} + \rho \left(\frac{\varepsilon}{k}\right)^m} \quad (5.7)$$

$$\varepsilon^{n+1} = \frac{\frac{\rho}{\Delta t} \varepsilon^n + C_{\varepsilon 1} \left(\frac{\varepsilon}{k}\right)^m P_k}{\frac{\rho}{\Delta t} + C_{\varepsilon 2} \rho \left(\frac{\varepsilon}{k}\right)^m} \quad (5.8)$$

where the superscript  $n$  indicates a value from the previous time step. The production term,  $P_k$ , is necessarily positive, since it is a sum of squares. All other terms on the right hand sides of Eqs. (5.7) and (5.8) are necessarily positive, assuming that the values of  $k$  and  $\varepsilon$  were positive from the previous time step. Thus, neglecting the diffusion and advection terms, the values of  $k$  and  $\varepsilon$  are guaranteed to remain positive.

We now have a contribution to the positivity scheme that prevents source terms from causing negative values of  $k$  or  $\varepsilon$ . Let us now take a closer look at the full conservation equation to find out what other terms can cause negative values of  $k$  or  $\varepsilon$  and develop a positivity scheme for those terms.

## 5.2 *Beyond the Source Terms*

Let us examine a conservation equation to clarify which non-source terms can cause the solution fields to contain negative values. We consider only one-dimensional flow for

simplicity, although all of the arguments presented can be readily adapted to two dimensions. The turbulence kinetic energy equation at node  $P$ , for one-dimensional incompressible flow, may be written as

$$\begin{aligned} \frac{\rho}{\Delta t} \phi_P^{n+1} - \frac{\rho}{\Delta t} \phi_P^n + A_P \phi_P^{n+1} - A_L \phi_L^{n+1} - A_R \phi_R^{n+1} = \\ - D_P \phi_P^{n+1} + D_L \phi_L^{n+1} + D_R \phi_R^{n+1} + P_k - \rho \frac{\varepsilon_P^m}{\phi_P^m} \phi_P^{n+1} \end{aligned} \quad (5.9)$$

where  $\phi$  is used to represent turbulence kinetic energy. It reminds us that this discussion could apply to any scalar variable. The variables  $A$  and  $D$  represent the magnitude of a global advection coefficient and the magnitude of a global diffusion coefficient, while the subscripts  $P$ ,  $L$  and  $R$  refer to the central node, left neighboring node and right neighboring node, respectively.

Grouping similar terms in Eq. (5.9) yields

$$\left( \frac{\rho}{\Delta t} + A_P + D_P + \rho \frac{\varepsilon_P^m}{\phi_P^m} \right) \phi_P^{n+1} = P_k + \frac{\rho}{\Delta t} \phi_P^n + (A_L + D_L) \phi_L^{n+1} + (A_R + D_R) \phi_R^{n+1} \quad (5.10)$$

Solving for  $\phi_P^{n+1}$  yields

$$\phi_P^{n+1} = \frac{P_k + \frac{\rho}{\Delta t} \phi_P^n + (A_L + D_L) \phi_L^{n+1} + (A_R + D_R) \phi_R^{n+1}}{\frac{\rho}{\Delta t} + A_P + D_P + \rho \frac{\varepsilon_P^m}{\phi_P^m}} \quad (5.11)$$

As mentioned in section 5.1, the production term is necessarily positive, since it is a sum of squares. Also, in a well-behaved solution, the advection and diffusion coefficients will also be positive (Minkowycz et al, 1988). In that case, both the numerator and denominator of (5.11) are positive (assuming  $\phi_L^{n+1}$  and  $\phi_R^{n+1}$  are positive for the new solution), yielding a positive value of  $\phi_p^{n+1}$ . Let us now take a closer look at the advection and diffusion coefficients to determine the circumstances in which they could result in either the numerator or denominator having a negative sum.

The influence coefficients, used to calculate the advection fluxes, are determined from a physical influence scheme (PINS) (Naterer, 2002). These coefficients are calculated in terms of integration point and nodal values, which after an inversion process, are written in terms of nodal values only. Negative contributions to advection fluxes can arise from neighboring nodal point values,  $\phi_N$ , if the corresponding mass flow rates are out of the control volume. After assembling all contributions from surrounding nodes, some of these terms may remain negative, leading to positive off-diagonal entries in the global stiffness matrix. This implies that an increase in  $\phi_N$  could result in a non-physical decrease in  $\phi_p$ . This is known as the “negative coefficient problem” and it can lead to spatial oscillations in the streamwise direction, resulting in negative values of  $\phi$  (Minkowycz et al., 1988). This has disastrous implications in a turbulence model. An unconverged solution of the velocity field is the most likely reason why the  $k$ - $\varepsilon$  model would predict negative values of  $k$  or  $\varepsilon$ . This is due to poor specification of  $k$  and  $\varepsilon$  at the tops of the wall elements and an unreasonable prediction of production as described in Chapter 3. The goal of the positivity scheme is to eliminate the possibility of positive off-

diagonal coefficients in the global  $\phi$  stiffness matrix by incorporating them into the diagonal coefficient.

### 5.3 *Advection Positivity Scheme*

Let us first consider the case where it is an advection term that is causing a positive off-diagonal coefficient in the global stiffness matrix, for which we will devise an “advection positivity scheme”. Positive off-diagonal coefficients in the global stiffness matrix are a consequence of positive off-diagonal coefficients in the local stiffness matrices. The advection positivity scheme eliminates all positive contributions to off-diagonal coefficients of the local stiffness matrices by incorporating these contributions into the diagonal coefficient.

For example, let us assume that the advection coefficient of the left neighboring node is negative. This results in the term  $-a_L\phi_L^{n+1}$  in the numerator of the local  $k$ -equation, viz.

$$\phi_P^{n+1} = \frac{P_k + \frac{\rho}{\Delta t} \phi_P^n + (d_L - a_L)\phi_L^{n+1} + (a_R + d_R)\phi_R^{n+1}}{\frac{\rho}{\Delta t} + a_P + d_P + \rho \frac{\varepsilon_P^m}{\phi_P^m}} \quad (5.12)$$

where the variables  $a$  and  $d$  represent the magnitude of a local advection coefficient and magnitude of a local diffusion coefficient, respectively. The numerator could become negative given a sufficiently large value of  $a_L$ . Thus, we incorporate the coefficient  $a_L$

into the diagonal coefficient by multiplying it by  $\phi_L^m/\phi_P^m$  and making it a coefficient of  $\phi_P^{n+1}$ , resulting in the modified local  $k$ -equation, viz.

$$\phi_P^{n+1} = \frac{P_k + \frac{\rho}{\Delta t} \phi_P^n + d_L \phi_L^{n+1} + (a_R + d_R) \phi_R^{n+1}}{\frac{\rho}{\Delta t} + a_P + a_L \frac{\phi_L^m}{\phi_P^m} + d_P + \rho \frac{\varepsilon_P^m}{\phi_P^m}} \quad (5.13)$$

The numerator and denominator are now both sums of positive terms, guaranteeing a positive solution for  $\phi_P^{n+1}$ . A comparison with Eq. (5.11) shows that the only modification is that the left-neighboring advection coefficient is now a coefficient of  $\phi_P^{n+1}$  rather than  $\phi_L^{n+1}$ . Depending on the sign of  $a_N$  for each nodal point, it is possible, and in fact likely, that different nodal points will have corresponding terms evaluated at different time/iteration steps. However, the converged solutions of variables with superscripts  $m$  and  $n+1$  will be the same. In other words, the terms  $a_L \phi_L^{n+1}$  will equal  $a_L (\phi_L^m/\phi_P^m) \phi_P^{n+1}$  upon convergence. As convergence is approached, the positivity scheme will not be invoked because the standard solution scheme will yield only positive values.

Now, let us consider the case where all off-diagonal advection coefficients of the local stiffness matrix are negative and the diagonal coefficient is also negative. In this case, we choose to replace the term  $a_P \phi_P^{n+1}$  with  $a_P \phi_P^m$ , resulting in the following local  $k$ -equation,

$$\phi_P^{n+1} = \frac{P_k + \frac{\rho}{\Delta t} \phi_P^n + a_P \phi_P^m + (a_L + d_L) \phi_L^{n+1} + (a_R + d_R) \phi_R^{n+1}}{\frac{\rho}{\Delta t} + d_P + \rho \frac{\varepsilon_P^m}{\phi_P^m}} \quad (5.14)$$

Note that both the numerator and the denominator are now sums of positive terms, guaranteeing that the solution of  $\phi_P^{n+1}$  is positive. Also, note that as the solution converges, the value of  $\phi_P^m$  approaches the value of  $\phi_P^{n+1}$  and the positivity scheme will not be invoked.

Finally, there is the possibility that one of the coefficients of a neighboring node is positive and the coefficient of the central node is negative. Consider that it is the coefficient  $a_L$  that is negative. Both procedures mentioned above need to be performed. However, it is desirable that these procedures be implemented in a specific order. The flowchart of Figure 5.1 depicts how the advection positivity scheme has been programmed.

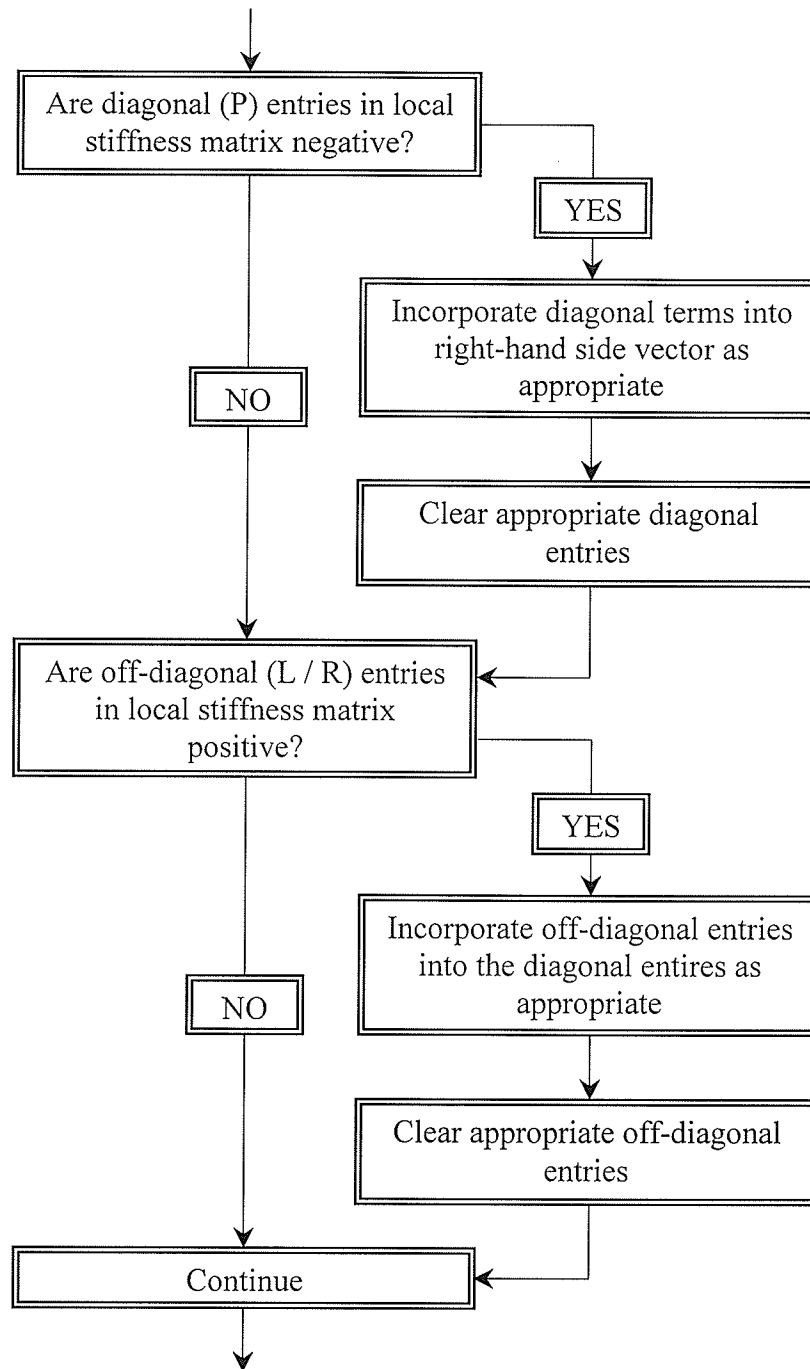


**Figure 5.1: Implementation of the advection positivity scheme**

Following the procedure depicted in Figure 5.1 yields the following equation for  $\phi_p^{n+1}$ :

$$\phi_P^{n+1} = \frac{P_k + \frac{\rho}{\Delta t} \phi_P^n + a_P \phi_P^m + d_L \phi_L^{n+1} + (a_R + d_R) \phi_R^{n+1}}{\frac{\rho}{\Delta t} + a_L \frac{\phi_L^m}{\phi_P^m} + d_P + \rho \frac{\varepsilon_P^m}{\phi_P^m}} \quad (5.15)$$

As required, both the numerator and the denominator are sums of positive terms, guaranteeing that the solution of  $\phi_P^{n+1}$  is positive. Now, let us consider what would happen if we were to check the off-diagonal terms for positive entries before checking the diagonal terms for negative entries. Assuming once again that  $a_L$  is negative, it would be incorporated in the diagonal ( $P$ ) entry of the local stiffness matrix. The resulting diagonal entry would be  $-a_P + a_L (\phi_L^m / \phi_P^m)$ . After this transformation has been performed, the diagonal entry of the stiffness matrix would be checked for a negative entry. If the value of  $-a_P + a_L (\phi_L^m / \phi_P^m)$  were negative, then the subroutine would incorporate this entry into the right-hand side vector, resulting in the following equation for  $\phi_P^{n+1}$ :

$$\phi_P^{n+1} = \frac{P_k + \frac{\rho}{\Delta t} \phi_P^n + \left( a_P - a_L \frac{\phi_L^m}{\phi_P^m} \right) \phi_P^m + d_L \phi_L^{n+1} + (a_R + d_R) \phi_R^{n+1}}{\frac{\rho}{\Delta t} + d_P + \rho \frac{\varepsilon_P^m}{\phi_P^m}} \quad (5.16)$$

A comparison of (5.15) and (5.16) reveals that  $a_L \phi_L^m / \phi_P^m$  has become a coefficient of  $\phi_P^m$ , rather than  $\phi_P^{n+1}$ . Both cases provide the correct answer upon convergence. However, convergence of Eq. (5.16) would presumably be slower than that of Eq. (5.15), thus reducing the efficiency of the CFD code. Now consider the alternate circumstance, in

which the coefficient  $-a_p + a_L(\phi_L^m/\phi_p^m)$  is positive. In this case, the diagonal entry would not be incorporated into the right-hand side vector, resulting in the following equation for  $\phi_p^{n+1}$ :

$$\phi_p^{n+1} = \frac{P_k + \frac{\rho}{\Delta t} \phi_p^n + d_L \phi_L^{n+1} + (a_R + d_R) \phi_R^{n+1}}{\frac{\rho}{\Delta t} + \left( a_L \frac{\phi_L^m}{\phi_p^m} - a_p \right) + d_p + \rho \frac{\varepsilon_p^m}{\phi_p^m}} \quad (5.17)$$

In well-behaved solutions, the diagonal advection terms of the stiffness matrix,  $a_p$ , are positive. The  $a_p$  coefficient is a measure of the weighting of  $\phi$  at the central node when determining the new value of  $\phi$  at that node. An increase in  $a_p$  should result in the solution field becoming more dependent on the value of  $\phi_p$ . The  $a_p$  component of the  $a_L(\phi_L^m/\phi_p^m) - a_p$  coefficient is negative and implies that the solution becoming less dependent on advection (i.e. the diagonal coefficient,  $a_L(\phi_L^m/\phi_p^m) - a_p$ , decreases with an increase of  $a_p$ ). In the limit of  $a_p$  approaching  $a_L(\phi_L^m/\phi_p^m)$ , the dependence of  $\phi_p^{n+1}$  on the advection coefficient of the central node and the left node vanishes.

The advection positivity scheme disallows negative values of  $k$  or  $\varepsilon$  dues to advection terms. Let us now consider the remaining terms in the conservation equations and devise another positivity scheme to completely eliminate negative values in the solution field.

#### 5.4 *Hybrid and Absolute Positivity Schemes*

The advection positivity scheme eliminates the possibility of negative values of  $\phi_p^{n+1}$  due to advection coefficients. It is implemented whenever the standard solution scheme produces a solution field containing at least one negative value. The only terms remaining that could possibly lead to negative values in the solution field are the diffusion terms.

The exact differential terms making up the diffusion term do not lead to negative values in the solution field. The algebraic expressions that are used to approximate the diffusion terms, however, could cause the solution to contain negative results if an intermediate solution contained unrealistically large spatial gradients. It was decided that if negative solutions still persist after invoking the advection positivity scheme, a “hybrid positivity scheme” would be invoked following the same procedures as mentioned above, but considering both the advection and diffusion terms.

The hybrid positivity scheme should eliminate the possibility of positive off-diagonal coefficients in the global stiffness matrix due to advection *and* diffusion terms. If negative solutions persist following invocation of the hybrid positivity scheme, then an “absolute positivity scheme” is invoked. The absolute positivity scheme closely resembles the hybrid positivity scheme with the following difference. All negative, off-diagonal coefficients in the local stiffness matrices become coefficients of  $\phi$  at time level  $m$ . They are incorporated into the solution vector, resulting in an expression for  $\phi_p^{n+1}$  resembling

$$\phi_P^{n+1} = \frac{P_k + \frac{\rho}{\Delta t} \phi_P^n + (a_L + d_L) \phi_L^m + (a_R + d_R) \phi_R^m}{\frac{\rho}{\Delta t} + a_p + d_p + \rho \frac{\varepsilon_P^m}{\phi_P^m}} \quad (5.18)$$

but with various coefficients of neighboring nodal values,  $\phi_N$ , multiplied by  $\phi_P^{n+1}/\phi_P^m$  and thus residing in the denominator. The global stiffness matrix that is generated following the absolute positivity scheme contains only diagonal coefficients, which are all positive, and the solution vector contains only positive values. This guarantees that all solution values are positive. During validation of the  $k$ - $\varepsilon$  turbulence model, only the advection positivity scheme has been required and only during the first two time steps.

A  $k$ - $\varepsilon$  turbulence model now exists that does not suffer from negative solutions or non-physical “clipping”. A summary of the implementation of positivity schemes is shown in Figure 5.2.

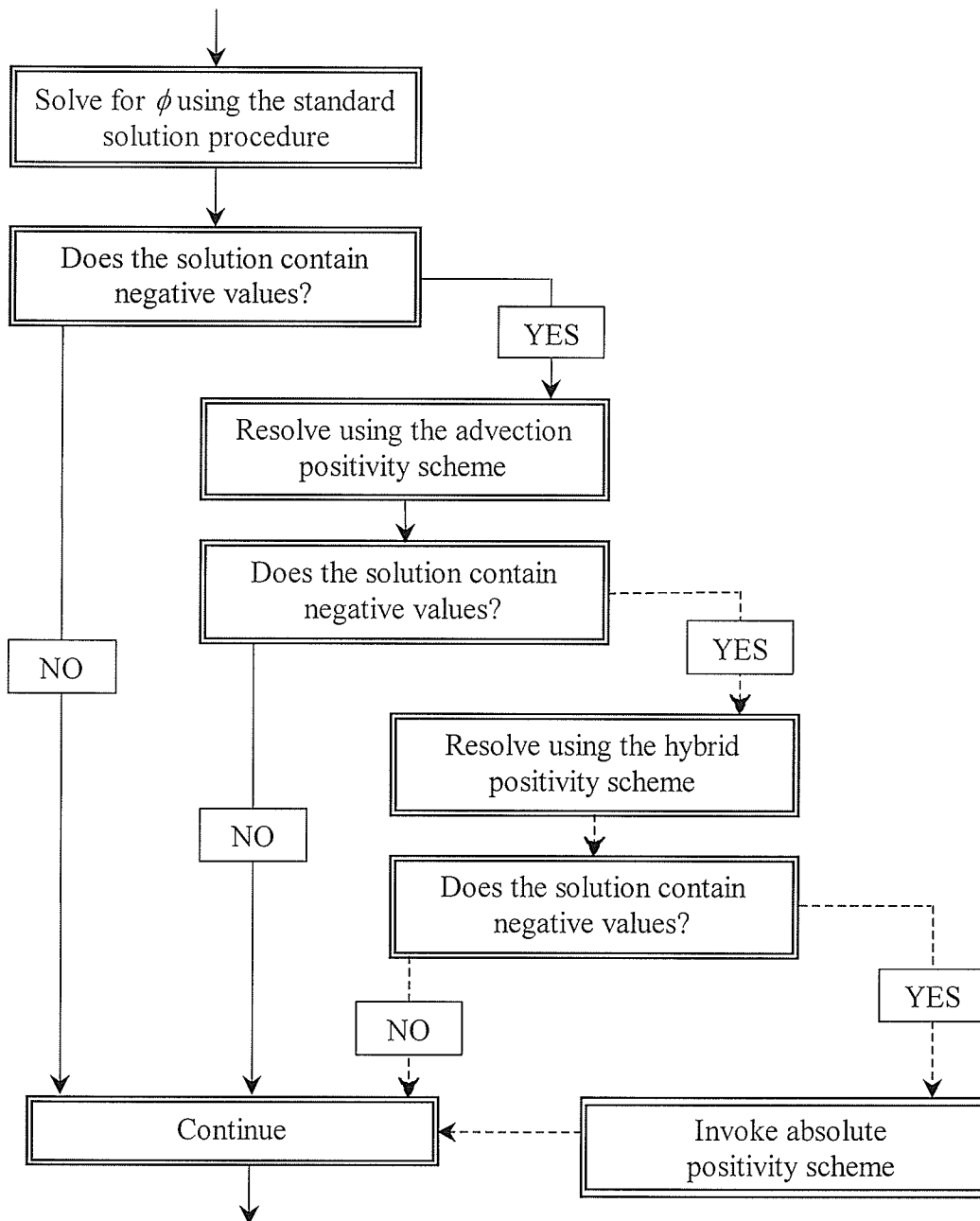


**Figure 5.2: Implementation of the positivity scheme**

A  $k-\varepsilon$  turbulence model with wall functions has been presented that does not suffer from negative solutions. This turbulence model has been used in the simulation of two flows. The first is flow between parallel plates (channel flow), which resembles the ductwork leading into the helicopter engine bay. The second is flow past a backward-facing step.

Both the backward-facing step flow and the flow past helicopter engine bay cooling inlets exhibit separation, a recirculation region and reattachment to the wall. Chapter 6 presents a simulation of channel flow, as well as flow over a backward-facing step.

# Chapter 6: Numerical Results

## 6.1 *Channel Flow Simulation*

In order to ensure that the turbulence model has been correctly formulated and implemented into the CFD code, a few simulations were performed. The first simulations involve turbulent forced convection between two parallel plates. Flow between parallel plates was chosen because it resembles the ductwork leading to the engine bay (Figure 6.1). Also, it produces inlet boundary conditions for a backward-facing step simulation (to be discussed), which resembles the flow beyond engine bay cooling inlets. Simulations were performed at Reynolds numbers consistent with values from the literature so that validation could be performed. A simulation was then performed at the Reynolds number consistent with that of backward-facing step flows in the literature.

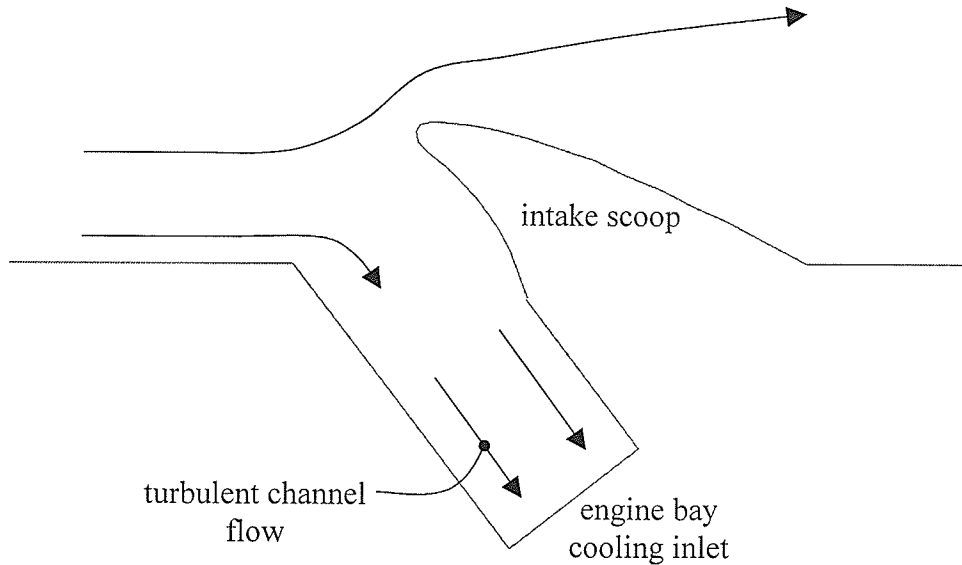


**Figure 6.1: Engine bay cooling inlet configuration**

The channel configurations of Kim et al. (1997), Kim and Moin (1989), Teitel and Antonia (1993) and Mansour et al. (1988) have been adopted. Wilcox (1998) presents results for the velocity field, Reynolds stress and turbulence kinetic energy for both his  $k-\omega$  simulation and a direct numerical simulation (DNS) performed by Mansour et al. Literature results were nondimensionalized using the friction velocity. The friction velocity was determined using an algebraic formulation for channel flow presented by White (1974). The simulation results of Kim et al., Kim and Moin, Teitel and Antonia and Mansour et al. have been adopted to verify the validity of the friction velocity as prescribed by White. The simulations were performed with the parameters used by Wilcox to permit comparisons of the velocity profile, turbulence kinetic energy profile and Reynolds shear stress profile.

It was desired to study the performance of the  $k$ - $\varepsilon$  turbulence model independently of the momentum equations in the previously developed CFD solver. Thus, the fully developed velocity profile of Mansour et al. was imposed. The computed turbulence quantities differed from those of Mansour et al. Thus, various velocity profiles were determined, using  $k$ - $\omega$ , Stress- $\omega$ , Baldwin-Barth, Spalart-Allmaras, Cebeci-Smith, Baldwin Lomax and Johnson-King turbulence models, because it was felt that an error may lie in the production term. The production terms in both the  $k$  and  $\varepsilon$  equations are directly proportional to the velocity gradient and eddy viscosity. It was found that the turbulence quantities calculated by the  $k$ - $\varepsilon$  turbulence model varied greatly between each of the imposed velocity profiles. This indicated that the turbulence quantities of the  $k$ - $\varepsilon$  model are highly sensitive to the velocity gradients through the production terms. These trends will be discussed in the upcoming results.

**(i) Channel Flow Meshes**

A channel flow mesh generation program was written in FORTRAN. The program allows the user to vary most parameters of the channel mesh. The following list shows the parameters that the user may control:

- Channel width and height,
- Height of the boundary elements along all four boundaries,
- Height of refined regions along all four boundaries,

- Number of elements in the vertical direction for entire channel, as well as for the refined regions along the upper and lower boundaries,
- Number of elements in the horizontal direction for entire channel, as well as for the refined regions along the left and right boundaries,
- Separate boundary conditions along all four boundaries for concentration, temperature,  $u$ -velocity,  $v$ -velocity, turbulence kinetic energy and dissipation rate,
- 3 options are available for the inlet  $u$ -velocity including a constant velocity profile, fully developed laminar velocity profile (based on desired centerline velocity) (Oosthuizen, 1999) and fully developed turbulent velocity profile (Danov, 2000),

(NOTE: All of the above options apply a no-slip boundary condition on both of the wall nodes at the channel inlet)

- Initial conditions for concentration, temperature,  $u$ -velocity,  $v$ -velocity, turbulence kinetic energy and dissipation rate.

Given the previous parameters, a mesh file, two boundary condition files and two initial conditions files are generated, with names specified by the user. It is felt that this channel flow mesh generator incorporates all of the necessary features that may be required for comparing with the simulations of other authors.

Two different grids were generated to ensure that the results were grid independent. The lengths of the channels were chosen to be 40 channel widths to ensure fully developed flow at the channel outlet.

## (ii) *Simulation Parameters*

The first parameter selected for the channel flow simulation was the Reynolds number, since it is not possible to nondimensionalize velocity fields such that they collapse onto a single curve for different Reynolds numbers. Figure 6.2 depicts typical dimensionless laminar and turbulent velocity profiles ( $U/U_c$ ) for channel flow. The figure shows that the “nose” of the profile gets flattened out as the Reynolds number increases. Since the nondimensionalized velocity profile varies with Reynolds number, the Reynolds number of the simulations needed to correspond to that of other authors so that a comparison of results could be made. The largest number of simulation results corresponds to the work of Wilcox (1998) with  $Re_m = 6,875$  (based on the bulk velocity and channel half-width). Wilcox also includes DNS results of Mansour et al. Most of the results are nondimensionalized using the friction velocity, even though Wilcox does not present the friction velocity for his simulations. The friction velocity is also a critical parameter that is required when resolving the near-wall region. A way of calculating the friction velocity, based on other flow variables, was thus required.

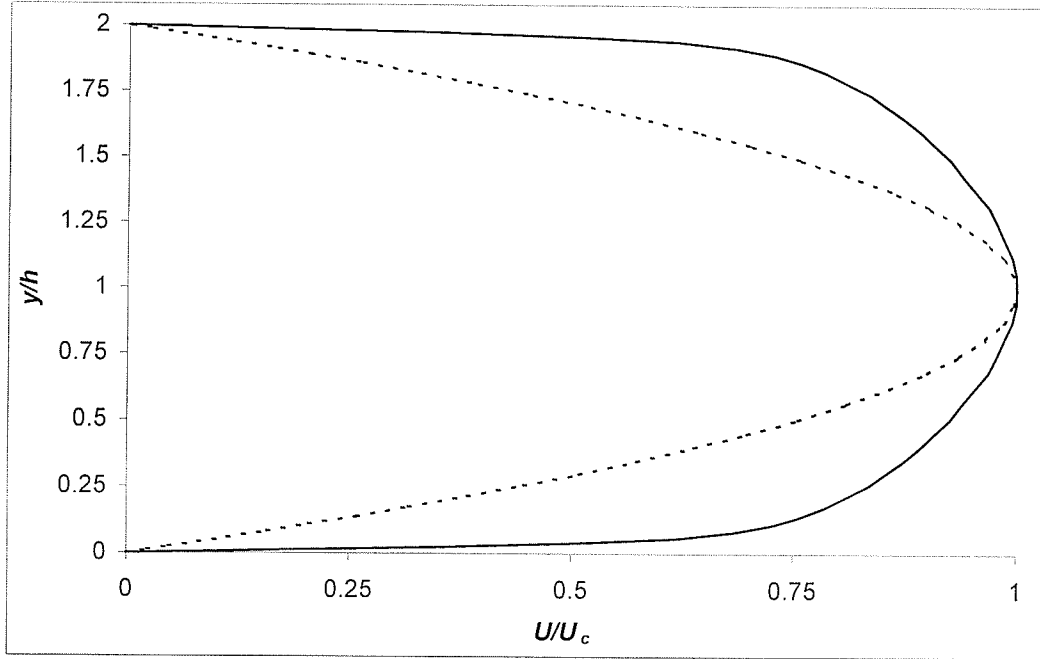


**Figure 6.2: Dimensionless velocity profiles for channel flow: - - -  $Re_m = 100$ , —  $Re_m = 6,875$**

White (1974) provides a formulation for calculating the wall shear stress from the Reynolds number based on the bulk velocity and channel half-width as follows :

$$\tau_w = \frac{\rho U_m^2 \Lambda}{8} \quad (6.1)$$

$$\Lambda \approx 0.495(\log Re_m)^{-2.2} \pm 2\% \quad (6.2)$$

$$Re_m = \frac{U_m h}{\nu} \quad (6.3)$$

We may calculate the friction velocity from the wall shear stress using Eq. (4.3), thereby yielding

$$u_\tau = \sqrt{\frac{U_m^2 \Lambda}{8}} \quad (6.4)$$

In order to verify the reliability of this formulation, we refer to the work of Kim et al., Kim and Moin, Teitel and Antonia and Mansour et al. who all performed channel flow simulations at the same Reynolds number. The Reynolds number based on the bulk velocity and channel half-width was reported to be  $Re_m \approx 2,800$ , corresponding to a Reynolds number based on the friction velocity and channel half-width of  $Re_\tau \approx 180$ , i.e.,

$$Re_m = \frac{U_m h}{\nu} \approx 2,800 \quad (6.5)$$

$$Re_\tau = \frac{u_\tau h}{\nu} \approx 180 \quad (6.6)$$

where  $h$  represents the half-width of the channel. The half-width of the channel for the simulations was chosen to be  $h = 0.021$  m, based on the work of Teitel and Antonia. The working fluid was chosen to be air at 293 K for which  $\nu = 15.09 \times 10^{-6}$  m<sup>2</sup>/s (Oosthuizen, 1999) based on the work of Kim and Moin (1989). For these flows, Eq. (6.5) yields  $U_m \approx 2.012$  m/s, from which Eq. (6.4) gives  $u_\tau \approx 0.12829$  m/s. Substituting  $u_\tau = 0.12829$  m/s into Eq. (6.6) yields  $Re_\tau = 178.529$ . This suggests that Eq. (6.4) provides an accurate

friction velocity if the Reynolds number, based on the bulk velocity and channel half-width, is known.

The Reynolds number of Wilcox's simulations was  $Re_m = 6,875$ . Assuming  $h = 0.021$  m and  $\nu = 15.09 \times 10^{-6}$  m<sup>2</sup>/s yields a bulk velocity of  $U_m = 4.94$  m/s. Applying Eq. (6.4) yields a friction velocity of  $u_\tau = 0.2799$  m/s. A constant inlet velocity of  $U_i = 4.94$  m/s yields the correct mass flow rate through the channel but violates the no-slip condition at the channel walls. The mass flow rate through the channel (without imposing the no-slip velocity condition) was calculated to be  $\dot{m} = 0.12492$  kg/m<sup>3</sup>, assuming a unit channel depth. The approximate heights of the wall elements were determined by ensuring that the first interior nodes were located in the log layer. This requires that the dimensionless distance between the first interior node and the wall lie within the range between  $y^+ = 30$  and  $y^+ = 100$ . Choosing  $y^+ = 50$  and assuming  $u_\tau = 0.2799$  m/s leads to a wall element height of

$$\Delta = \frac{y^+ \nu}{u_\tau} \approx 0.002625 \text{ m} \quad (6.7)$$

The trapezoid rule was then used to determine that a constant inlet velocity of  $U_i = 5.27$  m/s produces a mass flow rate of  $\dot{m} \approx 0.12494$  kg/m<sup>3</sup>, assuming a no-slip velocity condition is applied at the two wall nodes at the channel inlet. An inlet velocity of  $U_i = 5.27$  m/s should yield the desired bulk velocity for the fully developed turbulent flow at

the channel outlet. A zero  $y$ -direction velocity was also imposed at the channel inlet. The resulting channel configuration is shown in Figure 6.3

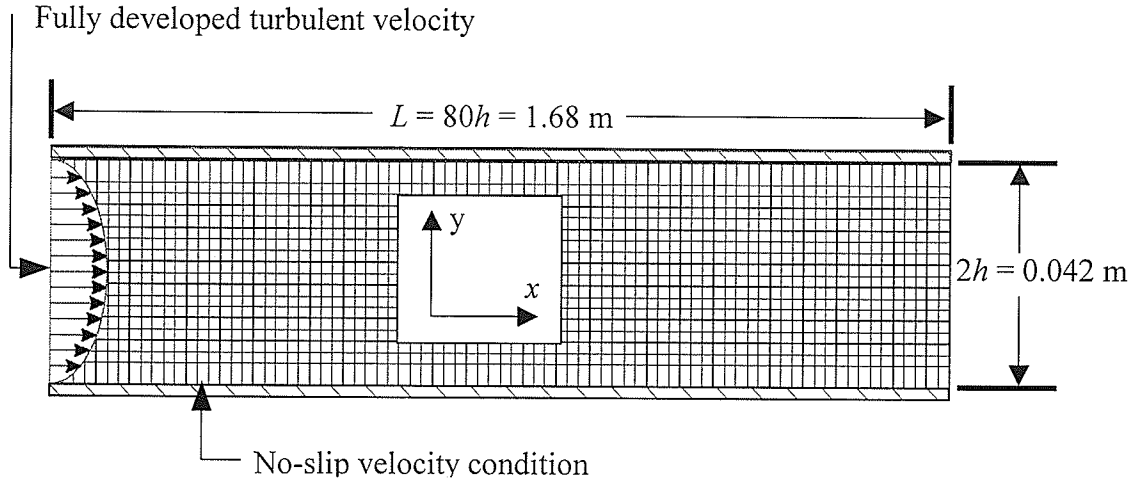


**Figure 6.3: Channel flow configuration**

The inlet values of the turbulence kinetic energy,  $k_i$ , and dissipation rate,  $\varepsilon_i$ , were determined based on the expected wall shear stress of the fully developed channel flow, i.e.,

$$k_i = \frac{u_\tau^2}{\sqrt{c_\mu}} \approx 0.261 \text{ m}^2/\text{s}^2 \quad (6.8)$$

$$\varepsilon_i = \frac{u_\tau^3}{\kappa \Delta} \approx 20.375 \text{ m}^2/\text{s}^3 \quad (6.9)$$

These inlet values of  $k$  and  $\varepsilon$  should produce a relatively smooth profile across the channel inlet. Next, the initial values of the turbulence kinetic energy,  $k_0$ , and dissipation rate,  $\varepsilon_0$ , were determined. Their values will not affect the final solutions, but they are

critical in providing a reasonable initial solution of the velocity field. The initial eddy viscosity is calculated based on the initial values of  $k_0$  and  $\varepsilon_0$  as

$$\nu_{T,0} = c_\mu \frac{k_0^2}{\varepsilon_0} \quad (6.10)$$

The initial eddy viscosity is added to the kinematic viscosity and passed to the momentum equations. It was found that if  $\nu_{T,0}$  is too small, the solution of the momentum equations will not stabilize. The resulting velocity field will be nonphysical. The initial values of the turbulent quantities were thus chosen such that a Reynolds number based on  $U_m$ , channel width,  $H$ , and  $\nu_{T,0}$  has a value of approximately  $Re = 100$ . This requires an eddy viscosity of approximately  $\nu_T = 0.00207 \text{ m}^2/\text{s}$ . Assuming an arbitrary value of  $k_0 = 0.1 \text{ m}^2/\text{s}^2$  yields  $\varepsilon_0 = 0.435 \text{ m}^2/\text{s}^3$ . The velocity field after the first time step should match that of a laminar flow with  $Re = 100$ .

A summary of the simulation parameters used in this study is presented in Table 6.1.

Mesh Property	Units	Value
channel height	m	0.042
channel width	m	1.68
height of wall elements	m	0.002625
number of horizontal elements	-	75
number of vertical elements	-	20/60

Fluid Property	Units	Value
density	kg / m <sup>3</sup>	1.2042
kinematic viscosity	m <sup>2</sup> / s	15.09×10 <sup>-6</sup>
thermal conductivity	W / m	25.64×10 <sup>-3</sup>
specific heat	kJ/kg K	1.0061

Simulation Property	Units	Value
number of time steps	-	100
time step size	s	10
maximum number of velocity iterations	-	20
velocity convergence tolerance	%	0.1
maximum number of $k$ - $\epsilon$ iterations	-	20
eddy viscosity convergence tolerance	%	0.1

Boundary Conditions	Units	Inlet	Outlet	Wall
concentration	-	$C = 0$	zero flux	zero flux
temperature	K	$T = 273$	zero flux	zero flux
turbulence kinetic energy	m <sup>2</sup> / s <sup>2</sup>	$k = 0.261$	zero flux	wall function
dissipation rate	m <sup>2</sup> / s <sup>3</sup>	$\epsilon = 20.375$	zero flux	wall function

Initial Conditions	Units	Value
concentration	-	$C = 0$
temperature	K	$T = 273$
turbulence kinetic energy	m <sup>2</sup> / s <sup>2</sup>	$k = 0.1$
dissipation rate	m <sup>2</sup> / s <sup>3</sup>	$\epsilon = 0.435$

Table 6.1: Parameters used in channel flow simulations

### (iii) *Full Simulation*

A channel flow was simulated using the parameters of Table 6.1. The velocity profile predicted from the momentum equations of the CFD solver differs from the results of Mansour et al. The CFD solver has been widely tested and validated for laminar flows involving a constant viscosity (i.e. Naterer, Schneider, 1995b). However, new issues appear in regards to the detailed impact of spatially varying viscosity as it arises in turbulent flows. For example, differences in the treatment of influence coefficients with PINS may affect the calculations of advecting and linearized advected velocities in the momentum equations. These detailed coupling, involving integration point modeling and full integration into the multiphase flow solver, are considered to lie outside the scope of this thesis. Instead, implementation of the  $k$ - $\varepsilon$  equations is tested independently by using and comparing results with various velocity profiles from different turbulence models.

Any errors in the predicted velocities can largely affect the calculation of the production terms in both the equations for  $k$  and  $\varepsilon$ . For example, these production terms may be artificially large, being proportional to a sum of squares of velocity gradients. If the velocity error at each node was 10 % (over-predicted), the error in the production term at each node, due solely to the error in velocity, would be 21 %. Production of  $k$  is also directly proportional to the eddy viscosity, which is directly proportional to  $k^2$  and inversely proportional to  $\varepsilon$ , indicating that the magnitude of the production term is further affected by any error in the production term. This sensitivity of predicted turbulence quantities due to variations of velocity profiles will be studied in the next section.

#### (iv) *U-Specified Simulation*

The velocity profile of Mansour et al., as presented by Wilcox (1998), was curve fitted by Microsoft Excel as a function of  $y/h$ . This curve was used to specify the DNS velocity profile at every point within the channel. The prediction of all turbulence quantities was made with the current  $k-\varepsilon$  model and CFVEM. It was discovered that the turbulence quantities are highly dependent on the velocity profile. As a results, more velocity profiles were desired.

DCW Inc. (Wilcox, 1998) provides a program (**PIPE**) that computes incompressible, fully developed flow in either a two-dimensional channel or a pipe of circular cross section. **PIPE** was run with various turbulence models at  $Re_\tau = 395$ . For this flow,  $u_\tau$  was assumed to be 0.279948 m/s from Eqs. (6.3) and (6.4) with  $Re_m = 6,875$ . **PIPE** provides, among other outputs, the dimensionless  $u$ -velocity profile at the channel outlet. **PIPE** was run for seven different turbulence models. These turbulence models are identified as follows.

#### **Algebraic models**

**A3** - 3 closure coefficients

**A6** - 6 closure coefficients

#### **½-Equation model**

**H7** – 7 closure coefficients

### **One-Equation models**

**O7** – 7 closure coefficients, 3 empirical damping functions

**O8** – 8 closure coefficients, 3 closure functions

### **Two-Equation model**

**T5** – 5 closure coefficients, 6 auxiliary relations

### **Stress-Transport model**

**S10** – 10 closure coefficients, 6 auxiliary relations

The predicted  $U^+$  profiles were curve-fit using Microsoft Excel as functions of  $y/h$ . These curves, used to specify the  $u$ -velocity profile after being dimensionalized using  $u_\tau = 0.2799$  m/s, are shown in Figure 6.4. The shapes and magnitudes of these  $u$ -velocity profiles vary significantly, depending on which turbulence model had been used.

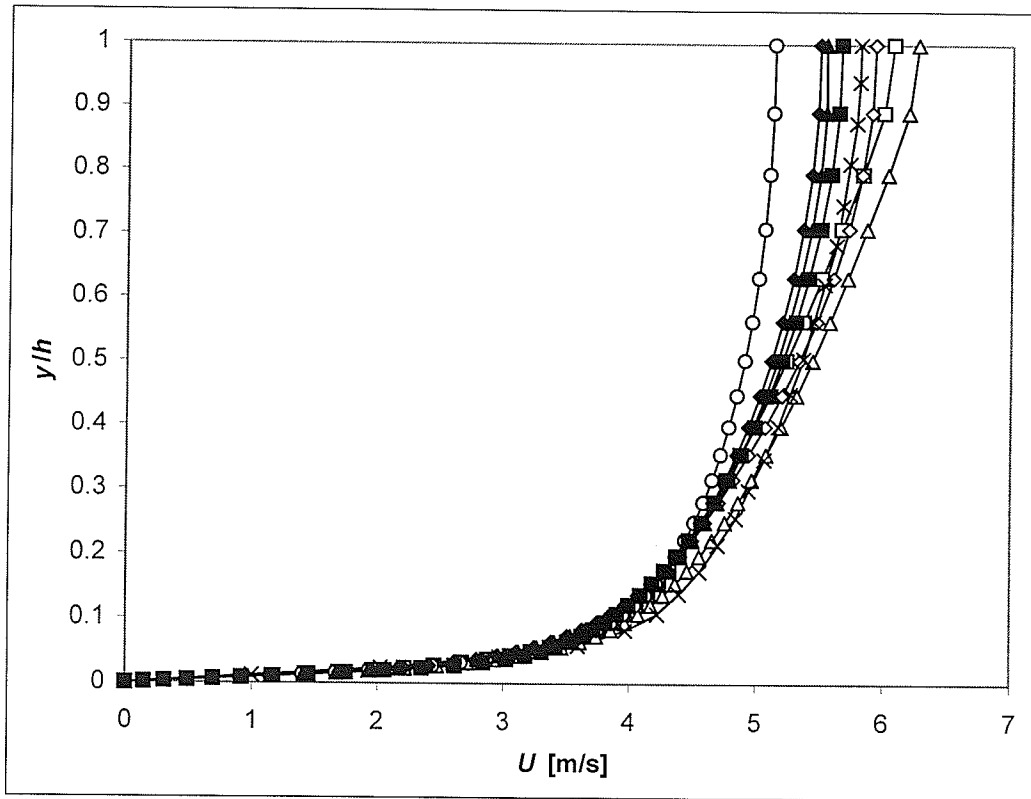


**Figure 6.4: U-Velocity profiles predicted using various turbulence models:**  
 —□— A3, —◇— A6, —△— H7, —○— O7, —■— O8, —◆— T5, —▲— S10,  
 —×— Mansour et al.

The turbulence kinetic energy profiles, shown in Figure 6.5, varied considerably depending on which velocity profile had been specified. Figure 6.5 shows the profiles that were calculated using velocity profiles from the one-equation models, the two-equation model, the stress-transport model and the DNS simulation of Mansour et al. (labeled DNS). The curves corresponding to the algebraic and  $\frac{1}{2}$ -equation models all showed poorer agreement with the DNS results. Also, the  $k$ -profile of Mansour et al. is shown for comparison. Most of the curves show a maximum at the first interior node, which is expected. The T5 curve shows the closest agreement, which is encouraging because the T5 model and the present  $k$ - $\varepsilon$  model are both two-equation models.

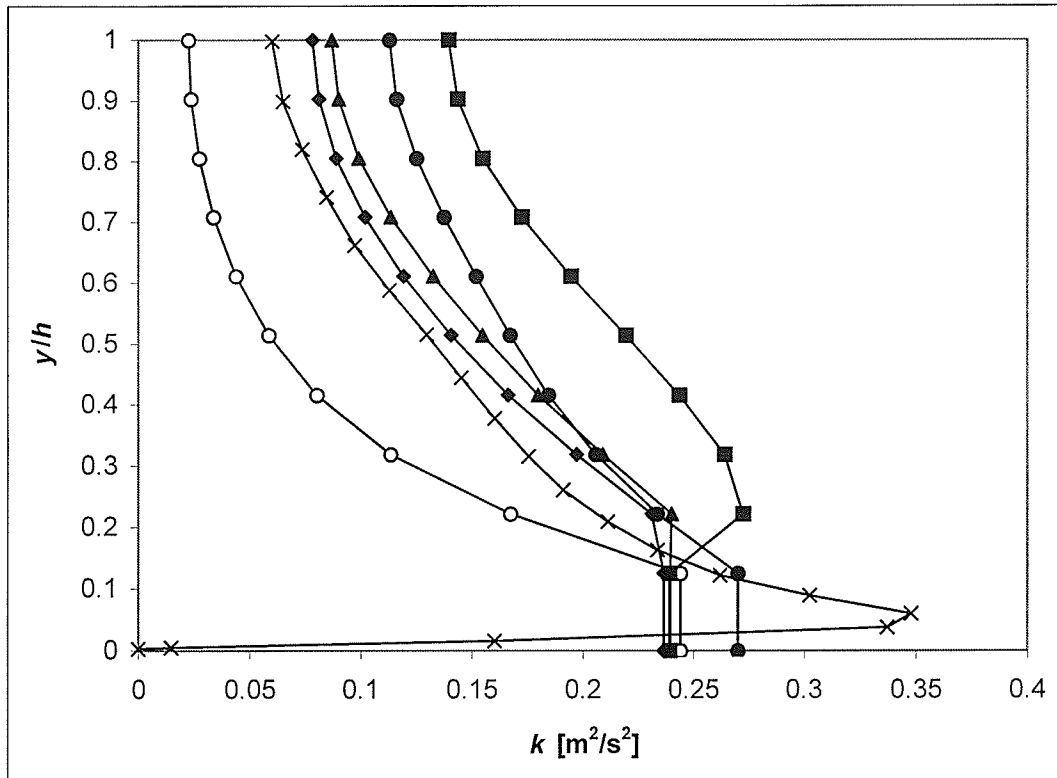


**Figure 6.5: Turbulence kinetic energy profiles: —○— O7, —■— O8, —◆— T5, —▲— S10, —●— DNS, —×— Mansour et al.**

The Reynolds-stress profiles, shown in Figure 6.6, also varied considerably depending on which velocity profile had been specified. Again, the T5 curve shows the closest agreement with the DNS results, which is encouraging. The thicker solid black line represents the total shear stress. The Reynolds stress that was predicted by the DNS simulation closely matches the total shear stress away from the wall where the shear due to molecular viscosity is negligible. Also, the Reynolds shear stress becomes zero at the channel centerline where there is zero velocity gradient and at the channel wall where the eddy viscosity becomes negligible.

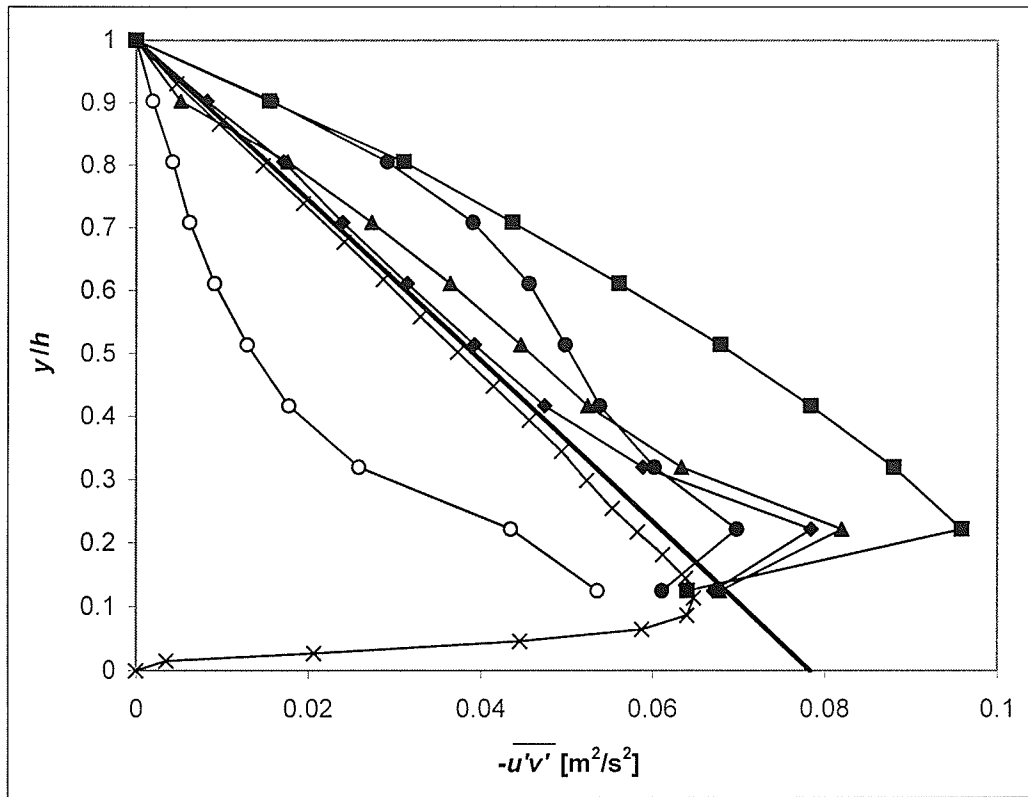


**Figure 6.6: Reynolds-stress profiles: —○— O7, —■— O8, —◆— T5, —▲— S10, —●— DNS, —×— Mansour et al.**

The grid was refined in order to determine how much the sparseness of the mesh was contributing to the discrepancies. The simulations were again performed with 60 elements across the channel using the T5  $u$ -velocity profile. These results are shown in Figures 6.6 and 6.7, with the results from the refined simulation labeled “60”. As expected, the results have improved considerably.

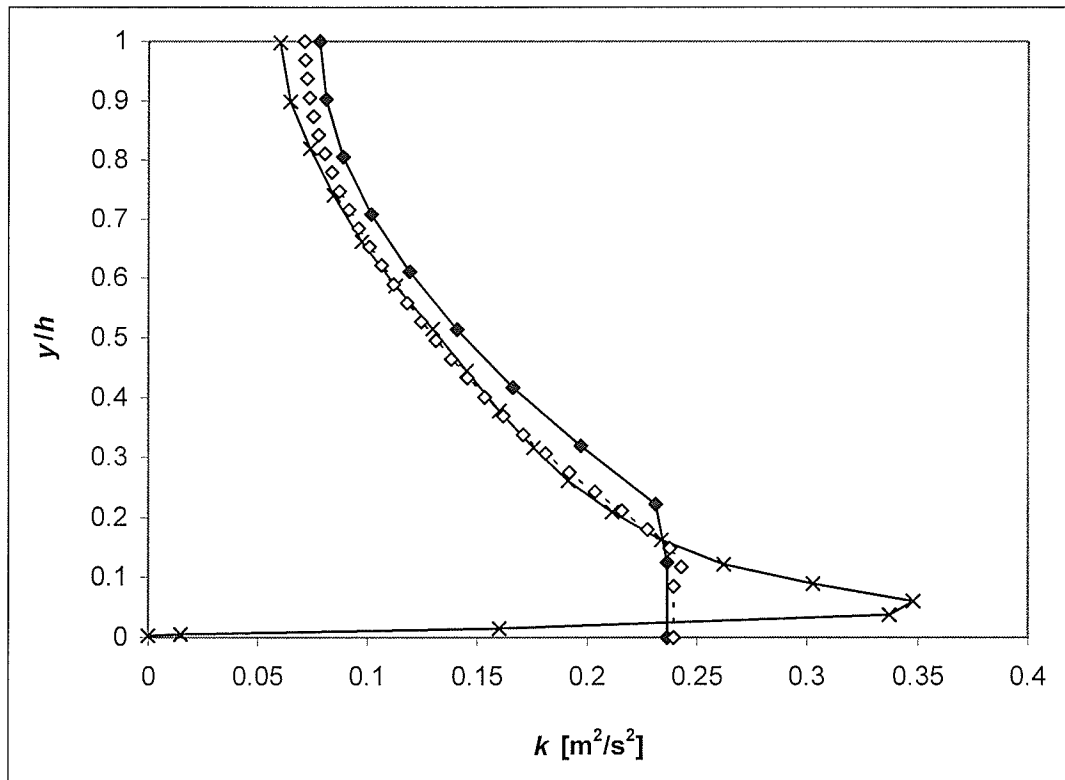


**Figure 6.7: Turbulence kinetic energy profiles: —♦— T5, - - ♦ - - 60, —x— Mansour et al.**

It is worth noting that the  $k$ - $\omega$  simulations performed by Wilcox do not exactly match the DNS results of Mansour et al. In fact, Wilcox's  $k$ -profile is in significant error across a majority of the channel. It is possible that the DNS simulations are predicting turbulence quantities with an accuracy that is beyond the capabilities of a two-equation model. In such a case, we cannot expect the prediction of the turbulence quantities to exactly match those of Mansour et al.

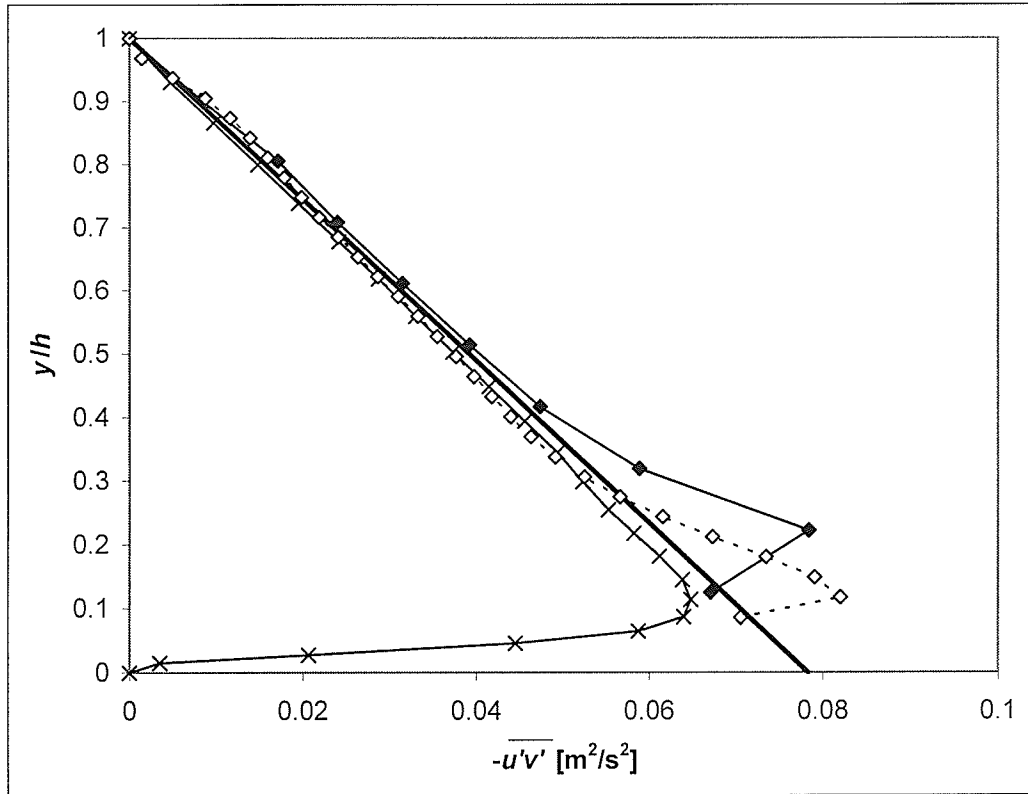
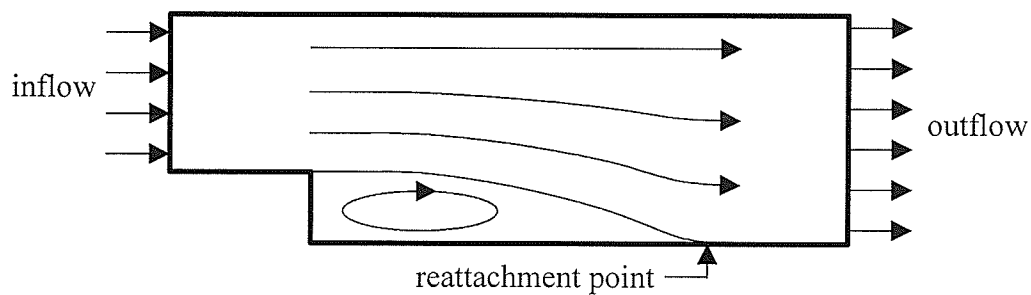


Figure 6.8: Reynolds-stress profiles: —♦— T5, --♦-- 60, —×— Mansour et al.

The previous results have shown that the current  $k-\varepsilon$  model predicts the turbulence quantities in reasonable agreement with DNS results what a two-equations (T5) based velocity profile is used. These comparisons were intended to validate the  $k-\varepsilon$  equations themselves (not full coupling with the momentum and multiphase equations). Furthermore, additional attempts to combine the mean flow and  $k-\varepsilon$  equations will be described in the following section. The channel flow simulation (this section) was selected in part because it provides the inlet boundary conditions for a backward-facing step simulation (next section).

## 6.2 Flow Over a Backward-Facing Step

A channel flow simulation was performed to ensure that the present  $k-\varepsilon$  turbulence model has been correctly formulated and properly implemented into the CFD code. The simulations predicted reasonable trends of the turbulence quantities. Proper formulation and implementation of the present  $k-\varepsilon$  turbulence model can be checked in regards to whether the model predicts turbulence quantities that yield a reasonable reattachment length past the backward-facing step (BFS). Figure 6.9 is a schematic of the BFS flow.



**Figure 6.9: Backward-facing step flow configuration**

### (i) Backward-Facing Step Meshes

A BFS mesh generation program was written in FORTRAN. The program allows the user to vary most parameters of the BFS mesh. The following list shows the parameters that the user may control:

- Channel width and height upstream and downstream of the step,
- Height of the wall boundary elements, including the step,

- Height of refined regions along the lower portion of the upstream channel and the upstream portion of the downstream channel,
- Number of elements in the vertical direction for each channel, as well as for the refined region in the upstream channel,
- Number of elements in the horizontal direction for each channel, as well as for the refined region of the downstream channel,
- Separate boundary conditions along all four boundaries (step is included in lower boundary) for concentration, temperature,  $u$ -velocity,  $v$ -velocity, turbulence kinetic energy and dissipation rate,
- Initial conditions for concentration, temperature,  $u$ -velocity,  $v$ -velocity, turbulence kinetic energy and dissipation rate.

Given the above parameters, a mesh file, two boundary condition files and two initial conditions files are generated, with names specified by the user. This BFS mesh generator was used to generate the BFS mesh in the simulation presented in this chapter. The inlet conditions, which were set equal to the outlet predictions of a channel flow simulation, were input manually using Microsoft Excel.

**(ii) *Simulation Parameters***

The BFS configuration of Thangam and Speziale (1992), Kim et al. (1980) and Eaton and Johnson (1980) was selected. The expansion ratio,  $E$ , defined as the ratio of the step height to the outlet channel height, is 1:3. The Reynolds number based on the inlet

centerline velocity and the outlet channel height is  $Re_c = 132,000$ . The step height was arbitrarily chosen to be  $h = 0.1$  m and the working fluid was chosen to be air at 293 K, for which the kinematic viscosity is  $\nu = 15.09 \times 10^{-6}$  m<sup>2</sup>/s (Oosthuizen, 1999). These properties yield a centerline velocity of  $U_c = 3.6396$  m/s.

A channel flow simulation was performed to obtain the inlet boundary conditions for the BFS simulation. The parameters used for the channel flow simulation are shown in Table 7.1. The profiles of  $u$ -velocity, turbulence kinetic energy and specific dissipation rate, which were predicted at the channel outlet, are shown in Figure 6.10.

The predicted centerline velocity is  $U_c = 6.637$  m/s, yielding  $Re_c = 87,966$ . This agrees well with the desired result of  $Re_c = 88,000$ , which should yield a Reynolds number of 132,000 for the BFS simulation.

Mesh Property	Units	Value
channel height	m	0.2
channel width	m	1.0
height of wall elements	m	0.006
number of horizontal elements	-	75
number of vertical elements	-	20

Fluid Property	Units	Value
density	kg / m <sup>3</sup>	1.2042
kinematic viscosity	m <sup>2</sup> / s	15.09×10 <sup>-6</sup>
thermal conductivity	W / m	25.64×10 <sup>-3</sup>
specific heat	kJ/kg K	1.0061

Simulation Property	Units	Value
number of time steps	-	100
time step size	s	10
maximum number of velocity iterations	-	20
velocity convergence tolerance	%	0.1
maximum number of $k$ - $\varepsilon$ iterations	-	20
eddy viscosity convergence tolerance	%	0.1

Boundary Conditions	Units	Inlet	Outlet	Wall
concentration	-	$C = 0$	zero flux	zero flux
temperature	K	$T = 273$	zero flux	zero flux
$u$ -velocity	m / s	$u = 5.93$	zero flux	$u = 0$
$v$ -velocity	m / s	$v = 0$	zero flux	$v = 0$
turbulence kinetic energy	m <sup>2</sup> / s <sup>2</sup>	$k = 0.1$	zero flux	wall function
dissipation rate	m <sup>2</sup> / s <sup>3</sup>	$\varepsilon = 0.5$	zero flux	wall function

Initial Conditions	Units	Value
concentration	-	$C = 0$
temperature	K	$T = 273$
$u$ -velocity	m / s	$u = 0$
$v$ -velocity	m / s	$v = 0$
turbulence kinetic energy	m <sup>2</sup> / s <sup>2</sup>	$k = 0.232$
dissipation rate	m <sup>2</sup> / s <sup>3</sup>	$\varepsilon = 0.4287$

Table 6.2: Parameters used in the channel flow simulation were used to obtain inlet boundary conditions for the backward-facing step simulation

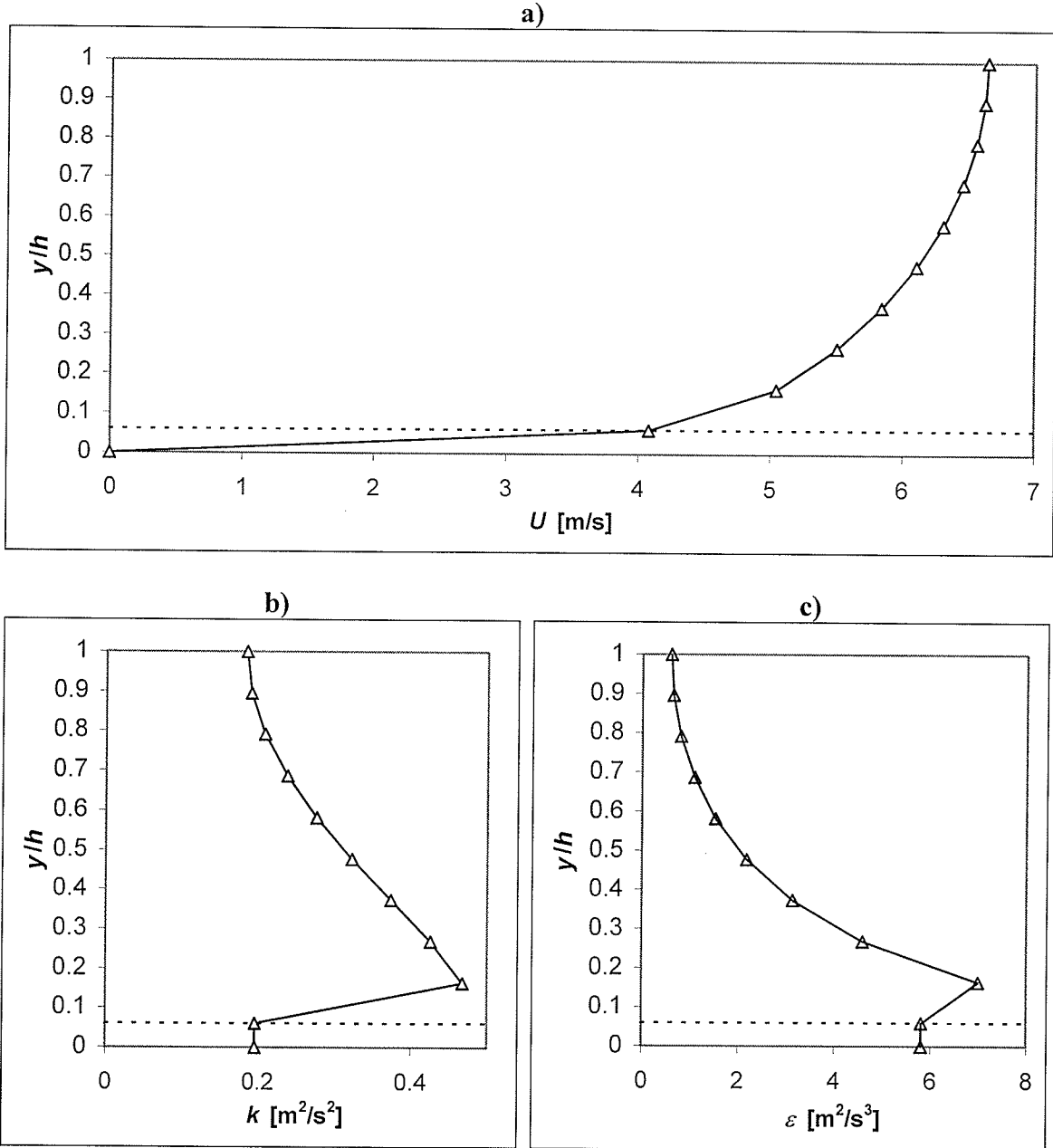


**Figure 6.10:** Predicted properties at the channel outlet that were used as inlet boundary conditions for the backward-facing step simulation: a)  $u$ -velocity b) turbulence kinetic energy, c) specific dissipation rate

### (iii) *BFS Simulation*

Flow over a BFS was simulated based on the parameters of Table 6.3. A parameter of comparison in this study is the reattachment length in terms of the step height. A vector representation of the predicted velocity field is depicted in Figure 6.11. This vector map shows the reattachment length to be approximately  $l_R = 5.35$  step heights, which represents an approximate 25% underprediction. Experimental results of Eaton and Johnson indicate a reattachment length of 7.1 step heights (Thangam, 1991). However, earlier reported results indicate that the  $k-\varepsilon$  model under-predicts the reattachment length by 20-25 % (Thangam, 1991). Furthermore, appreciable differences in experimental data have been reported for turbulent flows over a backward-facing step. For example, Durot and Schmitt (1985) use 2-channel LDA, but integrated  $U$ -velocity profiles have a 10 % difference between inlet and outlet mass flow rates. Also, other differences arise when measurements are taken with pitot tubes, as compared with hot wire or LDA methods. In view of these discrepancies, the current predicted results appear reasonable, both in terms of the qualitative features of the predicted velocities, and the reattachment length.

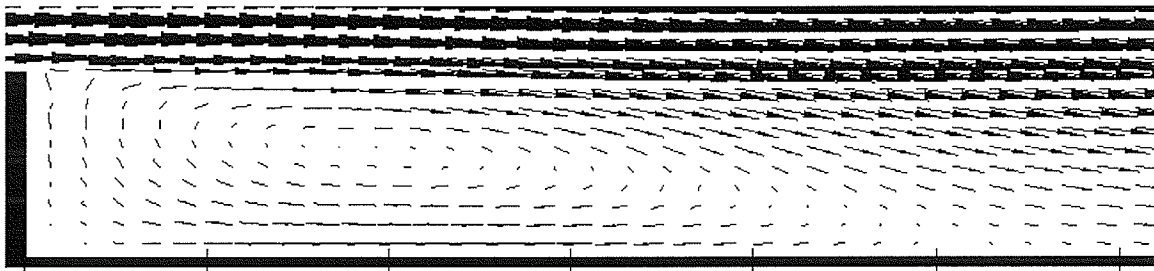


**Figure 6.11: Vector map of the predicted velocity field in the recirculation zone indicating a reattachment length of approximately 5.35 step heights, an underprediction of approximately 25%**

The results of the BFS simulation are encouraging and suggest that the  $k-\varepsilon$  turbulence model has been correctly formulated and properly implemented.

Upstream Mesh Property	Units	Value
channel height	m	0.2
channel width	m	0.5
height of wall elements	m	0.006
number of horizontal elements	-	25
number of vertical elements	-	20

Downstream Mesh Property	Units	Value
channel height	m	0.3
channel width	m	3.0
height of step wall elements	m	0.0
height of upper and lower wall elements	m	0.006
number of horizontal elements	-	60
number of vertical elements	-	30

Fluid Property	Units	Value
density	kg / m <sup>3</sup>	1.2042
kinematic viscosity	m <sup>2</sup> / s	15.09×10 <sup>-6</sup>
thermal conductivity	W / m	25.64×10 <sup>-3</sup>
specific heat	kJ/kg K	1.0061

Simulation Property	Units	Value
number of time steps	-	100
time step size	s	10
maximum number of velocity iterations	-	20
velocity convergence tolerance	%	0.1
maximum number of $k-\varepsilon$ iterations	-	20
eddy viscosity convergence tolerance	%	0.1

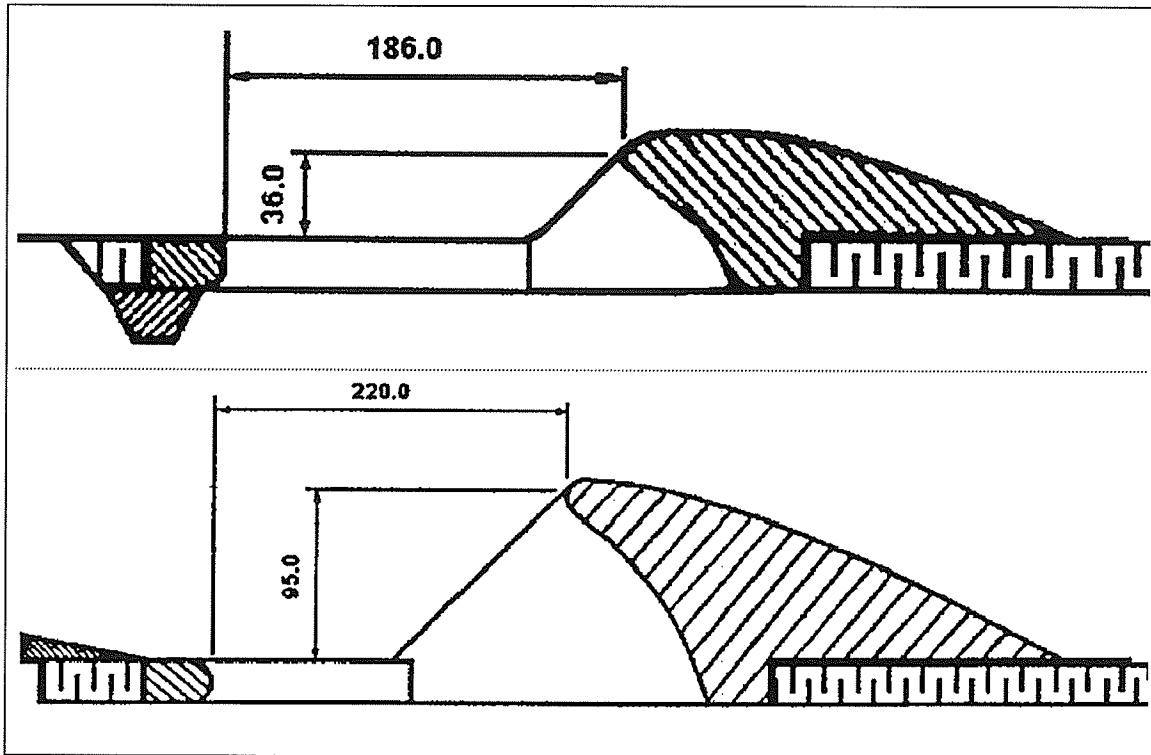
Initial Conditions	Units	Value
concentration	-	$C = 0$
temperature	K	$T = 273$
$u$ -velocity	m / s	$u = 0$
$v$ -velocity	m / s	$v = 0$
turbulence kinetic energy	m <sup>2</sup> / s <sup>2</sup>	$k = 1.0$
dissipation rate	m <sup>2</sup> / s <sup>3</sup>	$\varepsilon = 4.76$

Table 6.3: Parameters used in the BFS simulation

# Chapter 7: Particle Image Velocimetry

## Measurements

The previously developed two-dimensional multiphase CVFEM CFD code now includes a  $k$ - $\varepsilon$  turbulence model. This allows the CFD code to be applied to turbulent flows. An initial motivation for incorporating the turbulence model was to investigate the icing of helicopter engine bay cooling inlets (EBCIs). This inlet of the helicopter represents a rather complex geometry, as shown in Figures 7.1 and 7.2. An accurate prediction of the velocity fields is vital when predicting icing of the EBCIs. Unfortunately, the actual velocity fields past the EBCIs are unknown, so validation of numerical predictions requires new experimental data.



**Figure 7.1: Schematics of helicopter components: TOP) No. 1 and 3 engine bay cooling inlets, BOTTOM) No. 2 engine bay cooling inlet. Note: units are in mm**

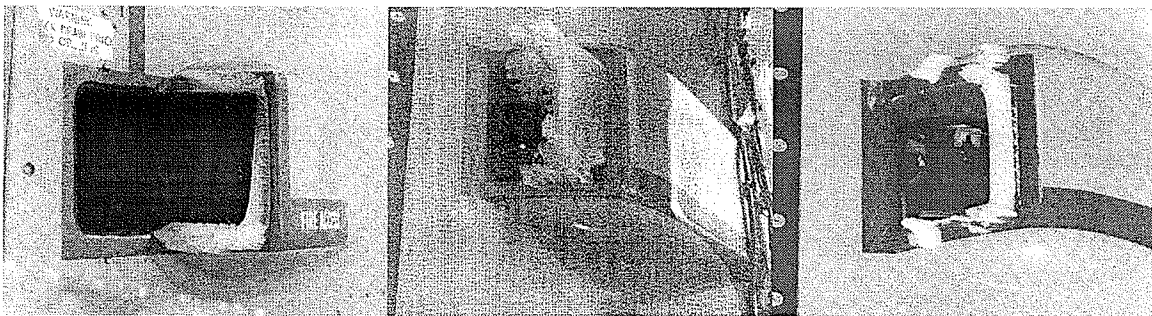


**Figure 7.2: Pictures of ice accretion on the leading edges of helicopter engine bay cooling inlets**

The measured velocity fields past the EBCIs must be known in order to fully validate the numerically predicted velocity fields. Particle image velocimetry (PIV) has been used to measure the velocity fields past bluff bodies resembling the EBCIs. The geometries of the bluff bodies do not exactly match those of the EBCIs. At this time, the body of the

helicopter upstream and downstream of the EBCIs is not replicated, nor is the ductwork within the helicopter. The purpose of the current studies is to measure the flow field past bluff bodies resembling the EBCIs, against which numerical predictions may be compared. Numerical simulation of the flow past the bluff bodies can later assess the CFD code's ability to predict the flows past the EBCIs.

### 7.1 *Particle Image Velocimetry Background*

PIV is an instantaneous full-field velocity measurement technique. A PIV system consists of particle seeding, an illumination system, a recording system, a processing system and an analysis system [Dantec, 1998], each of which is described in the following sections. The illumination component of the PIV system illuminates the area of the flow that is measured. Seeding particles residing in the fluid reflect the light cast by the illumination system towards a recording device. The recorded images are transferred to a processing system. Here the images are correlated into raw vector maps using Fast Fourier Transforms (FFT). The vector maps may be subsequently analyzed by the analysis system to refine the raw vector maps and derive other information, such as streamlines and vortices.

The basic equation used in PIV measurements of the motion of neutrally buoyant particle tracking in the flow is

$$speed = \frac{displacement}{time} = \frac{\Delta D}{\Delta t} \tag{7.1}$$

In order to determine the displacement of a particle, two successive images of a flow are captured  $\Delta t$  seconds apart. The image is then divided into smaller areas, termed interrogation regions. One such interrogation region is shown in Figure 7.3. Cross-correlation is used to determine the average shift in particle positions between the two frames. Each interrogation region yields one velocity vector.

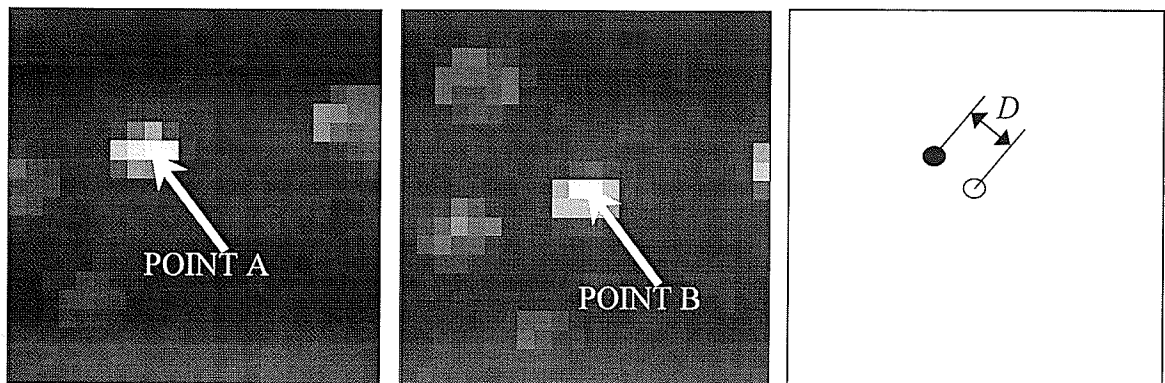


**Figure 7.3: Interrogation region showing the shift in the position of a particle between time  $t$  and time  $t+\Delta t$ : a) Image from first frame at time  $t$  and b) Image from second frame at time  $t+\Delta t$  and c) Shift in particle position from frame 1 to frame 2**

## 7.2 Seeding

The correlation unit attempts to determine the average shift in the location of the particles from one instant in time to another. This requires that the correlation system be must given an indication of where the fluid element is “located”. To this end, the fluid is impregnated with seeding particles. The small seeding particles are assumed to exactly follow the flow. This requires that the particles are approximately neutrally buoyant. The capability of using these neutrally buoyant particles over a range of flow velocities represents an important advantage of flow visualization in water tunnels over wind

tunnels. The correlation system determines the average change in the position of a group of particles within an interrogation region, which is assumed to match the bulk change in position of the fluid element in that region. The particles must be highly reflective in order to reflect light from the illumination system towards the recording medium. The diameter of the particles is also important when determining the location of a particle. Polyamide seeding particles with a mean diameter of 20 microns were used in this research.

### **7.3 *Illumination***

The seeding particles in the flow reflect a majority of the arriving light both forward and backwards (Dantec, 1998). Unfortunately, the recording device detects only the light that the particles reflect laterally. This demands that the region of the flow to be recorded must be intensely illuminated. A New Wave Gemini double pulsed Nd: Yag laser was used in this research. This laser emits infrared radiation at a wavelength of 1064 nm (New Wave Research, 2000). The infrared beam is doubled to 532 nm by passing it through an angle tuned KTP crystal and it falls within the visible spectrum as green light. The Nd: Yag laser pulses only at 1 Hz or 16 Hz. The time between images (required for cross-correlation) range from 100 and 400  $\mu$ s in this research, thereby requiring that the flow is illuminated between 2,500 Hz and 10,000 Hz. This is accomplished with a double cavity Nd: Yag laser system, whereby two laser beams, emitted by two lasing cavities and aligned with various optics, are emitted  $\Delta t$  seconds apart. In order to obtain short bursts of light, the lasing cavities are Q-switched during the maximum flash lamp

intensities. The two flash lamps and two Q-switches are synchronized by a synchronization system in the PIV processor.

#### **7.4 Recording**

Raw vector maps are generated by correlating two successive images of the flow. The images show the location of the seeding particles at two instances in time, which are assumed to exactly follow the flow. A Kodak MegaPlus ES 1.0 Charge Coupled Device (CCD) camera was used to capture the flow images in this research. The CCD chip includes  $1008 \times 1016$  light-sensitive cells, each with a corresponding storage cell (Eastman Kodak Company, 1997). The camera shutter is very slow in comparison to the interval between the laser pulses used in this research. As a result, both images are captured during one opening of the camera shutter. The camera shutter is fully open when the illumination pulses are emitted. The first frame is captured by the light-sensitive cells during the first illumination pulse, and immediately transferred to the storage cells. The light-sensitive cells then capture the second frame during the second laser pulse without closing the camera shutter. The storage cells now contain the first frame and the light-sensitive cells have the second frame. These frames are then transferred to the processor for further analysis.

The time intervals between actions in the data acquisition process are very small and must be very accurately timed. The timing is controlled by the PIV processor, which has

a synchronization board that sends appropriate signals to the various pieces of equipment at the appropriate time.

## **7.5 Processing and Analysis**

The PIV processor is a dedicated vector processing unit. The flow images captured by the recording device are transferred to the processor for processing. The various processing options used in this research are data windowing, correlation plane evaluation, multiple peak detection and vector measurement, some of which are described hereafter.

### **7.5.1 Data Windowing**

Data windowing was used to improve the signal-to-noise ratio in the correlation plane. The image maps are cross-correlated using a fast Fourier transform (FFT) technique, which assumes that the input is cyclic in nature (Dantec, 1998). This causes the FFT to generate eight ghost interrogation regions around the region under interrogation, as shown in Figure 7.4. These ghost interrogation regions are exact copies of the area interrogated, and thus they contain the same particles as the region under interrogation. The real particles from frame one are thus correlated with both the real particles of frame two (residing in the actual interrogation region), as well as these ghost particles in frame two (residing in the ghost interrogation regions). This reduces the signal-to-noise ratio of the correlation plane.

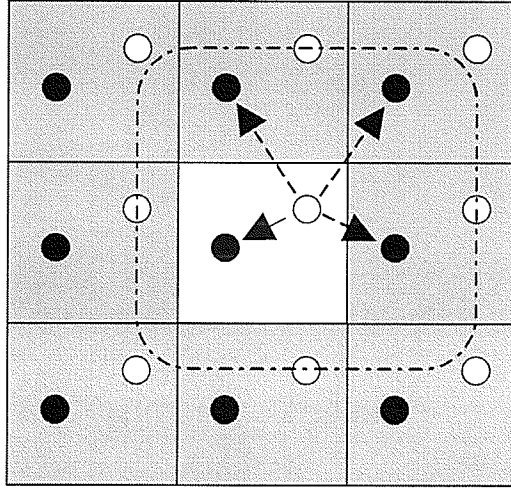


**Figure 7.4: Schematic of the ghost interrogation regions that are generated around the region under interrogation**

In Figure 7.4, the white square is the region under interrogation, whereas the gray squares are ghost interrogation regions. The filled circles represent particles in image 1 while the hollow circles represent particles in image 2. The solid arrow represents the correct correlation while the dotted arrows represent correlations with ghost particles.

The window functions multiply the camera image gray scale values by a weighting function having a value between 0 and 1. The Gaussian window function of Eq. (7.2) was applied to the image maps, with  $k = 1.0$ , i.e.,

$$G(i, j) = \exp \left[ - \left( \frac{2m}{kM} \right)^2 - \left( \frac{2n}{kN} \right)^2 \right] \quad (7.2)$$

where  $M$  and  $N$  are the number of pixels in the  $x$  and  $y$  directions, respectively, and  $m$  and  $n$  are the pixel positions in the  $x$  and  $y$  directions, respectively. The point  $(m, n) = (0, 0)$  is

located at the center of the image. Equation (7.2) is plotted in Figure 7.5. The weighting factor is close to one near the center, where real particles are likely to reside. It approaches zero near the edge of the interrogation region, where ghost particles are likely to reside.

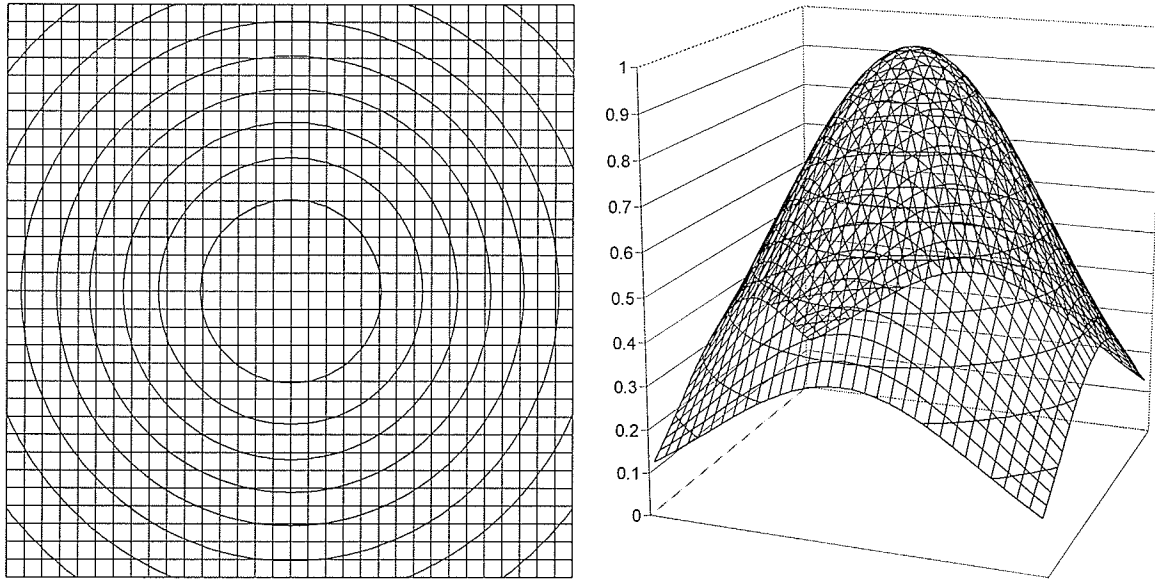
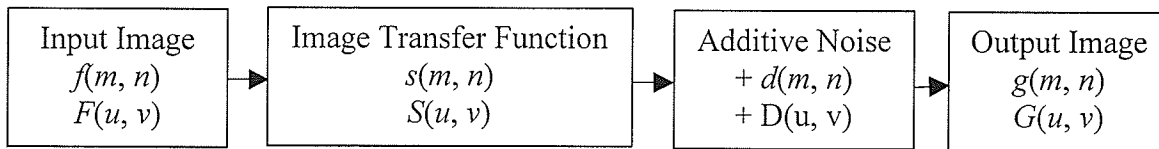


**Figure 7.5: Gaussian window function with  $k = 1.0$ ,  $M = 1016$  and  $N = 1008$**

An undesirable characteristic of window functions is that they reduce the weight of real particles near the edges of an interrogation region. It is thus recommended that the interrogation regions should be overlapped. For example, with a 50 % overlap, the edge of one interrogation region coincides with the center of one of the adjacent interrogation regions. An overlap of 50% was used in this research, with the image map divided into  $32 \times 32$  interrogation regions.

### 7.5.2 Correlation Plane Evaluation

The cross-correlation plane is evaluated using FFT processing of the image maps. The two image maps from the recording device are divided into smaller areas called interrogation regions. The particles that appear in a particular interrogation region from the first image are compared to those appearing in the corresponding interrogation region of the second image. The goal of cross-correlation is to determine the average shift in the position of the particles from the first frame to the next frame. This procedure can be shown as follows



The function  $f(m, n)$  represents the light intensity within the interrogation area in frame one, while the function  $g(m, n)$  represents the light intensity within the interrogation area in frame two (Dantec, 1998). The function  $g(m, n)$  is the output of the transfer function,  $s(m, n)$ , after signal noise,  $d(m, n)$ , is added. The upper case functions represent the Fourier Transforms of the corresponding lower case functions, where  $(u, v)$  are coordinates in the frequency plane of the Fourier Transforms. The noise function,  $d(m, n)$ , is a result of seeding particle moving into and out of the interrogation region. Determination of the function  $S(u, v)$  is the main goal of the cross-correlation. The best functional form of the displacement function,  $S(u, v)$ , is used to calculate the velocity vector for the interrogation region.

## 7.6 *The Water Tunnel*

As mentioned earlier, PIV experiments are more suited to water than to air. There are many more substances that are approximately neutrally buoyant in water than there are in air, making a water tunnel more attractive for flow visualization than a wind tunnel. Additionally, particles are automatically evenly distributed in the flow during water tunnel operation, whereas a seeding mechanism is required in a wind tunnel. The Water Tunnel 505 by Engineering Laboratory Designs, Inc., was used to generate a repeatable variable flow past the experimental bluff bodies and it is shown in Figure 7.6. The test section dimensions are 60.96 cm (wide)  $\times$  76.20 cm (high)  $\times$  182.88 cm (long) (Engineering Laboratory Designs, 2000). A 30 HP motor drives the propeller and it is capable of generating a flow rate of 0.362 m<sup>3</sup>/s, corresponding to a flow speed of 1.16 m/s in the test section (at maximum propeller frequency of 60 Hz). The tunnel was operated at maximum speed for all tests conducted in this research.

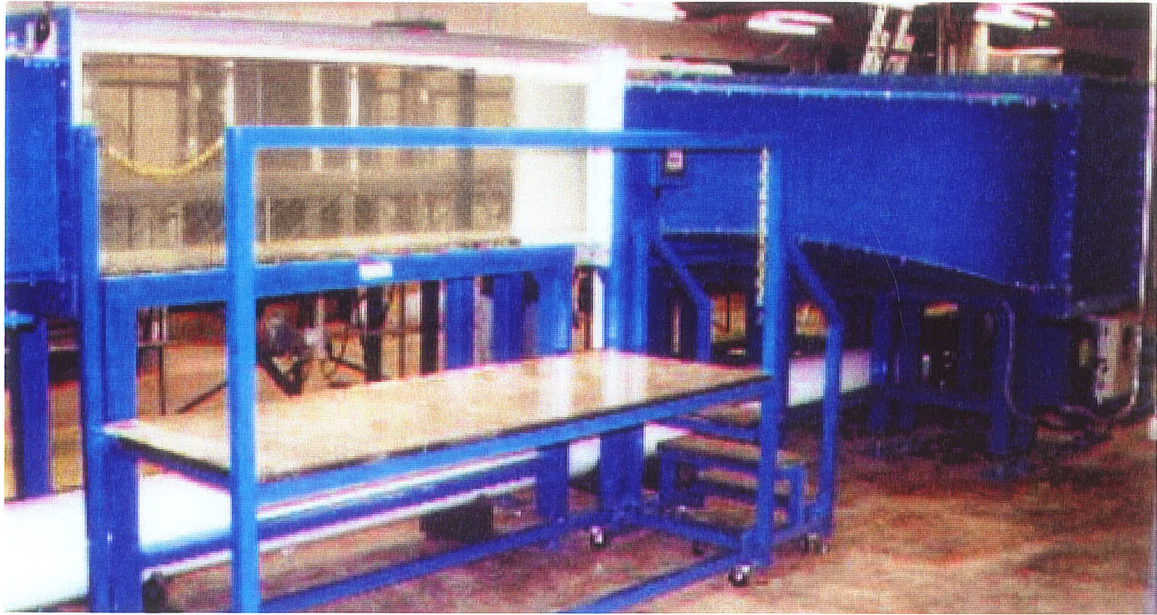


**Figure 7.6: Water Tunnel 505 by Engineering Lab Designs Inc.**

### **7.7 *The Bluff Bodies***

Two bluff bodies, resembling the EBCIs of Figure 7.1, but scaled down by 40%, were constructed. Blue construction Styrofoam was chosen as the building material because it is lighter, cheaper and easier to shape than wood, metal or plaster. The Styrofoam bluff bodies are extremely rigid when properly coated with a fiberglass woven roving and appropriate epoxy.

The blue Styrofoam was cut using a 48-inch hot-wire cutter. Wooden templates, taped to the sides of the foam block, were used to guide the wire. The templates were produced by enlarging the original inlet bay drawings from GKN Westland Helicopters Ltd., with extensions added to the bottoms of the templates at an angle of  $55^\circ$  (representing the

ductwork) based on drawings from GKN. After the templates were removed, the bodies were sanded with 60-grit and 240-grit sandpaper to ensure a smooth surface.

Fiberglass woven roving was wrapped around the bluff bodies and impregnated with West System Brand 105 Epoxy Resin and slow hardening West System Brand 206 Hardener (together they form an epoxy). Drying times were approximately 24 hours.

The mounting system for the bluff bodies needed to be able to withstand large forces created by the fast-moving water. The inside of the tunnel's test section is flat with no discontinuities, requiring that the bodies are mounted from above the test section. It was decided that 1/2-inch copper piping would be used as the building material for the mounting system. The portions of the mounting systems that run from the bodies to the top of the test section were constructed as a ladder rather than two straight pipes, to ensure that the two vertical pipes remain parallel. An arm of the mounting system is shown in Figure 7.7. T-joints were used at the top of the ladders to allow the two supports to be attached to wooden blocks at the top of the test section, as well as permitting two copper pipes to span the test section to keep the two supports pressed tightly against the tunnel walls. The upper portion of the mounting apparatus is shown in Figure 7.8. Four-inch C-clamps adequately immobilize the wooden blocks when the water tunnel runs at full speed. The greatest stresses on the bluff bodies were expected to exist at the point where the mounting system entered the bluff bodies. Strips of wood were inserted into slots cut into the sides of the foam bodies to prevent the foam bodies from deforming or the fiberglass from cracking. The strips were secured in the slots using Lepage Bulldog

Grip PL300 Foam Board adhesive caulking. The mounting systems were designed so that the distance between the bottom of the bluff body and the bottom of the test section was 11.5 cm.

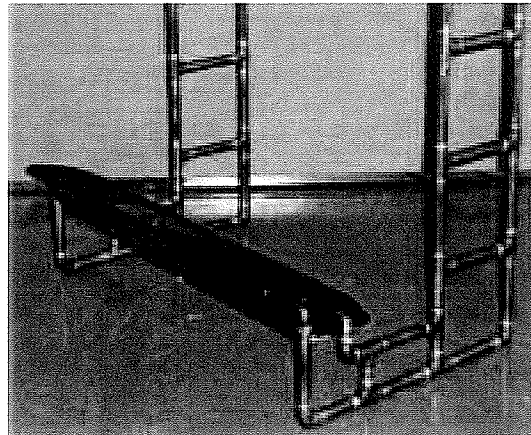


**Figure 7.7** Copper support used for mounting bluff bodies resembling EBCIs in the water tunnel

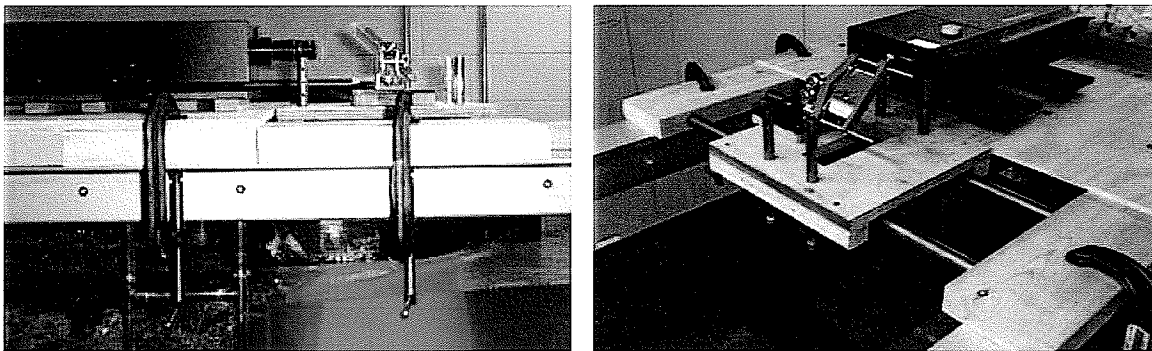


**Figure 7.8** Top of mounting system

Measurements revealed that the unpainted fiberglass reflected too much light. The laser sheet produced a bright glare along the edge of the body that disallowed the PIV system to detect particles near the surface. The bodies were thus coated with a layer of flat black rust paint and sanded with 240-grit sandpaper, significantly reducing reflections.

## 7.8 *Particle Image Velocimetry Experiments*

The PIV experiments should yield velocity fields that allow validation of numerical simulations. The main aspect that was examined in this research was the spreading rate of the turbulent wake. Numerical simulations of flows past bluff bodies resembling the EBCIs that predict significantly different spreading rates than those measured in the PIV experiments should be questioned.

The PIV Operators Manual suggests that a minimum of five seeding particles per interrogation region is required to achieve accurate velocity predictions. Experiments revealed that measurements performed with the minimum recommended seeding concentration yielded vector maps with several outliers. Seeding particles were added until the number of outliers approximately stabilized. This yielded a seeding concentration of approximately  $50 \text{ g/m}^3$ .

The cruising speed of the civil variant of the EH101 helicopter was chosen as representative of typical condition associated with the icing of EBCIs experienced by GKN. The cruising speed of the civil variant of the EH101 helicopter is approximately 150 knots (approximately 77 m/s) (GKN, 2000) Similar Reynolds numbers (based on air at 273 K and water at 293 K) would exist for a velocity of approximately 5.42 m/s in water (Oosthuizen, Naylor, 1999]. The 505 water tunnel generates a maximum speed of approximately 1.16 m/s. We thus performed the PIV experiments at maximum velocity.

Numerical simulations performed with a free-stream velocity of 1.16 m/s would be turbulent, and could thus still be useful for validating the CFD code.

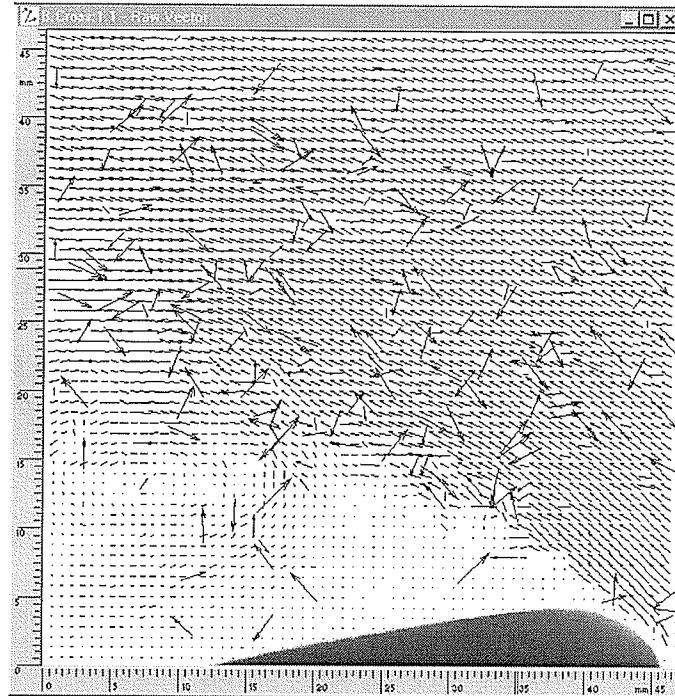
Experiments revealed that a 200  $\mu$ s delay between images yields optimum raw velocity maps when operating the tunnel at maximum speed. Particles travel (at most) one quarter of an interrogation region (based on  $32 \times 32$  interrogation regions) in this length of time. Cross correlations were derived from the image maps using  $32 \times 32$ -pixel interrogation regions with 50 percent overlap and a Gaussian window function.

There are an incredible number of processing combinations that could be performed on the raw vector maps. Several combinations were tested. It was found that any combination involving filtering produced the smoothest vector maps, but these were likely accompanied by a loss of information caused by the smoothing effect of the filtering algorithms. It was thus decided that filtering would not be employed. The post-processing of raw vector maps used in this research consisted of:

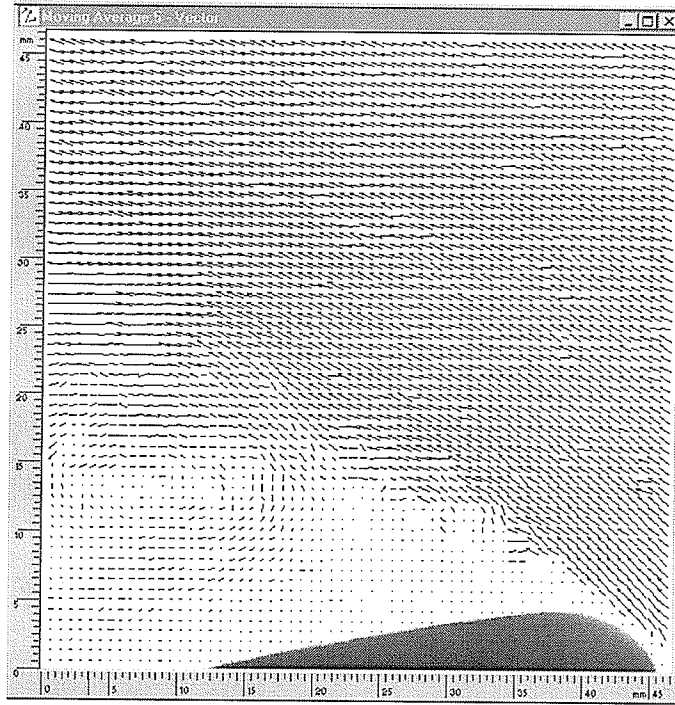
- a moving average algorithm to adjust any outliers, and
- statistical averaging of all measurements.

Figure 7.9 shows one of thirty raw vector maps that were measured for flow past the bluff body resembling EBCI No.2. Clearly there are several velocity vectors that are in significant error. This is likely a result of insufficient seeding densities in the corresponding interrogation regions, resulting in a poor correlation. A moving average

algorithm was applied to each of the raw vector maps. Figure 7.10 shows the validated vector map corresponding to the raw vector map of Figure 7.9.



**Figure 7.9: Raw vector map for the flow past the bluff body resembling engine bay cooling inlet No.2**



**Figure 7.10: Validated (moving average algorithm) vector map for the flow past the bluff body resembling engine bay cooling inlet No.2**

A statistical average was derived from the thirty validated vector maps, resulting in the averaged vector map of Figure 7.11. Every vector from all thirty validated vector maps was used in the averaging procedure. It is felt that thirty readings were enough to achieve an average vector map that is representative of the transient flow. Figure 7.11 shows a clear separation of the boundary layer past the leading edge of the EBCI. The reattachment point would be far downstream of the EBCI.

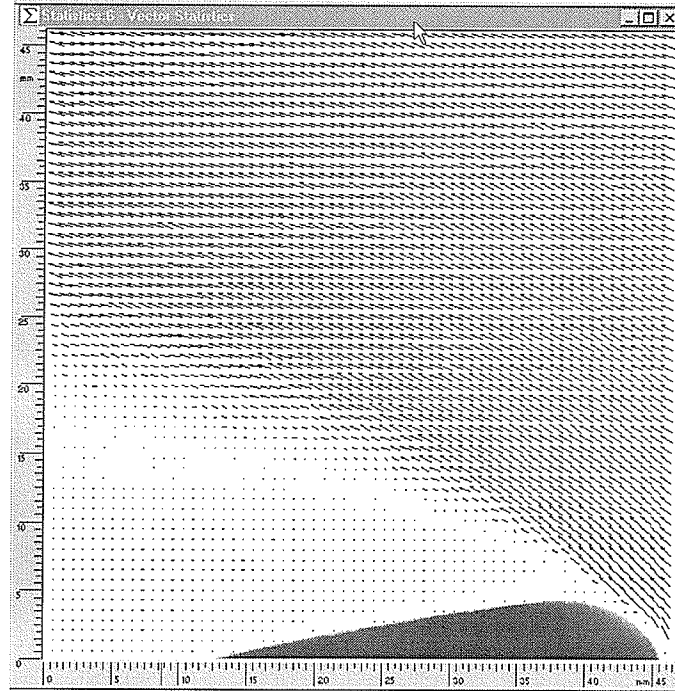


**Figure 7.11: Statistically averaged vector map (average of 30 validated vector maps) for the flow past the bluff body resembling engine bay cooling inlet No.2**

The streamline and vorticity plots of Figure 7.12 and 7.13 were generated from the averaged vector map of Figure 7.11. Figure 7.12 shows a recirculation cell on the back side of the EBCI. Altering the geometry of the EBCI, such as embedding micromachined grooves, could change the location of the separation point and affect the flow structure of the downstream recirculation cell. It is anticipated that the effects of altering the EBCI shape can be possible using the CFD code discussed in this thesis. For example, embedded surface grooves could affect the airstream in ejecting runback water from the helicopter surface, before it refreezes. In this way, the surface shapes could be re-designed to become less ice prone.

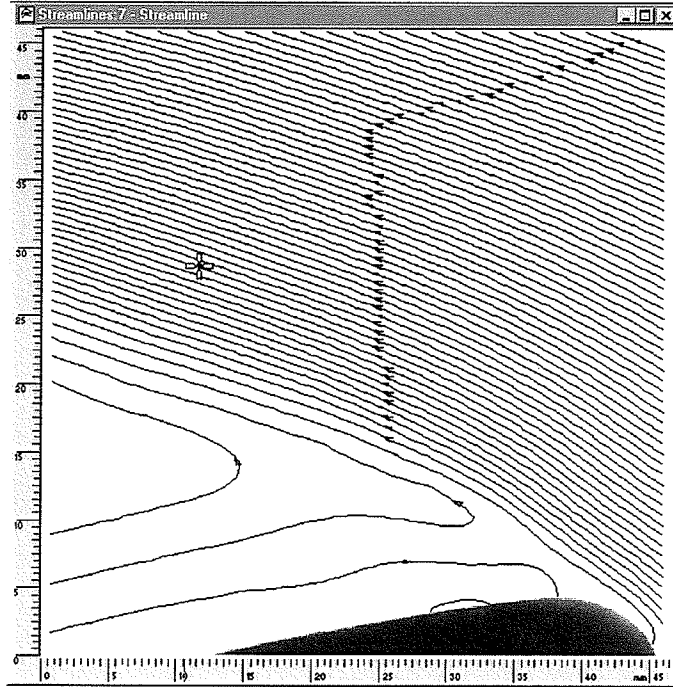


**Figure 7.12: Streamline plot for the flow past the bluff body resembling engine bay cooling inlet No.2**

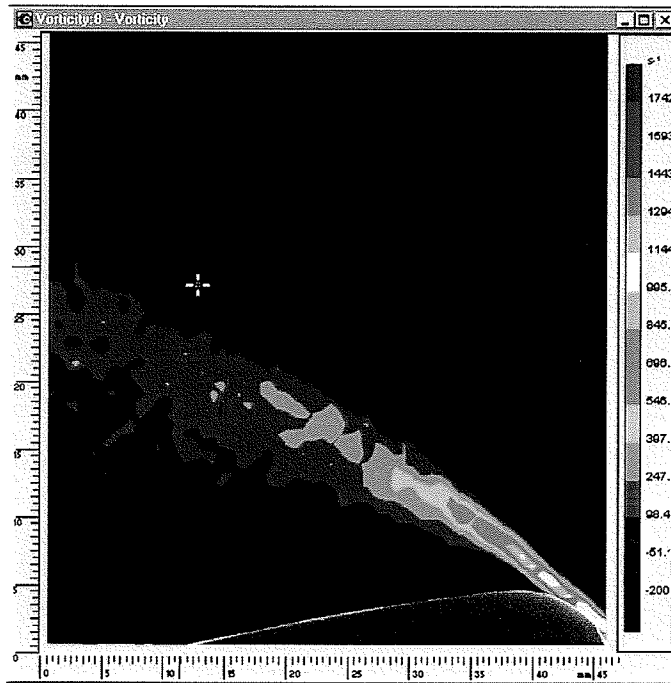


**Figure 7.13: Vorticity plot for the flow past the bluff body resembling engine bay cooling inlet No.2**

The spreading rate of the turbulent wake is the main parameter of these PIV experiments. The spreading rate for bluff body No.2, denoted by  $\alpha_2$ , was determined from the streamline plot of Figure 7.12. Two points were used to determine the spreading rate of the wake. The first point was the location of the separation point, having coordinates  $(x_1, y_1) = (45.63, 1.02)$  mm. The second was the downstream end of the streamline emanating from the separation point with coordinates  $(x_2, y_2) = (0.0, 23.42)$  mm. These two coordinates yield a spreading rate of  $\alpha_2 = 26.2^\circ$ .

An experimental uncertainty analysis was performed based on standard techniques outlined in the ASME Journal of Heat Transfer (ASME International, 2001). The spreading rate of the wake,  $\alpha$ , was calculated as

$$\alpha = \tan^{-1} \left( \frac{y_2 - y_1}{x_2 - x_1} \right) \quad (7.3)$$

The uncertainty,  $U$ , in the spreading rate may be determined from

$$U = \sqrt{B^2 + P^2} \quad (7.4)$$

where  $B$  and  $P$  are the precision limit and bias limit, respectively. The magnitudes of  $B$  and  $P$  may be determined separately in terms of the sensitivity coefficients of  $\alpha$  to the coordinate values used in Eq. (7.3) following the propagation equation of Kline and McClintock (1953) as

$$B^2 = \left(\frac{\partial\alpha}{\partial x_1}\right)^2 B_{x_1}^2 + \left(\frac{\partial\alpha}{\partial x_2}\right)^2 B_{x_2}^2 + \left(\frac{\partial\alpha}{\partial y_1}\right)^2 B_{y_1}^2 + \left(\frac{\partial\alpha}{\partial y_2}\right)^2 B_{y_2}^2 \quad (7.5)$$

$$P^2 = \left(\frac{\partial\alpha}{\partial x_1}\right)^2 P_{x_1}^2 + \left(\frac{\partial\alpha}{\partial x_2}\right)^2 P_{x_2}^2 + \left(\frac{\partial\alpha}{\partial y_1}\right)^2 P_{y_1}^2 + \left(\frac{\partial\alpha}{\partial y_2}\right)^2 P_{y_2}^2 \quad (7.6)$$

The partial derivatives found in the above equations were determined to be

$$\frac{\partial\alpha}{\partial x_1} = \frac{y_1 - y_2}{(x_1 - x_2)^2 + (y_1 - y_2)^2} \quad (7.7)$$

$$\frac{\partial\alpha}{\partial x_2} = \frac{y_2 - y_1}{(x_1 - x_2)^2 + (y_1 - y_2)^2} = -\frac{\partial\alpha}{\partial x_1} \quad (7.8)$$

$$\frac{\partial\alpha}{\partial y_1} = \frac{-1}{(x_1 - x_2)^2 + \frac{(y_2 - y_1)^2}{x_1 - x_2}} \quad (7.9)$$

$$\frac{\partial\alpha}{\partial y_2} = \frac{1}{(x_1 - x_2)^2 + \frac{(y_2 - y_1)^2}{x_1 - x_2}} = -\frac{\partial\alpha}{\partial y_1} \quad (7.10)$$

Firstly, we consider the determination of the precision limits. The precision limits account for the unsteadiness of the flow and represent the band about the average value within which results should fall if the experiment were repeated many times under the same conditions. In this experiment, vortices are periodically shed from the bluff bodies, thereby causing unsteadiness of the wake. When determining the unsteadiness in the coordinates  $x_1$ ,  $x_2$ ,  $y_1$  and  $y_2$ , we need to consider only their relative magnitudes because

the scaling factor would affect all of the independent variables of Eqs. (7.5) and (7.6) by the same amount.

Streamline plots were generated from each of the thirty validated vector maps. The determination of the observed location of the separation points from the streamline plots involves some uncertainty. This is because the regions occupied by the bluff body and the shadow cast by the bluff body contain no particles. The PIV software predicts erroneous vectors in this region, which cannot be removed using moving average algorithms. The location of the separation point was assumed constant and approximated from the streamline plot of Figure 7.12. The precision limits of  $x_1$  and  $y_1$  were conservatively estimated to be 3 mm. The precision limit of  $x_2$  was not considered because  $x_2$  is always located at 0 mm. The precision limit of  $y_2$  was determined by examining all of the streamline plots to determine the range of measured  $y_2$  values. The value of  $y_2$  varied between 20.5 and 27.5 mm. The precision limit was assumed to be half of the total range, equal to 3.5 mm.

The bias limit is an estimate of the fixed constant error (ASME International, 2001). In this experiment, the fixed error should not affect the value of  $\alpha$  because all of the coordinates would be equally affected by the bias error.

Following this procedure, the spreading rate was determined to be  $\alpha_2 = 26.2^\circ \pm 1.6^\circ$ . This represents a measurement accuracy within about  $\pm 6.1\%$ .

Figures 7.14 and 7.15 show the streamline and vorticity plots for the flow past the bluff body resembling EBCI No.1 and No.3. A procedure similar to that described above was performed for flow past these bluff bodies, yielding a spreading rate of  $\alpha_{1,3} = 18.2^\circ$   
 $1.2^\circ$ .

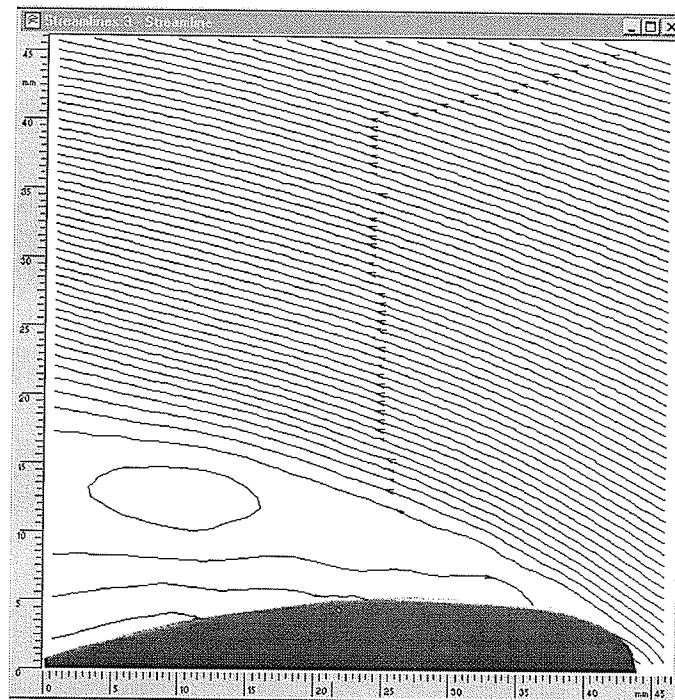


**Figure 7.14: Streamline plot for the flow past the bluff body resembling engine bay cooling inlets No.1 and No.3**

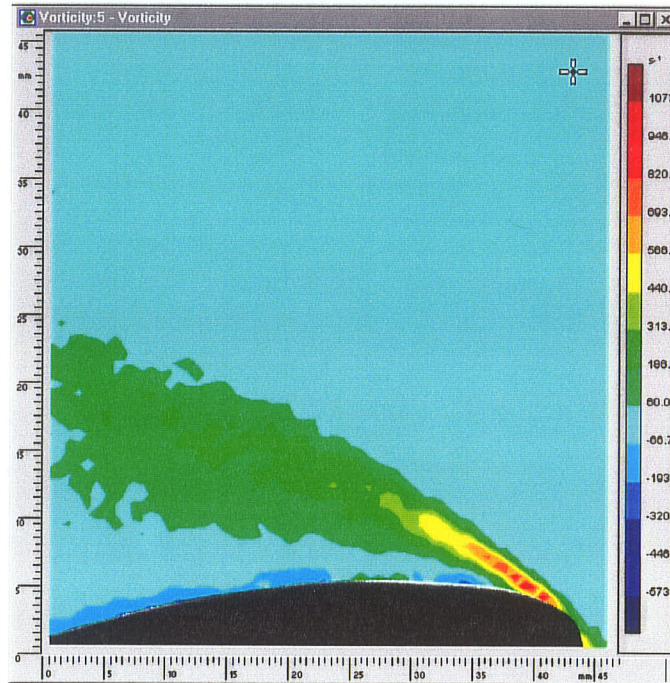


**Figure 7. 15: Vorticity plot for the flow past the bluff body resembling engine bay cooling inlets No.1 and No.3**

The spreading rate of the turbulent wake is now known for flow past two bluff bodies resembling engine bay cooling inlets. A, important characteristic parameter is now known that can be used to verify numerical simulations of flows past bodies resembling EBCIs.

# Chapter 8: Closure

## 8.1 *Conclusions*

A two-equation  $k$ - $\varepsilon$  turbulence model was developed within an existing multiphase computational fluid dynamics (CFD) code to allow the prediction of ice accretion on helicopter engine bay cooling inlets (EBCIs). This turbulence model serves as a base from which multiphase extensions, involving droplet turbulence, may be made. These extensions would likely involve adding damping and other source terms to the turbulence equations. A control-volume-based finite-element method (CVFEM) was employed to solve the turbulence conservation equations.

The  $k$ - $\varepsilon$  turbulence model developed in this thesis was presented. A two-equation turbulence model was selected for many reasons. Two-equation turbulence models appear to be well suited to solving flows involving complex geometries. Also, they are complete, meaning that no prior knowledge of the flow is required. A  $k$ - $\varepsilon$  turbulence model with wall functions was selected for this application. Other two-equation turbulence models require significant grid refinement in the near-wall region. This causes difficulties in multiphase flows because the ice that accretes on the walls of the domain creates the need for undesired re-meshing.

Wall functions were employed in the near-wall region. These wall functions prescribe the velocity profile in the near-wall region. This eliminates the need to refine the grid along the walls in order to capture the steep velocity gradients using the momentum equations. Special wall functions, based on Reichardt's law, were developed to span the entire near-wall region. A new prescription for  $\varepsilon$  at the first interior node was developed that is consistent with Reichardt's law.

Intermediate solutions of turbulence equations that contain negative values could have disastrous effects on the turbulence model. A positivity scheme was thus developed that is based on physical principles and should never require "clipping". This requires that the positivity scheme is implemented on a local element-by-element basis. Entries in the local stiffness matrices that have undesirable signs are incorporated into the diagonal entries or the solution vectors. An advection positivity scheme was developed to eliminate the possibility of negative results due to advection terms. A hybrid positivity scheme was developed to eliminate the possibility of negative values due to both advection and diffusion terms. An absolute positivity scheme was developed to guarantee positive values to ensure that clipping would never be required.

A channel flow was simulated to determine whether the turbulence model had been correctly formulated and implemented into the existing CFD code. The channel flow resembles the ductwork leading into a helicopter engine bay and it provides inlet boundary conditions for a backward-facing step simulation. Overall, the model seems to be predicting reasonable trends of the turbulence quantities. To further assess the model's

ability to predict channel flows, velocity profiles from various simulations were imposed throughout the domain and the turbulence quantities were solved. The results indicated that the model had been correctly formulated and that the velocity profile across the channel has a dramatic effect on the solution of the turbulence quantities. A grid refinement study was performed and the agreement of the turbulence quantities showed further improvement.

Flow over a backward-facing step was simulated because it resembles another relevant aspect of the flow past the engine bay cooling inlets. A channel flow simulation provided the inlet conditions for this flow. The backward-facing step simulation predicted a reattachment length of 5.35 step heights, an approximate 25% underprediction. Earlier reported results indicate that the  $k-\varepsilon$  model under-predicts the reattachment length by 20-25 %. This simulation further suggests that the turbulence model has been correctly formulated and implemented in the existing CFD code.

Particle image velocimetry (PIV) measurements were performed of flow past bluff bodies resembling 40% scaled models of helicopter engine bay cooling inlets (EBCIs). Thirty measurements were performed for each of the two bluff bodies. A moving average algorithm was employed to validate the raw vector maps. A statistical average was applied to the thirty validated vector maps for each of the bluff bodies. From these averaged vector maps, streamline and vorticity plots were generated. The spreading rates of the turbulent wakes were determined to be about  $\alpha_2 = 26.2^\circ$  and  $\alpha_{1,3} = 18.2^\circ$  for the bluff bodies resembling EBCI No.2 and EBCIs No.1 and No.3, respectively. These

spreading rates are anticipated to be useful for validating future numerical simulations of flow past the bluff bodies.

## **8.2 *Recommendations for Future Research***

Simulations of the channel flow revealed an issue relating to the coupling of the momentum and turbulence subroutines. Initially, the channel flow simulation was performed with the velocity field predicted from the momentum equations of the CFD solver. This simulation revealed an artificial mass generation between the channel inlet and the channel outlet. The resulting over-prediction of the velocity field led to over-predictions of production of  $k$  across the entire channel, especially in the near-wall region. It is felt that differences in the treatment of influence coefficients with PINS may be affecting the calculation of advecting and linearized advected velocities in the momentum equations. Full integration of the turbulence model into the multiphase flow solver remains to be completed.

The PIV measurements performed in this thesis provide the spreading rate of the turbulent wake. It is anticipated that this important characteristic parameter can be used to validate numerical simulations of flows past bluff bodies resembling helicopter engine bay cooling inlets (EBCIs). Simulations of flow past EBCIs will be performed with and without droplets in the airstream.

As mentioned in this thesis, the  $k-\varepsilon$  turbulence model that developed serves as a based for which extensions to multiphase flows may be made. PIV experiments in the water tunnel and in a new spray tunnel will be performed in an attempt to better understand the behavior of droplets after they enter the boundary layer along a solid surface. Additional source and damping terms may be added to the turbulence equations to account for the turbulence of the droplets.

# References

Amano, R.S., “Development of a Turbulence Near-Wall Model and its Application to Separated and Reattached Flows”, Numerical Heat Transfer, vol. 7, pp. 59-75, 1984.

ASME International, Policy on Reporting Uncertainties in Experimental Measurements and Results, Journal of Heat Transfer, ASME International, [http://www.seas.ucla.edu/jht/info/files/policy\\_uncertainty.pdf](http://www.seas.ucla.edu/jht/info/files/policy_uncertainty.pdf), Nov 2001.

Buchhave, P., “Particle Image Velocimetry – Status and Trends”, Experimental Thermal and Fluid Science, pp. 586-604, 1992.

Baldwin, B., Lomax, H., “Thin-Layer Approximation and Algebraic Model for Separated Turbulent Flows”, AIAA Paper 78-257, AIAA 16<sup>th</sup> Aerospace Sciences Meeting, Huntsville, Alabama, January 1978.

Cazalbou, J. B., Spalart, P. R., Bradshaw, P., “On the Behavior of Two-Equation Models at the Edge of a Turbulent Region”, Physics of Fluids, vol. 6, no. 5, pp. 1797-1804, 1994.

Chai, J. C., Amano, R. S., "Application of a Higher-Order Turbulence Closure Model to a Plane Jet", Numerical Heat Transfer, Part A, vol. 21, pp. 21-35, 1992.

Chen, H. C., Patel, V. C., "Near-Wall Turbulence Models for Complex Flows Including Separation", AIAA Journal, vol. 26, no. 6, pp. 641-648, 1988.

Danov, S. N., Arai, N., Churchill, S. W., "Exact Formulations and Nearly Exact Numerical Solutions for Convection in Turbulent Flow Between Parallel Plates", International Journal of Heat and Mass Transfer, v. 43, pp. 2767-2777, 2000.

Dantec Measurement Technology, FlowMap Installation and User's guide: 4<sup>th</sup> edition, Skovlunde, Denmark, 1998.

Dash, S. M., Beddini, R. A., Wolf, D. E., Sinha, N., "Viscous/Inviscid Analysis of Curved Sub- or Supersonic Wall Jets", AIAA Paper 83-16709, 1983.

Durst, F., Schmitt, F., "Experimental Studies of High Reynolds Number Backward-Facing Step Flows, Cornell University, Ithica, New York, pp. 5.19-5.24, 1985.

Eastman Kodak Company, Kodak Megaplug Camera: User's Manual, Rochester, New York, 1997.

Eaton, J. K., Johnson, J. P., "Turbulent Flow Reattachment: An Experimental Study of the Flow and Structure Behind a Backward-Facing Step", Report MD-39, Stanford University, Stanford, California, 1980.

EH Industries, "EH Industries EH101 Medium-Lift Twin-Engine Helicopter",  
<http://www.aerospace-technology.com/projects/EH101>, July 2002.

EH101, "EH101 Completes Tour of Nordic Region",  
<http://defence-data.com/paris99/gknnew04.htm>, June 12, 1999.

Engineering Laboratory Design, Inc., 24" Flow Visualization Water tunnel Operation and Maintenance Manual, Lake City, Minnesota, 2000.

Etheridge, D. W., Kemp, P. H., "Measurements of Turbulent Flow Downstream of a Rearward-Facing Step", Journal of Fluid Mechanics, vol. 86, pp. 545-566, 1978.

Fluent, Tutorial Manual: 7. Modeling Turbulent Flows, Fluent Incorporated,  
<http://fortuitous.ncsa.uiuc.edu/fidapdocumentation/tutorial/tu07.htm>, National Center for Supercomputing Applications, University of Illinois at Urbana, 2000a.

Fluent, Theory Manual: 10. Turbulence Modeling, Fluent Incorporated,  
<http://fortuitous.ncsa.uiuc.edu/fidapdocumentation/theory/thtoc.htm#th10.htm>, National Center for Supercomputing Applications, University of Illinois at Urbana, 2000b.

GKN, EH101 Civil Variant, <http://www.gkn-whl.co.uk/ehcspec.html>, December 2000.

GKN, EH101 Cormorant, Press Release 11-07-1996, <http://www.gkn-whl.co.uk>, May 2002.

Goldberg, U., Peroomian, O., Chakravarthy, S., "A Wall-Distance-Free  $k-\varepsilon$  Model With Enhanced Near-Wall Treatment", ASME Journal of Fluids Engineering, vol. 120, pp. 457-462, 1998.

Hackman, L. P., Strong, A. B., Raithby, G. D., "The Calculation of Properties of the Flow over a Backward-Facing Step with a  $k-\varepsilon$  Model of Turbulence", Transactions of the CSME, vol. 8, no. 3, pp. 165-170, 1984.

Hirata, T., Matsui, H., "Ice Formation and Heat Transfer With Water Flow Around Isothermally Cooled Cylinders Arranged in a Line", ASME Journal of Heat Transfer, vol. 112, pp. 707-713, 1990.

Ilegbusi, J. O., Spalding, D. B., "An Improved Version of the  $k-\omega$  Model of Turbulence", ASME Journal of Heat Transfer, vol. 107, pp. 63-69, 1985.

Johnson, D. A., King, L. S., "A Mathematically Simple Turbulence Closure Model for Attached and Separated Turbulent Boundary Layers", AIAA Journal, vol. 23, no. 11, 1985.

Jones, W. P., Launder, B. E., "The prediction of Laminarization with a Two-Equation Model of Turbulence", *International Journal of Heat and Mass Transfer*, vol. 15, pp. 301-314, 1972.

Karimian, S. M. H., Schneider, G. E., "Pressure-Based Computational Method for Compressible and Incompressible Flows", *AIAA Journal of Thermophysics and Heat Transfer*, vol. 8, no. 2, pp. 267-274, 1994.

Kim, J., Kline, S. J., Johnson, J. P., "Investigation of a Reattaching Turbulent Shear Layer: Flow Over a Backward-Facing Step", *Journal of Fluid Mechanics*, vol. 102, no. 3, pp. 302-308, 1980.

Kim, J., Moin, P., Moser, R., "Turbulence Statistics in Fully Developed Channel Flow at Low Reynolds Number", *Journal of Fluid Mechanics*, v. 177, pp. 133-166, 1987.

Kim, J., Moin, P., "Transport of Passive Scalars in a Turbulent Channel Flow, Turbulent Shear Flows 6: Selected Papers from the Sixth International Symposium on Turbulent Shear flows", Berlin; New York: Springer-Verlag, 1989.

Kim, S. -W., Chen, Y. -S., "A Finite-Element Computation of Turbulent Boundary Layer Flows with an Algebraic Stress Turbulence Model", *Computer Methods in Applied Mechanics and Engineering*, vol. 66, pp. 45-63, 1988.

Kline, S. J., McClintock, F. A., "Describing Uncertainties in Single-Sample Experiments", Mechanical Engineering, vol. 104, pp. 250-260, 1953.

Kok, J. C., "Resolving the Dependence on Free-Stream Values for the  $k$ -Omega Turbulence Model", NLR-TP-99295, Nationaal Lucht- en Ruimtevaartlaboratorium (National Aerospace Laboratory NLR), 1999.

Lam, S. H., "On the RNG theory of turbulence", Physics of Fluids A, vol. 4, no. 5, pp. 1007-1017, 1992.

Launder, B. E., Spalding, D. B. "The Numerical Computation of Turbulent Flows", Computer Methods in Applied Mechanics and Engineering, vol. 3, pp. 269-289, 1974.

Launder, B. E., Sharma, B. I., "Application of the Energy Dissipation Model of Turbulence to the Calculation of Flow Near a Spinning Disc", Letters in Heat and Mass Transfer, vol. 1, no. 2, pp. 131-138, 1974.

Launder, B. E., "Numerical Computation of Convective Heat Transfer in Complex Turbulent Flows: Time to Abandon Wall Functions?", International Journal of Heat and Mass Transfer, vol. 27, no. 9, pp. 1485-1491, 1984.

Liu, F., Zheng, X., "Staggered Upwind Method for Solving Navier-Stokes and  $k$ - $\omega$  Turbulence Model Equations", AIAA Journal, vol. 33, no. 6, pp. 991-998, 1995.

Liu, F., Zheng, X., "Staggered Finite Volume Scheme for Solving Cascade Flow with a  $k-\omega$  Turbulence Model", AIAA Journal, vol. 32, no. 8, pp. 1589-1596, 1994.

Liu, F., Jameson, A., "Multigrid Navier-Stokes Calculations for Three-Dimensional Cascades", AIAA Journal, vol. 31, no. 10, pp. 1785-1791, 1993.

Lu, M. L., Popplewell, N., Shah, A. H., Barrett, W., Au, A., "Mass of Ice Accretion from Freezing Rain Simulations", Proceedings of 8<sup>th</sup> IWAIS, Iceland, 1998.

Mansour, N. N., Kim, J., Moin, P., "Reynolds-Stress and Dissipation-Rate Budgets in a Turbulent Channel Flow", Journal of Fluid Mechanics, v. 194, pp. 15-44, 1988.

Menter, F. R., "Influence of Freestream Values on  $k-\omega$  Turbulence Predictions", AIAA ASME Journal, vol. 30, no. 6: Technical Notes, pp. 1657-1659, 1992a.

Menter, F. R., "Performance of Popular Turbulence Models for Attached and Separated Adverse Pressure Gradient Flows", AIAA Journal, vol. 30, no. 8, pp. 2066-2072, 1992b.

Menter, F. R., "Two-Equation Eddy-Viscosity Turbulence Models for Engineering Applications", AIAA Journal, vol. 32, no. 8, pp. 1598-1605, 1994.

Menter, F. R., "A Comparison of Some Recent Eddy-Viscosity Turbulence Models", Journal of Fluids Engineering, vol. 118, pp. 514-519, 1996.

Menter, F. R., "Eddy Viscosity Transport Equations and their Relation to the  $k-\epsilon$  Model", Transactions of the ASME, vol. 119, pp. 876-883, 1997.

Minkowycz, W. J., Sparrow, E. M., Schneider, G. E., Pletcher, R. H., Handbook of Numerical Heat Transfer, John Wiley & Sons, Inc., New York, 1988.

Moin, P., Kim, J., "Numerical Investigation of Turbulent Channel Flow", Journal of Fluid Mechanics, vol. 118, pp. 341-377, 1982.

Myers, K. J., Ward, R. W., Bakker, A., "A Digital Particle Image Velocimetry Investigation of Flow Field Instabilities of Axial-Flow Impellers", ASME Journal of Fluids Engineering, vol. 119, pp. 623-632, 1997.

Myers, T. G., Thompson, C. P., "Modeling the Flow of Water on Aircraft in Icing Conditions", AIAA Journal, vol. 36, no. 6, pp. 1010-1013, 1998.

Naterer, G. F., "On Turbulent Boundary Layer Flow Near an Accreting Ice Surface", Report, Department of Mechanical Engineering, University of Waterloo, Waterloo, Ontario.

Naterer, G. F., Schneider, G. E., "PHASES Model of Binary Constituent Solid – Liquid Phase Transition – Part 1. Numerical Method", Numerical Heat Transfer B, vol. 28, no. 2, pp. 111-126, 1995a.

Naterer, G. F., Schneider, G. E., "PHASES Model of Binary Constituent Solid – Liquid Phase Transition – Part 2. Applications", Numerical Heat Transfer B, vol. 28, no. 2, pp. 127-137, 1995b.

Naterer, G. F., "Simultaneous Pressure-Velocity Coupling in the Two-Phase Zone for Solidification Shrinkage in an open Cavity", Modeling Simulations of Material Sciences and Engineering, vol. 5, pp. 595-613, 1997.

Naterer, G. F., "Constructing an Entropy-Stable Upwind Scheme for Compressible Fluid Flow Computations", AIAA Journal, vol. 37, no. 3, pp. 303-312, 1999.

Naterer, G. F., Deng, H., Popplewell, N., "Predicting and Reducing Glaze Ice Accretion on Electrical Power Lines with Joule Heating: Theory and Experiments", Transactions of the CSME, vol. 23, no. 1A, pp. 51-70, 1999.

Naterer, G. F., Glockner, P. S., personal communications to G. Richardson, GKN Westland Helicopters Ltd., UK, 2000-2002.

Naterer, G. F., Popplewell, N., Deng, H., Shah, A. H., "Prediction and Measurement of Ice and Wind Loads on Power Lined During a Freezing Rainstorm", Final Report to Manitoba Hydro, Canada, 2000.

Naterer, G. F., and Glockner, P. S., "Pulsed Laser PIV Measurements and Multiphase Turbulence Model of Aircraft Engine Inlet Flows", AIAA Paper 2001-3032, 31st AIAA Fluid Dynamics Conference, Anaheim, CA, June 11-14, 2001.

Naterer, G. F., "Multiphase Flow with Impinging Droplets and Airstream interaction at a Moving Gas/Solid Interface", International Journal of Multiphase Flow, v. 28, pp. 451-477, 2002.

[NWV] Near-Wall Velocity, <http://www.me.mtn.edu/~slyang/meem5240/wallfn.pdf>, 2001.

New Wave Research Co., Ltd., Operator's Manual: Tempest and Gemini PIV Nd: Yag Lasers, Cambridgeshire, England, 2000.

Oosthuizen, P. H., Naylor, D., Introduction to Convective Heat Transfer Analysis, WCB/McGraw-Hill, New York, 1999.

Pajayakrit, P., Kind, R. J., "Assessment and Modification of Two-Equations Turbulence Models", AIAA Journal, vol. 38, no. 6, pp. 955-963, 2000.

Papageorgakis, G. C., Assanis, D. N., "Comparison of Linear and Nonlinear RNG-Based  $k$ - $\varepsilon$  Models for Incompressible Turbulent Flows", Numerical Heat transfer, Part B, vol. 35, no. 1-22, 1999.

Patel, C. P., Rodi, W., Scheuerer, G., "Turbulence Models for Near-Wall and Low-Reynolds Number Flows: A Review", AIAA Journal, vol. 23, no. 9, pp. 1308-1319, 1984.

Peng, S. -H. Davidson, L., "New Two-Equation Eddy Viscosity Transport Model for Turbulent Flow Computations", AIAA Journal, vol. 38, no. 7, pp. 1196-1205, 2000.

Rodi, W., Scheuerer, G., "Scrutinizing the  $k-\varepsilon$  Turbulence Model Under Adverse Pressure Gradient Conditions", Transactions of the ASME, vol. 108, pp. 174-179, 1986.

Schetz, J. A., Foundations of Boundary Layer Theory for Momentum, Heat, and Mass Transfer, Prentice-Hall, Inc. 1984.

Schneider, G. E., Zedan, M., "Control Volume Based Finite Element Formulation of the Heat Conduction Equation", AIAA Paper 82-0909, AIAA/ASME 3<sup>rd</sup> Joint Thermophysics, Fluids, Plasma and Heat transfer Conference, St. Louis, Missouri, June 7-11, 1982.

Schneider, G. E., Raw, M. J., "A Skewed, Positive Influence Coefficient Upwinding Procedure for Control-Volume-Based Finite-Element Convection-Diffusion Computation", Numerical Heat Transfer, vol. 9, pp. 1-26, 1986.

Schuster, E. P., Gambill, J. M., Fisher, M. S., "Computational Icing Analysis of Aircraft Inlets", AIAA Paper 92-3178, 1992.

Smith, L. M., Reynolds, W. C., "On the Yakhot-Orszag Renormalization Group Method for Deriving Turbulence Statistics and Models", Physics of Fluids A, vol. 4, no. 2, pp. 364-371, 1992.

Speziale, C. G., Gatski, T. B., Fitmaurice, N., "An Analysis of RNG-Based Turbulence Models for Homogeneous Shear Flow", Physics of Fluids A, vol. 3, no. 9, pp. 2278-2281, 1991.

Speziale, C. G., Abid, R., Anderson, E. C., "Critical Evaluation of Two-Equation Models for Near-Wall Turbulence", AIAA Journal, vol. 30, no. 2, pp. 324-331, 1992.

Speziale, C. G., Thangam, S., "Analysis of an RNG Based Turbulence Model for Separated Flows", International Journal for Engineering and Science, vol. 30, no. 10, pp. 1379-1399, 1992.

Tascflow, <http://www.cranfield.ac.uk/cww/ccc/documentation/tascflow/theory>,  
Bedfordshire, UK, 2000.

Teitel, M., Antonia, R. A., "Heat Transfer in Fully Developed Turbulent Channel Flow: Comparison Between Experimental and Direct Numerical Simulations", International Journal of Heat and Mass Transfer, v. 36, no. 6, pp. 1701-1706, 1993.

Thangam, S., Hur, N., "A Highly-Resolved Numerical Study of Turbulent Separated Flow Past a Backward-Facing Step", International Journal of Engineering Science, vol. 29, no. 5, pp. 607-615, 1991.

Thangam, S., Speziale, C. G., "Turbulent Flow Past a Backward-Facing Step: A Critical Evaluation of Two-Equation Models", AIAA Journal, vol.30, no. 5, pp. 1314-1320, 1992.

White, F., Viscous Fluid Flow, McGraw-Hill, 1974.

Wilcox, D. C., "Reassessment of the Scale-Determining Equation for Advanced Turbulence Models", AIAA Journal, vol. 26, no. 11, pp. 1299-1310, 1988a.

Wilcox, D. C., "Multiscale Model for Turbulent Flows", AIAA Journal, vol. 26, no. 11, pp. 1311-1320, 1988b.

Wilcox, D. C., "Comparison of Two-Equation Turbulence Models for Boundary Layers with Pressure Gradient", AIAA Journal, vol. 31, no. 8, pp. 1414-1421, 1993.

Wilcox, D. C., "Simulation of Transition with a Two-Equation Turbulence Model",  
AIAA Journal, vol. 32, no. 2, pp. 247-255, 1994.

Wilcox, D., Turbulence Modeling for CFD, Second Edition, DCW Industries, 1998.

Yakhot, V., Orszag, S. A., "Journal of Scientific Computing", vol. 1, no. 3, 1986.

Yakhot, V., Thangam, S., Gatski, T. B., Orszag, S. A., Speziale, C. G., "Physics of  
Fluids A".

Yoon, B. K., Chung, M. K., "Computation of Compression Ramp Flow with a Cross-  
Diffusion Modified  $k$ - $\varepsilon$  Model", AIAA Journal, vol. 33, no. 8, pp.1518-1521, 1996.